The Pennsylvania State University
The Graduate School

FRACTAL MODELING OF LIGHTNING DISCHARGES

A Thesis in
Electrical Engineering
by
Jérémy A. Riousset

Submitted in Partial Fulfillment
of the Requirements
for the Degree of

Master of Science

August 2006

The thesis of Jérémy A. Riousset was reviewed and approved* by the following:

Victor P. Pasko
Associate Professor of Electrical Engineering
Thesis Advisor

Douglas H. Werner
Professor of Electrical Engineering

Kenneth W. Jenkins
Professor of Electrical Engineering
Department Head

*Signatures are on file in the Graduate School.

Abstract

The direct comparison of lightning mapping observations by the New Mexico Tech Lightning Mapping Array (LMA) with realistic models of thundercloud electrical structure and lightning discharges represents a useful tool for studies of electrification mechanisms in thunderstorms, initiation and propagation mechanisms of different types of lightning discharges as well as for understanding of electrical and energetic effects of tropospheric thunderstorms on the upper regions of the Earth's atmosphere. For this purpose, the development of efficient numerical lightning models is essential. In this thesis, we provide an up-to-date review of the electrical structure of thunderclouds and of the mechanisms of lightning propagation. We also introduce a new three-dimensional probabilistic model describing development of bi-directional structure of positive and negative lightning leaders closely resembling processes observed by LMA in association with intracloud discharges. The model represents a synthesis of the original dielectric breakdown model based on fractal approach proposed by *Niemeyer et al.* [1984] and the equipotential lightning channel hypothesis advanced by *Kasemir* [1960], and places special emphasis on obtaining self-consistent solutions preserving complete charge neutrality of the discharge trees at any stage of the simulation. Special attention is paid to performing a thorough validation of the model. Simple case studies are used to evaluate the accuracy of the derivation of the electric field, potential, charge density and charge transfer in the model. The model results are compared to a representative intracloud discharge measured by LMA in a New Mexico thunderstorm on July 31, 1999. These comparisons indicate that the model is capable of realistically reproducing principal features of the observed event including the initial vertical extension of the discharge between the main negative and upper positive charge regions of the thundercloud, followed by horizontal progression of negative and positive leaders in the upper positive and main negative charge regions, respectively. For the particular model case presented in this thesis, the total charge transfer, the vertical dipole moment and the average linear charge density associated with the development of bi-directional structure of lightning leader channels are estimated to be 37.5 C, 122 C·km, and 0.5 mC/m, respectively, in good agreement with related data reported in the referred literature. The model results also demonstrate that the bulk charge carried by the integral action of the positive and negative leaders leads to a significant (up to 80%) reduction of the electric field values inside the thundercloud, significantly below the lightning initiation threshold.

Table of Contents

List of Figures

List of Tables

List of Symbols

δx, δy, δz	Discretization steps in x-, y- and z-directions (m)
ε_0	Permittivity of free space (ε_0=8.85 $\times$ 10^{-12}) (F/m)
η	Probability sensitivity (dimensionless)
ϕ	Total electric potential ($\phi = \phi_{amb} + \phi_{cha}$, see below) (V)
ϕ_0	Total electric potential of the channel(V)
ϕ_{amb}	Ambient electric potential due to cloud charges (V)
ϕ_{cha}	Electric potential due to polarization charges on the channel (V)
ϕ_{gnd}	Total electric potential of the ground boundary (V)
ρ_{amb}	Thundercloud charge density (C/m^3)
ρ^i_{amb}	Ground image of the thundercloud charge density (C/m^3)
ρ_{cha}	Polarization charge density in the channel (C/m^3)
ρ^i_{cha}	Ground image of the polarization charge density in the channel (C/m^3)
ρ^l_{cha}	Average linear charge density of the discharge tree (C/m)
d_{LP}, d_N, d_P	Depths of the lower positive, central negative and upper positive charge layers (m)
$\vec{E}$	Total electric field ($\vec{E} = \vec{E}_{amb} + \vec{E}_{cha}$, see below) (V/m)

$\vec{E}_{amb}$	Ambient electric field due to cloud charges (V/m)
$\vec{E}_{cha}$	Electric field due to polarization charges on the channel (V/m)
E_{init}	Electric field threshold for discharge initiation (V/m)
E_{cr}^{+}	Electric field threshold for propagation of positive streamers (V/m)
E_{cr}^{-}	Electric field threshold for propagation of negative streamers (V/m)
E_k	Electric field conventional breakdown threshold (V/m)
E_{th}^{+}	Electric field threshold for propagation of positive leaders (V/m)
E_{th}^{-}	Electric field threshold for propagation of negative leaders (V/m)
l	Length of a link (m)
L	Total length of the discharge (m)
N	Neutral density (m^{-3})
N_0	Neutral density at sea level (m^{-3})
$\vec{p}$	Electric dipole moment of the discharge (C·m)
p_i	Probability of propagation for a candidate link i ($p_i \in [0, 1]$)
Q_{cha}^{+}	Net charge carried by the positive leaders (i.e., charge transfer) (C)
Q_{LP}, Q_N, Q_P	Net charges in the lower positive, central negative and upper positive charge layers (C)
R_{LP}, R_N, R_P	Radii of the lower positive, central negative and upper positive charge layers (m)

Acknowledgments

First and foremost, I must express my deepest gratitude to my advisor Dr. Victor P. Pasko, who introduced me to the lightning research area. Without his constant support, guidance and confidence during the last two years, the research presented in this paper would not have been possible. I would also like to thank Dr. Douglas H. Werner for his feedback as a member of my thesis committee. I am equally indebted to Drs. Paul R. Krehbiel, William Rison, Ronald J. Thomas and William P. Winn for insightful directions and their tremendous help as co-authors or reviewers of my first paper, which is a preponderant part of this work. I am also indebted to the CEDAR community for the many helpful discussions and lectures during the 2005 and 2006 Summer Workshops.

I wish I could name all my friends in Europe, Asia or in the United States to express my thanks to them, but I am afraid this would make this thesis much longer. I hope they know that I forget none of them and that I could never possibly repay them the way they deserve it for their constant support and friendship in times of happiness as well as in moments of discouragements.

Finally, I would like to thank my family (in Europe and Canada) with a special thought for my parents Michèle and Christian and my sister and brother, Pauline and Nicolas, for the endless encouragements and support that they have given to me throughout my life.

Jérémy Riousset,
University Park, PA
July 9, 2006

This research was supported by the National Science Foundation under grant ATM-0134838 to the Pennsylvania State University.

Dedication

to my loving mother and father,

Michèle *and* Christian Riousset

pour leur affection et leur soutien indéfectible.

Chapter 1

Introduction

1.1 Brief History of Lightning Modeling

The first scientific study of lightning should be granted to Benjamin Franklin during the second half of the eighteen century [*Uman*, 2001, p. 3]. His various experiments established the electrical nature of the thundercloud and of the lightning discharge [*Franklin*, 1751; *Krider*, 2006]. However, major breakthroughs in the study of discharge propagation were long to come and made possible by the invention of the streak camera by Boys in 1926. In particular, the leader process as an initiation and propagation mechanism of cloud-to-ground lightning was determined photographically during the 1930's by Schonland, Malan and co-workers in South Africa (as summarized by *Uman* [1984, p. 5; 2001, pp. 7, 83]).

This basic mechanism is now known to be also valid for intracloud discharges [*Ogawa and Brook*, 1964; *Proctor*, 1981, 1983; *Uman*, 1984, p. 10; *Liu and Krehbiel*, 1985; *Shao and Krehbiel*, 1996; *Rakov and Uman*, 2003, p. 322]. However, understanding of the internal physics of the leader process is still far from complete [e.g., *Bazelyan and Raizer*, 2000, pp. 84–85; *Gallimberti et al.*, 2002; *Pasko*, 2006, and references therein] (for details on the leader process, see Chapter 2 of this thesis).

Interest in studies of lightning discharges has been renewed by the potential hazards induced by lightning strokes on aircraft, spacecraft, and installations using solid-state electronics. First models of the lightning discharge directed towards a theoretical description of the interaction between the lightning and the surrounding thunderstorm electric field had been developed in the 1950's [e.g., *Kasemir*, 1960, and references therein]. The complexity of the phenomenon and the lack of a complete theory on lightning propagation led some authors to consider only the bulk effects of the lightning discharges in the development of cloud electrification models [e.g., *Ziegler and MacGorman*, 1994; *Krehbiel et al.*, 2004]. The model presented in this thesis belongs to a category of lightning simulations which put emphasis on the channel itself.

Among the earliest models of this kind is *Kasemir*'s [1960]. *Kasemir* [1960] modeled the lightning channel as an equipotential, overall neutral, prolonged spheroid placed in the thundercloud electric field. The spheroid is vertical and lies on the main axis of the system, which is assumed to possess a rotational symmetry. The induced linear charge density on the channel is derived based on the surrounding ambient potential of the thundercloud.

Mazur and Ruhnke [1998] revisited *Kasemir*'s [1960] model with the same assumptions of overall neutrality and equipotentiality in order to investigate the relationships among cloud charges, potentials and electric fields, and the induced charges, currents, and electric field changes associated with the lightning channel. The linear charge density in the channel was no longer derived analytically but numerically. This work utilized a tripolar-like charge model to study the development of cloud-to-ground and intracloud discharges, but the system remained axisymmetric and did not allow for branching or horizontal development. Unlike *Kasemir*'s [1960] model, in which the estimation of the potential was done for a channel of fixed length, *Mazur and Ruhnke* [1998] introduced a dynamical variation of the channel length to simulate the discharge progression.

Recently, *Behnke et al.* [2005] applied the principles of *Mazur and Ruhnke*'s [1998] model to investigate the evolution of initial leader velocities during intracloud lightning. Instead of these authors' model of a thundercloud, they used a more realistic model derived from lightning mapping and electric field sounding observations of actual storms. Like *Mazur and Ruhnke* [1998], *Behnke et al.* [2005] ensured the overall neutrality of the channel by adequately shifting the electric potential of the channel.

Helsdon et al. [1992] used *Kasemir*'s [1960] equipotential, spheroid, overall neutral representation of the lightning in their Storm Electrification Model. The problem was solved in a two-dimensional (2-D) Cartesian domain, with no hypothesis concerning the symmetry of the channel. To overcome the difficulty of deriving a linear charge density in 2-D, *Helsdon et al.* [1992] derived an analytical expression for the linear charge density carried by a channel of the designated spheroid geometry. In this model, the lightning propagates with no branching along the field lines defined by the ambient field configuration regardless of the electric field due to the lightning channel itself. *Helsdon et al.* [2002] extended the previous model to a 3-D geometry. The channel is again neutral and equipotential and propagates bidirectionally between the grid points of the three-dimensional Cartesian space, with essentially the same limitations as in the 1992 model. Other models based on the same concepts have been developed but are not described here for the sake of brevity. A review of those can be found in [*Poeppel*, 2005, pp. 1–5].

A significant limitation of the aforementioned models is related to the deterministic character of the lightning propagation. Indeed, none of these models is able to reproduce the observed morphology of highly distorted and branched path of the lightning in a realistic way. This issue cannot be resolved at present using a micro-physical approach to the lightning propagation because of insufficient knowledge of the related processes and also due to the lack of computational power.

In his pioneer work on the mathematics of fractals and their applications, Benoit Mandelbrot suggested the use of random fractals model as a tool to model complex physical phenomena [*Mandelbrot*, 1983, pp. 201–204]. In this book, he underlined the impossibility to use complicated deterministic algorithms to solve many physical problems and emphasized that *"[such an approach] would be not only tedious, but doomed to failure. [...]"* and logically concluded that *"The goal of achieving a full description is hopeless and should not even be entertained"*. This led him to develop an alternative solution using a probabilistic approach and the concept of fractal geometry. This inspiring idea was extended to many problems in various branches of physics among which fractures in brittle and quasi-brittle materials [e.g., *Cherepanov et al.*, 1995; *Borodich*, 1997], and dielectric breakdown patterns [e.g., *Niemeyer et al.*, 1984]. Applied to gas discharges, the idea of these models is to simulate the macroscopic behavior of the discharge by using a probabilistic approach to reproduce the fractal geometry of the discharge channels rather than by resolving internal physics of the channel. Hence, shortly after the introduction of fractal mathematics, *Niemeyer et al.* [1984] proposed a Dielectric Breakdown

Model capable of reproducing the basic features of Lichtenberg's figures produced by a leader surface discharge in compressed SF_6 gas. This model by *Niemeyer et al.* [1984] has been further discussed, refined and improved in [*Satpathy*, 1986; *Niemeyer et al.*, 1986; *Niemeyer and Wiesmann*, 1987; *Niemeyer et al.*, 1989; *Femia et al.*, 1993]. More recently, *Petrov and Petrova* [1993] used *Niemeyer et al.*'s [1984] Dielectric Breakdown Model to introduce stochasticity in the modeling of the lightning. Fractal models of gas discharges have also been successfully applied to reproduce other atmospheric electrical phenomena such as sprites [e.g., *Pasko et al.*, 2000, 2001] and blue jets [*Pasko and George*, 2002].

Petrov and Petrova's [1993] model used a dipole representation of a thundercloud in a 2-D Cartesian space. The links between grid points resembling lightning channels were initiated from a central circular region in the simulation domain where the potential was kept constant. The model used unusually high electric field values for the discharge initiation threshold and employed a variable voltage drop along the channel to simulate its resistivity. *Petrov et al.* [2003] further extended this model to a 3-D Cartesian geometry to predict the probability of lightning strikes to practical structures. Similarly to their previous model, the potential of a point of a new link at the moment of its connection with the discharge remained unchanged for the remainder of the simulation. No assumptions concerning the channel neutrality were employed and no charge densities were derived. *Mansell et al.* [2002] also extended *Niemeyer et al.*'s [1984] model to a 3-D Cartesian geometry. In addition, they added bidirectional propagation of the model lightning trees, and integrated it in a numerical thunderstorm model. As in *Petrov and Petrova* [1993], the channel is resistive but with a fixed voltage drop between adjacent channel grid points. Like *Kasemir* [1960], *Mansell et al.* [2002] assumed the overall neutrality of the channel, which was ensured by favoring the development of a part of the bidirectional tree having a charge deficit. In particular, if the overall net charge carried by the discharge trees after an iteration was positive (respectively negative), the threshold field needed for advancement of branches of negative (respectively positive) polarity was lowered to enhance their development until neutrality was achieved [*Mansell et al.*, 2002].

The aforementioned channel-based simulations of lightning only model the leader part of the discharge. Nonetheless, it is well known that a streamer zone, not described in the previous models, develops at the leader tip and plays an important role in leader advancement (see Section 2.2 in this thesis for details). Because of its high conductivity, the leader is analogous to an equipotential metallic wire which gets polarized when placed in the thundercloud ambient electric field. The resulting accumulation of charge at the tip of the leader enhances the surrounding electric field above the threshold required for initiation of streamers. Consequently streamers continuously develop in the region surrounding the tip with a generation frequency on the order of 10^9 s^{-1} [*Bazelyan and Raizer*, 2000, p. 71]. The charge density associated with streamers leads to a self-consistent reduction of the electric field in the leader streamer zone to values comparable to the streamer initiation threshold [*Bazelyan and Raizer*, 2000, pp. 56–71]. In addition, currents of all streamers starting from a leader tip are summed up, heating the region ahead of the tip and therefore increasing its conductivity permitting further propagation of the leader channel [*Bazelyan and Raizer*, 2000, pp. 53-64 and p. 255; *Rakov and Uman*, 2003, pp. 136 and 226]. The exclusion of the direct modeling of the streamer zone in existing models is justified by the lack of knowledge of the detailed physics of this region as well as by the computational expenses involved in a thorough description of it.

Kupershtokh et al. [2001] proposed to introduce the streamer zone in probabilistic lightning models using a cellular automata approach. *Kupershtokh et al.*'s [2001] model does not deal with the underlying microphysics of the process. Thus, from this point of view it remains close to *Niemeyer et al.*'s [1984] original model. The previous models consider only two states for any grid point in the simulation domain–a conducting state, if the point is crossed by the leader, and a dielectric state otherwise. The use of a cellular automata approach described in [*Kupershtokh et al.*, 2001] allows the introduction of a third, streamer state, reproducing the streamer zone. Moreover, *Kupershtokh et al.* [2001] introduced time in their model to overcome the absence of an actual time-scale in the *Niemeyer et al.*'s [1984]-based models. The model developed in [*Kupershtokh et al.*, 2001] has not yet been applied to the modeling of leader development in realistic thundercloud configurations.

Agoris et al. [2004] also introduced leader–streamer zone effects but still based their model on the classical *Niemeyer et al.*'s [1984] dielectric breakdown model.

In addition, they used a time-scale for propagation of streamer and leader bounds. The formation time of each streamer segment likely to propagate the discharge is derived using the assumption of a Weibull probability distribution function and compared to the time step of the current iteration (defined as the average of the times of formation of all candidate streamer bounds). Hence at each step, if the time of formation of a candidate streamer link is smaller than the time step of the current iteration, the link is added to the existing tree. Unlike the leader streamer corona mechanism described above, the formation of leader channels is considered to be done at constant velocity compared to streamer propagation (and therefore with a constant time step). Its driving mechanisms are the same as in *Femia et al.* [1993], except that candidate leader bounds are now defined between the leader channels and points occupied by a streamer link. This model is run in a 2-D Cartesian simulation domain and no charge considerations are accounted for at any stage of the development of either streamer or leader channels. This model has been applied to the study of Franklin rod height impact on the striking distance and produced results in good agreement with experiments.

In *Kupershtokh et al.*'s [2001] model as well as in any models based on approaches proposed by *Niemeyer et al.* [1984], the channel propagates through grid points of a discretized 2-D or 3-D domain. Therefore, the channel propagation often takes unrealistically sharp angles. This issue has been addressed by *Helsdon and Poeppel* [2005]. These authors proposed to avoid grid dependency in a 3-D geometry by deriving the direction of the lightning propagation based on the location of random free electrons near the leader tip, and no longer in terms of the probability introduced by *Niemeyer et al.* [1984]. Stochasticity is introduced by the location of the free electrons, which is derived using a Monte Carlo technique. The channel is assumed to be equipotential and the linear charge density is derived using the theory for unbranched conductors [e.g., *Mazur and Ruhnke*, 1998]. *Helsdon and Poeppel* [2005] were able to identify numerical parameters responsible for the global behavior of the channel (e.g., branching, arresting of propagation, etc.). The model produced positive leaders developing in the negative charge regions, and negative leaders propagating in the positive charge center, consistent with expectations.

1.2 Problem Formulation

In the process of reviewing fractal models of gas discharges in the available literature, we noticed that ever since the fractal models have been introduced by *Niemeyer et al.* [1984] to reproduce the behavior of breakdown channels, it has been extensively used in atmospheric research (for example, to model lightning flash [e.g., *Mansell et al.*, 2002; *Petrov et al.*, 2003] or gap breakdown in dielectrics [e.g., *Niemeyer and Wiesmann*, 1987; *Niemeyer et al.*, 1989; *Petrov and Petrova*, 1992]). We also noted that most of the model validations have been done by phenomenological comparison of numerical results with real pictures [e.g., *Mansell et al.*, 2002], or by developing experiments easily comparable to simulation results [e.g., *Femia et al.*, 1993].

Surprisingly, we could not find any work on quantitative estimations of the errors involved in fractal models. In particular, fractal models employ a discretization of space, and some algorithms to derive parameters such as:

- the potential in the discharge channels
- the net charge carried by the discharge trees
- the linear charge density in the leader branches
- the volumetric charge density in the simulation domain

Little has been done to check the implications of the approximations introduced by the use of those procedures on the accuracy of the results produced by the simulations. Therefore, there is a definite lack of validation studies related to fractal models that should be addressed before conclusions can be drawn about the applicability of fractal modeling to simulation of gas discharges. One of the central goals of this thesis is to perform such validation studies.

One of the motivations for the development of the fractal model presented in this work, is the idea to unify *Kasemir*'s [1960] hypotheses with fractal modeling in a self-consistent scheme. Among the fractal models mentioned in the previous section, either no hypothesis of neutrality have been used [*Niemeyer et al.*, 1984; *Niemeyer and Wiesmann*, 1987; *Niemeyer et al.*, 1989; *Femia et al.*, 1993; *Petrov and Petrova*, 1993; *Pasko et al.*, 2000, 2001; *Pasko and George*, 2002; *Popov*, 2002;

Petrov et al., 2003; *Agoris et al.*, 2004] or mathematical artifacts were used to decrease the net charge in the channel and to move the system closer to the charge neutral state [e.g., *Mansell et al.*, 2002]. In particular, none of these models modified the potential of a link once it has been connected to the discharge tree. The idea of ensuring overall neutrality of the discharge by shifting the channel potential to adequate values has been first suggested by *Kasemir* [1960] and applied to a simplistic 1-D model of the discharge in [*Mazur and Ruhnke*, 1998; *Behnke et al.*, 2005]. In this work we propose to apply *Kasemir*'s [1960] hypothesis to three-dimensional fractal modeling.

Thus, the purpose of this thesis is to develop a 3-D fractal model of lightning derived from *Niemeyer et al.*'s [1984] Dielectric Breakdown Model. The model uses *Kasemir*'s [1960] equipotential hypotheses to describe the channel properties. Special emphasis is placed on obtaining self-consistent solutions preserving complete charge neutrality of discharge trees at any stage of the simulation. Efforts are also put in a thorough validation of the model by comparisons with experimental results and alternative models. This model is eventually applied to investigate the reduction of the thunderstorm electric field by an intracloud discharge.

1.3 Organization of the Thesis

Chapter 1 has begun our discussion with a review of the relevant literature on the modeling of lightning discharges. We have focused our review on existing fractal models and their alternatives. Chapter 2 is dedicated to the underlying mechanisms governing the occurrence and propagation of the lightning phenomenon. In particular, it focuses on presenting a review of the electrical structure of thunderclouds and of the physics of the lightning channel. The discussion of the physics of the lightning propagation is helpful for understanding the numerical model presented in Chapter 3. Chapter 4 provides a discussion about the applicability of the model to lightning discharge simulations as well as evaluation of the accuracy of the produced results. The model is applied to the simulation of intracloud discharges in Chapter 5, in which additional model validation is also provided by comparison with real lightning discharges. Chapter 6 provides conclusions and suggests future research relevant to the present study. Two appendices (A and B) are included to provide further details about the model charge and potential sources and some limitations of the method of moments.

1.4 Scientific Contributions

This thesis makes several contributions to the fields of atmospheric electricity and gas discharge modeling, which can be summarized as follows:

1. Two different kinds of channel-based lightning models are united; on one hand, one-dimensional model using potential shift to ensure discharge neutrality, on the other hand, three-dimensional fractal models capable of reproducing the chaotic aspect of the lightning path.

2. The validity of the derivation of the electric potential using a successive over-relaxation (SOR) algorithm for any fractal model of gas discharge, including models of upper atmospheric discharges such as sprites and blue jets [*Pasko et al.*, 2000, 2001; *Pasko and George* , 2002] is demonstrated.

3. The applicability of the proposed model to lightning studies is demonstrated by direct comparisons of the model results to a representative intracloud discharge measured by the New Mexico Tech Lightning Mapping Array (LMA).

4. A possible mechanism based on polarization charges induced on the discharge trees leading to the fractional reduction of the electric field experimentally observed after intracloud lightning discharges is identified.

Most of the results presented in this thesis have been submitted for publication on June 6, 2006 in a form of full-length paper in the Journal of Geophysical Research–Atmospheres [*Riousset et al.*, 2006a] and presented at CEDAR 2006 workshop [*Riousset et al.*, 2006b].

Chapter 2

Thunderclouds and Lightning

2.1 Electrical Structure of Thunderclouds

Unfortunately it is very difficult to obtain global data on the electrical field in thunderstorms. Usual measurement techniques are limited to measurement around the probe. For example, a rocket sounding can provide information on the local electric and magnetic fields around the rocket tip within a 0–12 km altitude range [*Winn et al.*, 1974], but cannot provide data about the electric field or charge density in the overall volume of the thundercloud. Neither can a balloon sounding which provides information on the local electric field and charge density in its surroundings [*Marshall et al.*, 1995, and references therein]. Moreover, data are measured at different altitudes and different moments of time, depending on the ascending rate. The major differences between those two techniques lay in the duration of the measurements and the rate of displacement of the probe when it measures the storm. Balloon soundings can be combined to radar data to obtain the radar reflectivity in vertical cross sections in the vicinity of the balloon [*Shepherd et al.*, 1996]. Slow antennas measure field changes, allowing detection of flashes but are unable to distinguish intracloud (IC) and positive cloud-to-ground (+CG) discharges [*Marshall et al.*, 1996]. The New Mexico Tech Lightning Mapping Array (LMA) provides location of sources of impulsive VHF radiation in the 60–66 MHz band by measuring the arrival times of the radiation at up to ten receiving stations [*Rison et al.*, 1999; *Coleman et al.*, 2003]. The LMA data can be used to track the path of a single lightning event (see Figure 2.1).

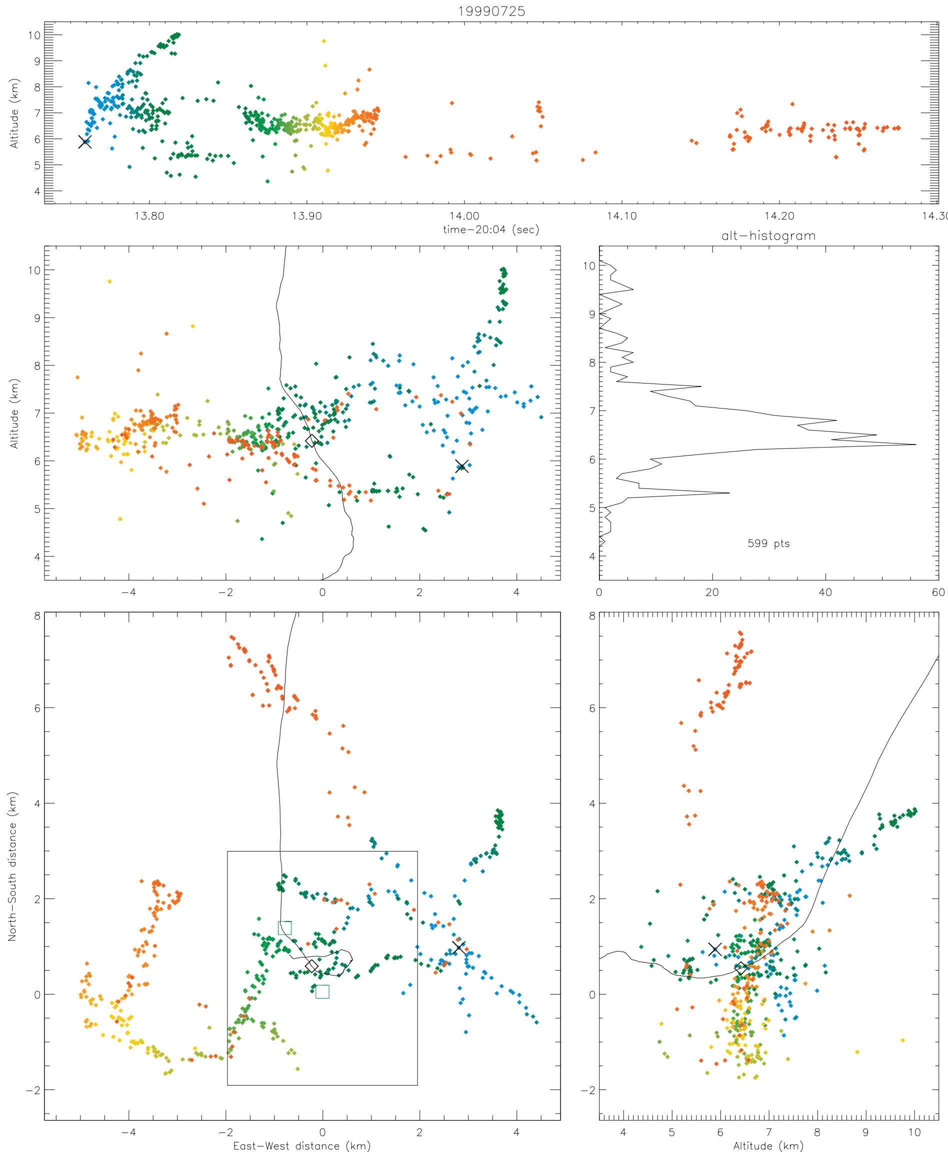

Figure 2.1. Example of LMA data from [*Coleman et al.*, 2003, Figure 1]. This intracloud (IC) flash occurred at 2004:13 UT on 25 July 1999. Locations of VHF radiation sources detected by the LMA are color-coded by time and displayed in five different graphs (clockwise from top): altitude versus time, altitude histogram of the sources in 100-m bins, a projection of the sources onto the south-north vertical plane, a horizontal (plan) projection of the sources, and a projection of the sources onto the west-east vertical plane. The crosses denote the position of the first LMA source. The first source was at 5.8 km altitude and was the likely location of flash initiation. The path of an instrumented balloon is shown in the projections; the diamonds show the location of the balloon at the time of the flash. The two small squares in the middle of the horizontal projection indicate the locations of two of the 10 LMA stations in the middle of the array. The station to the southeast was located at Langmuir Laboratory and is the origin of the horizontal coordinates. Altitudes are relative to mean sea level (msl).

The knowledge of the charge structure of the thundercloud is fundamental in lightning studies. This knowledge would allow to derive electric field everywhere, especially at the location of initiation of the lighting channel. However, based on the LMA data, we can only infer this structure on a global scale. Knowing that a lightning flash preferentially propagates in a region of large charge density [e.g., *Williams et al.*, 1985; *Mansell et al.*, 2002], the superposition of sequences of lightning discharges obtained with the LMA allows to retrieve the location of the denser charge regions [*Coleman et al.*, 2003]. The values of charges in these inferred charge regions can be deduced from balloon soundings (Figure 2.2). Obviously, this method only gives a large-scale image of the cloud, and misses the smaller details. Nevertheless, it allows to get a good quantitative idea of the global "electrical shape" of the thundercloud. The initiation of the lightning probably occurs in regions of intense electric field. Such regions could be of relatively small dimension compared to the size of the charge layers and hence would not clearly appear on the lightning inferred cloud structure. That is one of the reasons why it is difficult to accurately determine the electric field threshold required for lightning initiation. The only available data are the local values of charge density and electric field provided by balloon soundings, which might not be at the exact location of the initiation at the time when the lightning flash starts. Numerous series of soundings have been done to investigate the electrical structure of the thunderclouds. Some of these investigations are mainly based on balloon soundings, other also involve rocket soundings [e.g., *Marshall et al.*, 1995], or radar data [e.g., *Shepherd et al.*, 1996; *Marshall et al.*, 2001].

From the measurements cited above, the authors deduced the charge structure of the thundercloud. A common description of the charge distribution in the thunderstorm is based on a tripole model of the thundercloud [e.g., *Williams*, 1989; *Rakov and Uman*, 2003, p. 69]. This model is often regarded as an adequate approximation of the charge structure involved in lightning discharges in the convective parts of normally electrified storms. It employs a three-layer charge structure above a perfectly electrically conducting (PEC) ground plane. A main negative charge (Q_N) is located at mid-levels in the storm, with comparable upper positive charge (Q_P) above the negative and a weaker lower positive charge (Q_{LP}) below the negative (see Figure 2.3). The model can also be extended to

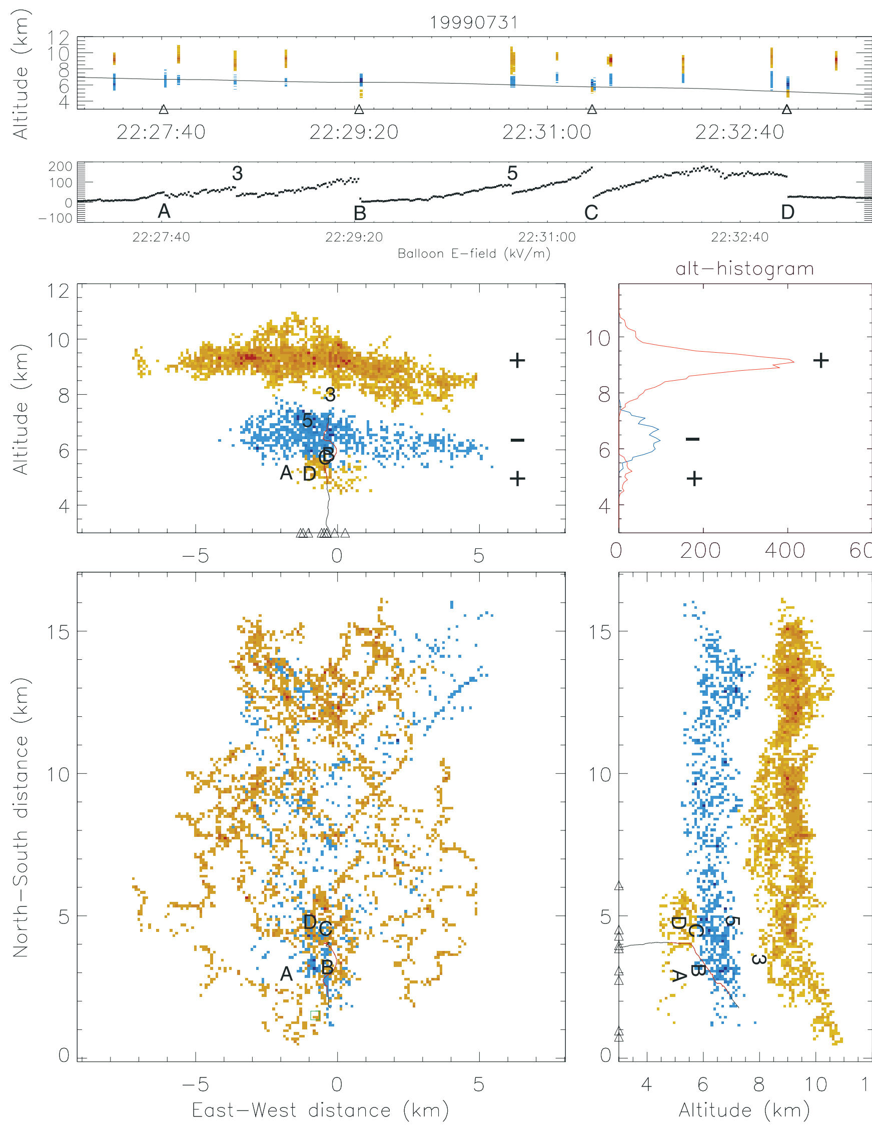

Figure 2.2. Example of cloud structure [*Marshall et al.*, 2005, Figure 1]. Lightning inferred storm charge structure for a 6 min time interval of LMA data collected during the descent of the sounding balloon. Yellow/red regions indicate positive charge; the blue region indicates negative charge. The letters show the initiation points of the cloud-to-ground (CG) and intracloud (IC) flashes that occurred in the part of the storm observed by the balloon. The occurrence times of the flashes are shown in the upper panels, and the red part of the balloon trajectory corresponds to the time interval of the lightning data.

Table 2.1. Charge heights and extents for the cylindrical disk model presented in Figure 5 of [*Behnke et al.*, 2005] and charge amounts required to initiate intracloud discharges.

Charge Layer	Altitude, km AGL[a]	Depth, km	Radius, km	Charge, C
Upper positive	7.0	2.0	2.5	31.5
Main negative	4.0	2.0	2.0	-45.0
Lower positive	1.5	2.0	2.0	4.5

[a] AGL, above ground level

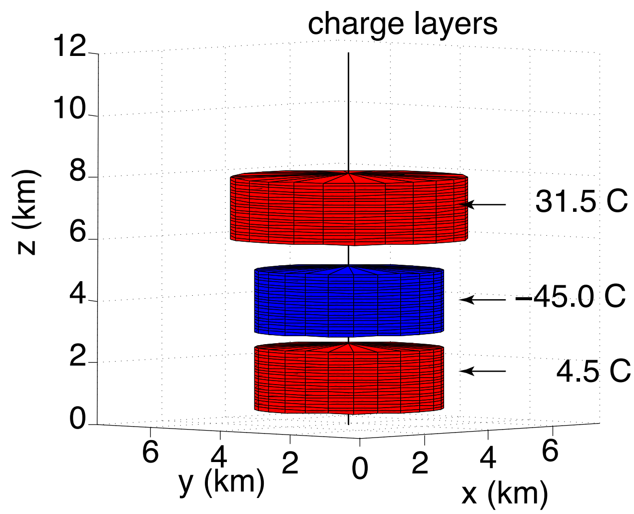

Figure 2.3. Representation of the tripole model based on data from [*Behnke et al.*, 2005] using parameters shown in Table 2.1. The main positive and lower positive layer are colored in red, while the main negative charge is colored in blue. The values on the plot give the total charge in the corresponding layer.

include a negative screening charge (Q_{screen}) at the top of the cloud, which is not considered in the simulation results presented in this thesis. An important aspect of storm charge structure, which is reflected by means of cylindrical disk models and is important in simulating the storm's lightning, is that the upper positive and main negative charge regions are distributed horizontally within the confines of the storm. We give an illustration of this model in Figure 2.3, which is based on the parameters suggested by *Behnke et al.* [2005] (Table 2.1).

An obvious advantage of this charge model is its simplicity. Moreover, it has been quite successfully applied to reproduce certain features of the thunderstorm such as the lightning leader initial velocity [*Behnke et al.*, 2005] or lighting path and branching [see Chapter 5 of this thesis]. *Mazur and Ruhnke* [1998] used a slightly modified tripole model to investigate the relationships among cloud charges, potentials and electric fields, and the induced charges, currents, and electric fields associated with the lightning channel. In this model, the lower positive charge is enclosed at the lower part of the main negative charge, which is split in two to better reproduce the updraft region. Recent studies of the cloud structure based on LMA data [e.g., *Marshall et al.*, 2005] have not confirmed that the lower positive charge is enclosed at the bottom of the main negative layer. However, this choice of modeling still remains fairly close to a tripole structure, which the authors argue to be especially suitable for modeling of isolated thunderstorms. Furthermore, the tripolar structure tends to be reproduced by recent numerical models of the global electrification of the thundercloud [e.g., *Barthe et al.*, 2005; *Altaratz et al.*, 2005].

Not all authors agree on the validity of the tripole model as an accurate description of the thundercloud electrical structure. In particular, *Marshall and Rust* [1993] suggested that large thundercloud complexes, so-called mesoscale convective systems (MCSs), were too complicated to be described by the simple tripole model (for further information about MCSs, see [e.g., *Stolzenburg et al.*, 1998a]). Investigations based on balloon soundings in the stratiform precipitation region of the MCSs (represented in the left part of Figure 2.4) led *Marshall and Rust* [1993] and *Shepherd et al.* [1996] to define alternative structures of so-called "Type A" and "Type B" to describe the charge configuration in this region. A type A structure is composed of four main regions of charge equally spaced with alternating polarities. The lowest charge region is negative, and a fifth screening region is added at the top. A type B structure seems to be associated with either bow-echo MCSs or with the presence of a well-defined trailing mesovortex at midlevels [*Marshall and Rust*, 1993]. The type B vertical structures consist of four main regions with alternating polarities, with the lowest region being negative. The main differences between the two electrical structures are the following: type B has fewer charge regions and a positive charge-density layer at 0°C, while type A is more complex and tends to have a negative charge-density layer at 0°C [*Marshall and Rust*, 1993; *Shepherd et al.*, 1996].

Stolzenburg et al.'s [1998a] picture of the MCS (Figure 2.4) supports the idea

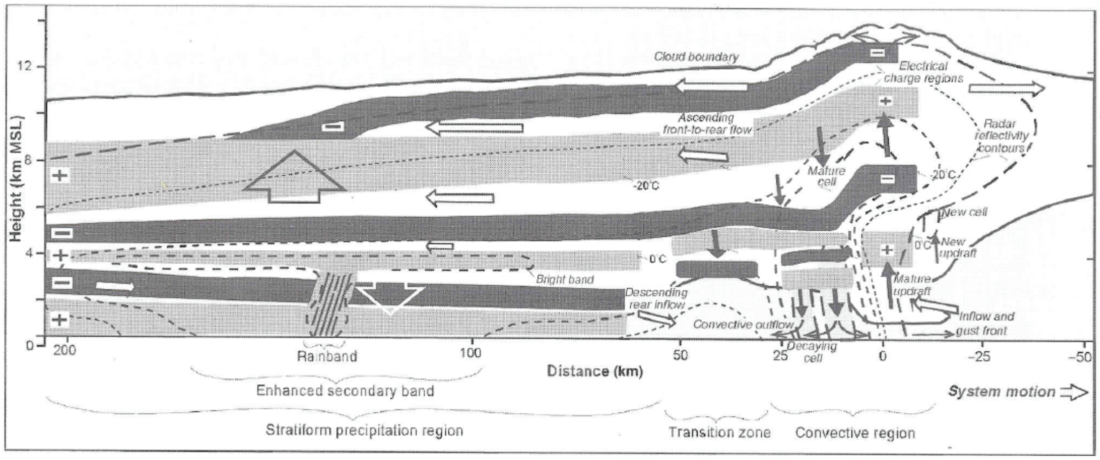

Figure 2.4. Conceptual model of the charge structure of an MCS [*Stolzenburg et al.*, 1998a; *Rakov and Uman*, 2003, p. 93]. Positive charge layers are indicated by the light grey shading and negative layers are indicated by the dark shading. The broken lines are radar reflectivity contours. In the convective region and the transition zone, the thick solid arrows depict convective updrafts and downdrafts, and the thin solid arrows show divergent outflows. The smaller open arrows represent system-relative flows, which are mainly horizontal. The mesoscale updraft and downdraft in the stratiform region are depicted by large open arrows (black and white outlines, respectively). There are four horizontally extensive cloud charge layers in the part of the stratiform precipitation region farthest behind the convective region, the fifth (lowermost) charge layer being seen in the stratiform region entirely below the cloud. An additional (negative) charge layer extends from the convective region through the nearest part of the stratiform region above all the other layers [*Stolzenburg et al.*, 1998a; *Rakov and Uman*, 2003, p. 93].

that the stratiform region of the MCS cannot be described based on the assumption of a tripole structure. However, how type A and type B structures fit in *Stolzenburg et al.*'s (1998a) picture of the thundercloud is unclear. In the same study, *Stolzenburg et al.* [1998a,b,c] also established that convective regions of MCSs, supercells and New Mexican thunderstorms, which are three types of thunderstorms, presented similar electric structures. They noticed that the convective updraft region of an MCS (shown in the right part of Figure 2.4), the updraft region of a supercell and the region near the center of a New Mexican storm (Figure 2.5) could be accurately described by a tripole structure with an additional negative screening layer at its top. Within the convective region of the thundercloud but outside of the updraft (to the left of the updraft diagram in Figure 2.5), the cloud electrical structure is similar to that described in stratiform region of MCSs (Figure 2.4)

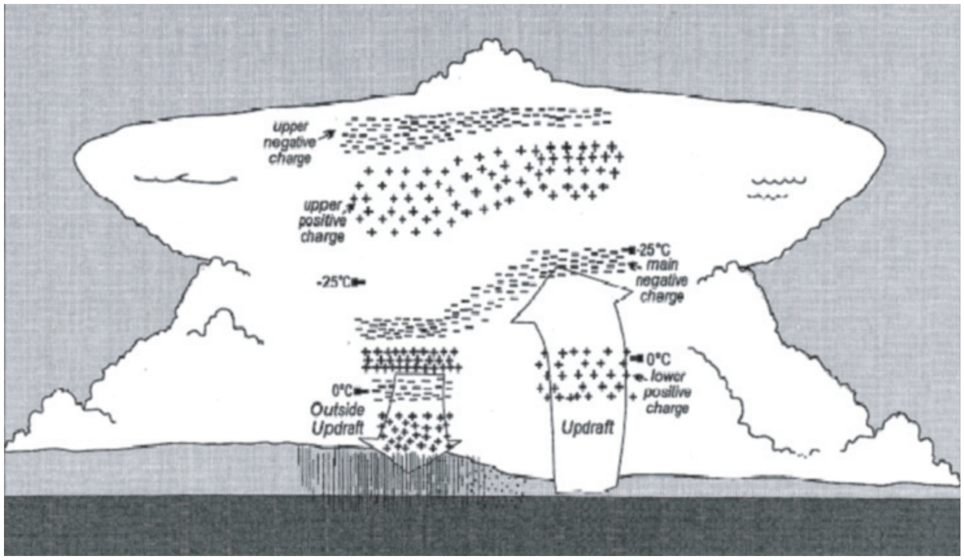

Figure 2.5. Schematic of the basic charge structure in the convective region of a thunderstorm [*Stolzenburg et al.*, 1998a; *Rakov and Uman*, 2003, p. 83]. Four charge layers are seen in the updraft region, and six charge layers are seen outside the updraft region (to the left of the updraft diagram). The charge structure shown in this figure is applicable to the convective elements of Mesoscale Convective Systems (MCS), isolated supercell storms, and New Mexican air-mass storms. Note that there is a variability about this basic structure, especially outside the updraft [*Stolzenburg et al.*, 1998a; *Rakov and Uman*, 2003, p. 83].

with possible variability between the three types of thunderstorms. Nevertheless it remains consistent with the idea that this region needs more than three charge layers to be properly described.

Finally, we conclude this section by noting that all interpretations of the measurements converge toward the idea of a stratified structure, but no consensus exists on the validity of the tripole model as an accurate description of the thundercloud. Yet, some authors still argue that a tripole charge model is not unreasonable for the mature stage of an isolated storm [e.g., *Mazur and Ruhnke*, 1998]. In addition, *Rakov and Uman* [2003, p. 81] question the distinction established by *Marshall and Rust* [1993] and justify the classical tripolar charge structure of the cloud interior by suggesting that those extra charge regions might be related to transitions between different stages of the thunderstorm evolution. Similarly, *Coleman et al.* [2003] suggest that the definition of type A and B structures may be due to a misqualification of charges deposited by previous discharges as charge centers and reaffirm in their study that the tripole structure is a good electrical equivalent of the thundercloud. From the above discussion, it appears that the tripole model (with additional screening layer) is at least accurate in the region where lightning discharges mainly occur. Therefore, we adopt the tripole structure for the simulation of lightning producing clouds in this thesis.

Although the exact physics of the formation of the charge layers is still not fully understood, it is known that each charge layer grows during the early stages of the thunderstorm and consequently enhances the local electric field. A discharge process is therefore required to prevent the electric field in the cloud from reaching unrealistic values. This is achieved through lightning discharges. The next section is therefore dedicated to a review of the mechanisms governing their development.

2.2 Physics of Lightning Leaders

The leader process is a well-documented means by which lightning develops in thunderstorms [*Uman*, 2001, p. 82]. The head of the highly ionized and conducting leader channel is normally preceded by a streamer zone looking as a diverging column of diffuse glow and filled with highly branched streamers [*Bazelyan and Raizer*, 1998, pp. 203, 253]. Figure 2.6 provides illustration of the leader-corona system. In this section we review essential physical processes involved in the for-

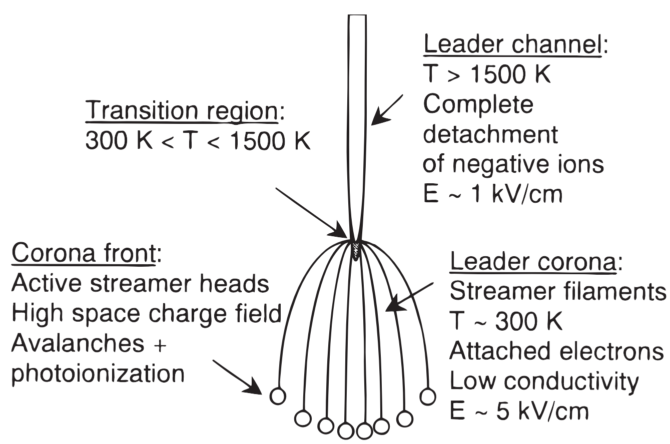

Figure 2.6. Sketch of the leader/leader-corona system, with the main characteristics of the different discharge regions [*Comtois et al.*, 2003].

mation and propagation of lightning leaders. This information provides important physical background for formulation of fractal lightning model presented in the next chapter.

2.2.1 Concept of a Streamer

Raizer [1991, p. 334] defines the streamer as *"a moderately, one can even say, weakly ionized thin channel formed from the primary avalanche in a sufficiently strong electric field"*. Some types of gas discharges are produced based on streamer phenomenon only, but streamers also serve as precursors to the more complicated leader phenomena, which will be discussed further in this chapter. A classic distinction is usually made between the streamer head (or active region), where the luminous emission and the ionization process occur, and the streamer tail (or passive region). The streamer head contains a net electrical charge which defines its polarity [*Gallimberti et al.*, 2002]. Due to its weak ionization, a streamer has low conductivity, with a voltage drop along its path often quoted as $\sim$5 kV/cm for positive streamers and ~ -10 kV/cm for negative streamers at ground pressure [*Bazelyan and Raizer*, 1998, pp. 156–158; 2000, p. 84; *Pasko and George*, 2002].

Gallimberti et al. [2002] summarized the streamer head and the streamer body characteristics. Those values are given at ground level and reproduced in Table 2.2.

Table 2.2. Streamer characteristics at ground level [*Gallimberti et al.*, 2002; *Pasko*, 2006].

Parameter	Value	Similarity relationship
	Streamer head	
Rotational temperature	330 K	constant
Vibrational temperature	$\geq$ 1000 K	constant
Electron energy	5–15 eV	constant
Electric field in front of the head	100–150 kV/cm	$\propto N/N_0$
Head radius	10–30 μm	$\propto N_0/N$
Electron density	10^{15} cm^{-3}	$\propto N^2/N_0^2$
	Streamer channel	
Channel radius	10–30 μm	$\propto N_0/N$
Electron density	$10^{13} - 10^{15}$ cm^{-3}	$\propto N^2/N_0^2$

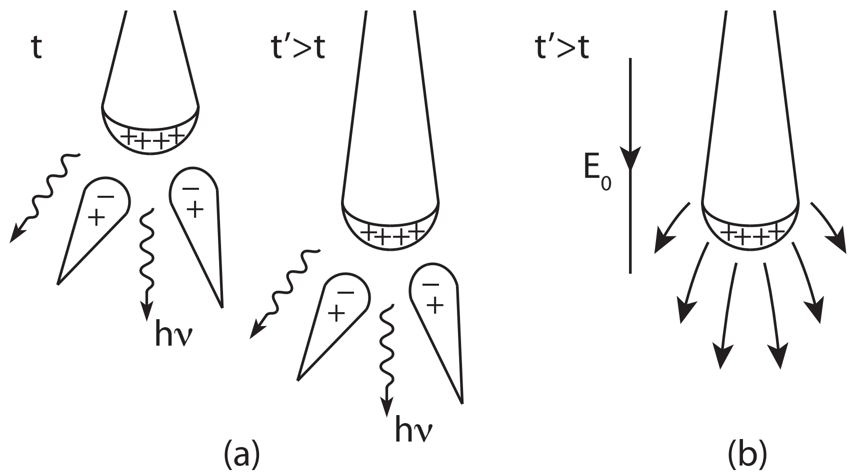

Figure 2.7. Positive (or cathode directed) streamer. (a) Streamer at two consecutive moments of time, with secondary avalanches moving towards the positive head of the streamer, and wavy arrows showing photons that generate seed (i.e., initial) electrons for avalanches. (b) Lines of force of the field near the streamer head. Adapted from [*Raizer*, 1991, p. 335; *Bazelyan and Raizer*, 2000, p. 33].

However, we note that these values must be scaled with altitude. *Pasko* [2006] reviews useful similarity relationships using the neutral density N (or equivalently the total pressure p assuming constant temperature of the neutral gas). The scaling factor is shown in the third column of Table 2.2, where N_0 denotes the neutral density at the sea level.

In both positive and negative streamer processes, the strong field near the tip is created mostly by the charge in the streamer head. In this region electrons are accelerated and get enough energy to ionize air molecules by electron impact. Streamer head also represents a source of UV photons which are able to ionize neutral gas ahead of the streamer head [e.g., *Liu and Pasko*, 2004, and references therein]. The radiation is mostly absorbed, but its intensity is high enough to provide an initial electron density of 10^5–10^6 cm^{-3} in a range of a couple of millimeters in front of the streamer tip. The electrons so-produced gain energy due to the strong local electric field (Figures 2.7b and 2.8b), generating the electron avalanches. Since the number of avalanches developing simultaneously is very large, they create in front of the plasma tip a new plasma region leading to spatial extension of the streamer [*Bazelyan and Raizer*, 2000, p. 33].

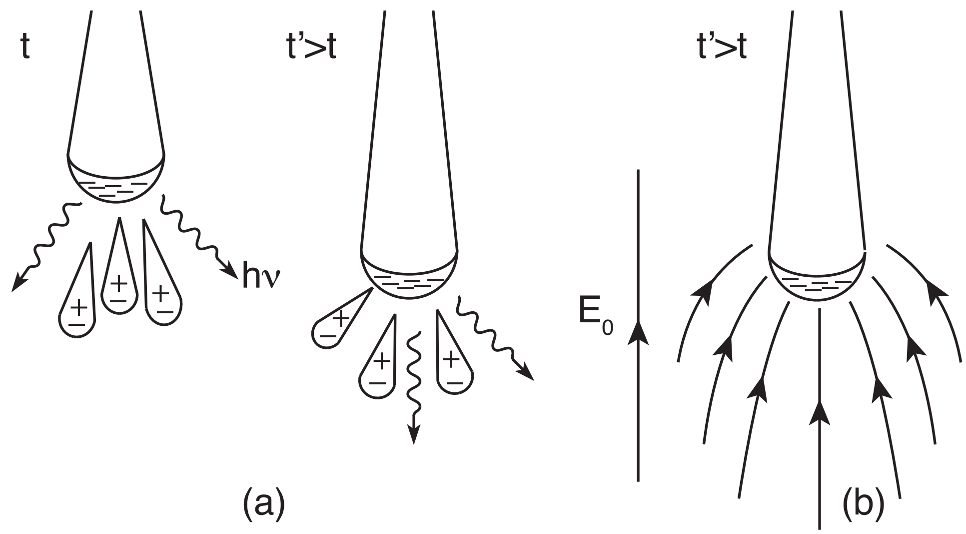

Figure 2.8. Negative (or anode directed) streamer. (a) Streamer at two consecutive moments of time, with secondary avalanches moving away from the negative head of the streamer (bubble shapes), and wavy arrows showing photons that generate seed (i.e., initial) electrons for avalanches. (b) Field in the vicinity of the head. Adapted from [*Raizer*, 1991, p. 338].

In a positive streamer (Figure 2.7a), electrons are avalanching towards the streamer head and neutralize positive charges in there to create a new section of the streamer body. Meanwhile a positive charge density appears at the other end of the avalanches. This becomes the new streamer head [*Bazelyan and Raizer*, 2000, p. 33].

Negative streamers propagate in a very similar way to positive ones. However, the different charge sign at the streamer tip introduces a few differences. Unlike in positive streamers, electrons drift away from the streamer tip. The negative charges in the streamer tip move rapidly in this strong field and join the positive charges of the avalanches ahead to form a plasma region. There, electrons at the front of the plasma region move away, repelled by the negative head, while electrons in the back (hence, in a weaker field) do not separate from ions and form with them a quasi-neutral plasma, which extends the streamer body (Figure 2.8a) [*Raizer*, 1991, p. 335].

Table 2.3. Electric field thresholds at ground pressure [*Pasko*, 2006, and references therein].

Threshold Name	Notation	Value
Thermal Runaway	E_c	∼260 kV/cm
Conventional Breakdown	E_k	∼32 kV/cm
Negative Streamer Propagation	E_{cr}^-	∼−12.5 kV/cm
Positive Streamer Propagation	E_{cr}^+	∼4.4 kV/cm
Relativistic Runaway	E_t	∼2 kV/cm
Leader Propagation	E_l or $E_{th}^{\pm}$	∼±1 kV/cm

2.2.2 Concept of a Leader

It is known that the electric field in a thunderstorm hardly exceeds 1.5 kV/cm [e.g., *Marshall et al.*, 1995]. This is insufficient for the propagation of positive or negative streamers (see Table 2.3). Thus the lightning breakdown must be of another nature. The lightning body extends as *"a thin, highly conductive, highly ionized channel [...] from the strong field region along the path prepared by the preceding streamers"*; this channel carries the potential along the path of the discharge much more efficiently than a streamer. This channel is known as a leader. This description, written by *Raizer* [1991, p. 364] for long gap discharges, equally applies for lightning discharges. The voltage drop in a leader is much less than that of a streamer; *Mansell et al.* [2002] quote the value of 0.5 kV/cm in their Stochastic Lightning Model, while *Pasko et al.* [2001] use an internal field in the streamer equal to the propagation threshold, i.e. ∼4.4 kV/cm for positive streamers and ∼−12.5 kV/cm for negative streamers.

The current understanding of the leader process is still far from complete [e.g., *Raizer*, 1991, p. 370; *Bazelyan and Raizer*, 2000, pp. 84-85; *Uman*, 2001, p. 79; *Rakov and Uman*, 2003, p. 136; *Pasko*, 2006]. In this section we provide the most accepted theory on leader propagation and emphasize differences between positive and negative leaders. Leaders of positive or negative polarities are thought to be able to propagate in ambient fields of the same order of magnitude [e.g., *Raizer*, 1991, p. 375; *Bazelyan and Raizer*, 1998, p. 253; *Rakov and Uman*, 2003, p. 322]. The related values are shown in Table 2.3.

A positive or negative streamer has been described as a plasma channel with internal electric field equal to $\sim$4.4 kV/cm or $\sim$$-$12.5 kV/cm, respectively. The neutral gas temperature in the streamer body is about 300 K. Under those conditions, low ionization occurs, and would actually be unable to sustain the channel propagation in long gap or lightning. The plasma produced at the tip of the streamer would decay and electrons would be lost due to recombination and attachment inherent to any electronegative gases (e.g., air). This would lead to a decrease of the conductivity of the channel and eventually to the suppression of its development, unless it enters a region of high electric field [*Bazelyan and Raizer*, 2000, p. 59].

In low electric field, the decay of the plasma can only be slowed down by an increase of the temperature of the neutral gas in the channel up to 5000–6000 K or more. At such temperature and relatively low electric field, the air ionization mechanism changes dramatically. Ionization of O_2 molecules is the main source of free electrons in streamers, but is negligible in low electric fields. Instead, at high neutral gas temperatures associative ionization reactions are now the primary source of electrons [*Bazelyan and Raizer*, 2000, p. 77]:

$$\mathrm{N} + \mathrm{O} + 2.8\,\mathrm{eV} \rightarrow \mathrm{NO}^{+} + \mathrm{e} \tag{2.1}$$

The lightning channel temperature has been measured to exceed 10,000 K, depending on the stage of development [*Rakov and Uman*, 2003, p. 7]. At such temperature, direct ionization of NO by electron impact may compete with associative ionization, all the more that gas heating decreases the gas density and therefore favors impact ionization process [*Bazelyan and Raizer*, 2000, pp. 59, 77]. Finally, the detachment reactions and decrease of the recombination rate in a hot plasma, compensate the loss of electrons by attachment process. Combined with associative ionization mechanisms, this allows the plasma channel to support itself in a relatively low field. This holds if we take for granted that gas heating does maintain plasma conductivity [*Bazelyan and Raizer*, 2000, pp. 59, 77].

The leader channel is not uniform. One can usually distinguish the main body, the transition region and the leader tip (see Figure 2.6). Most of the ionization occurs in the latter, where the gas is also gradually heated and the conductivity increased. The plasma in the rest of the channel is usually in a quasi-stationary

Table 2.4. Leader characteristics at ground level [*Helsdon et al.*, 1992; *Gallimberti et al.*, 2002; *Mansell et al.*, 2002; *Comtois et al.*, 2003; *Pasko*, 2006].

Parameter	Value
Leader head (Transition region)	
Temperature	330 K $<$ T $<$ 1500 K
Leader channel	
Temperature	$>$ 1500 K
Luminous diameter	0.5–4 mm
Thermal diameter	0.2–1 mm
Voltage drop	$\sim$0.5–1$\times 10^{-3}$ kV/cm
Linear charge density	$\sim$1 mC/m

state at high temperature of a few thousands of Kelvins [*Bazelyan and Raizer*, 2000, p. 75; *Gallimberti et al.*, 2002].

The main characteristics of a leader channel significantly depend on the experimental conditions. Therefore, values can vary whether measured for a short gap ($\sim$1.5 m) or a long gap ($>$10 m) or a lightning discharge. However, we tried to give an idea of the scale of those parameters based on the work of different authors [*Helsdon et al.*, 1992; *Gallimberti et al.*, 2002; *Mansell et al.*, 2002; *Comtois et al.*, 2003; *Pasko*, 2006]. Thus, values summarized in Table 2.4 must not be taken *per se*, but should rather be compared to values for streamer discharges reported in Table 2.2.

While the main difference between positive and negative streamers lies in the direction of the electron avalanches at the tip of the channel, the difference between leader of different polarities is far more complex. In particular, the propagation mechanisms and streamer zone structure of a negative leader are much more complicated than those of a positive leader and are still poorly understood [*Bazelyan and Raizer*, 2000, pp. 84–85; *Gallimberti et al.*, 2002]. Below we provide a summary of characteristics for positive and then for negative leaders.

The plasma in the leader body (or thermalized leader) is heated up to thousands of Kelvins, and consequently the conductivity of the channel is highly increased (to $\sim 10^4\ \Omega^{-1}\mathrm{m}^{-1}$ [*Rakov and Uman*, 2003, p. 227]). Therefore the leader head approximately carries the same potential as at the point where the discharge has been initiated. From this point of view, the leader can be considered roughly equipoten-

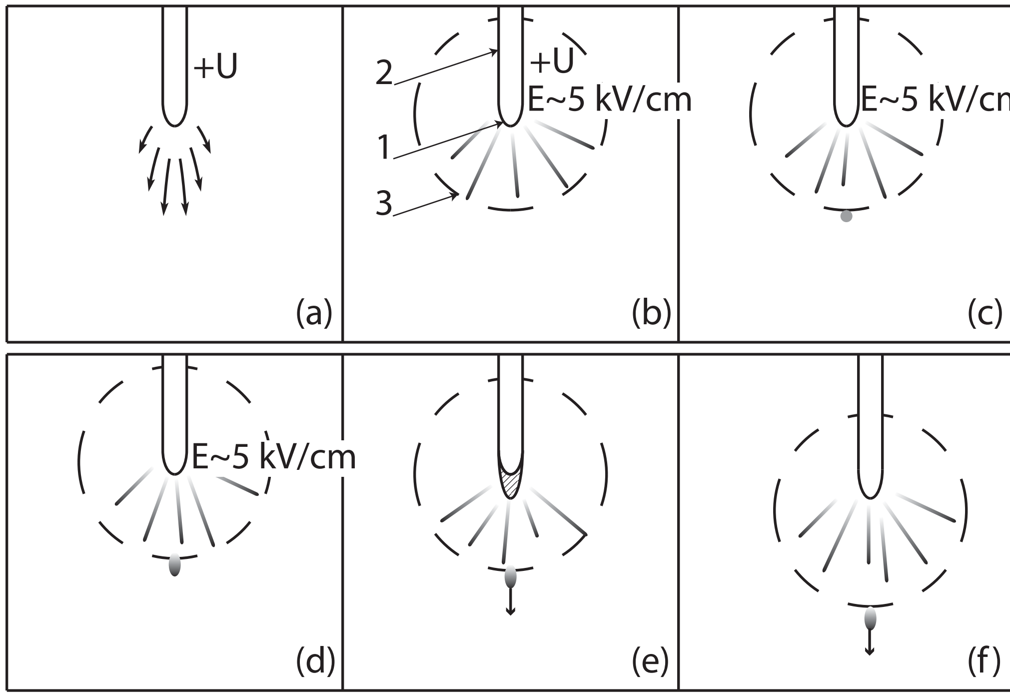

Figure 2.9. Development of a positive leader. Panels (a), (b), (c), (d), (e) and (f) represent different stages of the development; 1, leader tip; 2, leader channel; 3, streamer zone. See text for details.

tial or with a very low voltage drop (around 0.5 kV/cm, see [*Mansell et al.*, 2002] and Table 2.4). Hence the leader channel is analog to a metallic wire placed in a non-zero ambient field. It becomes polarized by the ambient field (i.e., the thundercloud electric field in the case of a lightning discharge). The resulting accumulation of charge at the tip of the leader enhances the surrounding electric field above the threshold required for initiation of streamers. The plot of the electric field lines around the tip of leader of positive polarity (Figure 2.9a) clearly illustrates this process. Their convergence towards the leader head indicates the increase of the E-field in this region. Consequently streamers continuously develop in the region surrounding the tip with a generation frequency on the order of 10^9 s^{-1} [*Bazelyan and Raizer*, 2000, p. 71] (Figure 2.9b). The charge density associated with streamers leads to self-consistent reduction of the electric field in the leader streamer zone to values comparable to the streamer propagation threshold. Besides, currents of all streamers starting from a leader tip are summed up (Figure 2.9d), leading to Joule

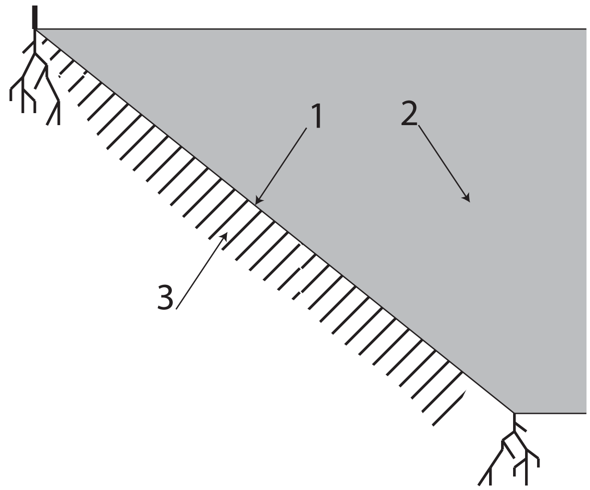

Figure 2.10. Schematic of a streak picture of a positive leader. 1, leader tip; 2, leader channel; 3, streamer zone [*Rakov and Uman*, 2003, p. 227].

heating of the region ahead of the tip (Figure 2.9e) and therefore to increase of its thermal energy. This energy input provokes a temperature increase of the gas molecules, a hydrodynamic expansion, a reduction of the gas density, and finally detachment of the negative ions due to both the increase of the gas temperature and low reduced electric field, defined as the ratio of electric field over the neutral density. These effects tremendously increase the conductivity at the leader head, permitting further propagation of the leader channel (Figure 2.9f). This mechanism, so-called current contraction in the front region of a leader channel is not quite clear, especially quantitatively. One may only assume the existence of ionization–thermal instability [*Bazelyan and Raizer*, 2000, pp. 53–64 and p. 255; *Gallimberti et al.*, 2002; *Rakov and Uman*, 2003, pp. 136 and 226].

A plasma spot formation is represented in Figure 2.9c. It is polarized in Figure 2.9d. The existence of this plasma spot has been shown for negative leader development (see further discussion in this section), but is still uncertain for positive leaders. However, even if present, the electric field in the streamer zone of positive leader ($\lesssim$5 kV/cm, see Table 2.3) is not strong enough to allow negative streamer development toward the leader head and consequently to modify the mechanism of development of the positive leader (recall that a field on the order of -12.5 kV/cm is needed for propagation of negative streamers, see Table 2.3). A streak picture of a positive leader discharge (sketched in Figure 2.10, see also [*Gallimberti et al.*, 2002]) shows that the leader tip and the leader streamer zone advance at roughly constant velocity ($\sim 2 \times 10^4$ m/s for a typical laboratory leader [e.g., *Lalande et al.*, 2002]).

The initial stages of the development of a negative leader are the same as those of a positive leader. The temperature of the leader body is increased to thousands of Kelvins, the electric field is increased around the leader tip (Figure 2.11a) up to values exceeding the propagation threshold of negative streamers (~ -12.5 kV/cm). Consequently, negative streamers develop to form the leader corona (Figure 2.11b). A plasma spot arises near the external boundary of the negative streamer zone (Figure 2.11c). The physical nature of the plasma spot is not understood at present. Under the effect of the ambient electric field, the plasma body becomes polarized (Figure 2.11d). The positive plasma dipole end, which is directed towards the main leader tip, serves as a starting point for positive streamers. We note that positive streamers require only 5 kV/cm fields for their propagation (Table 2.3) and can therefore easily propagate toward the negative leader head in streamer zone fields on the order of 12.5 kV/cm. The negative streamers can develop on the other end of the plasma body thanks to the field enhancement around it (Figure 2.11e). A current contraction process similar to that of positive leaders probably occurs at the tip of the plasma spot, allowing the development of a secondary leader, known as volume or space leader [*Bazelyan and Raizer*, 1998, pp. 254–255; 2000, pp. 85–88; *Rakov and Uman*, 2003, pp. 136–137]. The leader main channel slowly advances towards the volume leader. The positive end of the space leader develops towards the main leader and the negative end propagates in the opposite direction (Figures 2.11f and 2.11g). Normally, the positive streamer zone of the positive space leader almost immediately reaches the main negative leader. Therefore the junction between the main negative leader and the positive space leader is very quick, and develops in a way similar to the final stage of development of positive leader [*Bazelyan and Raizer*, 1998, p. 212]. When the space leader comes into contact with the main channel, they form a common conducting channel. A process of partial charge neutralization and redistribution occurs and results in the modification of the potential of the former space leader.

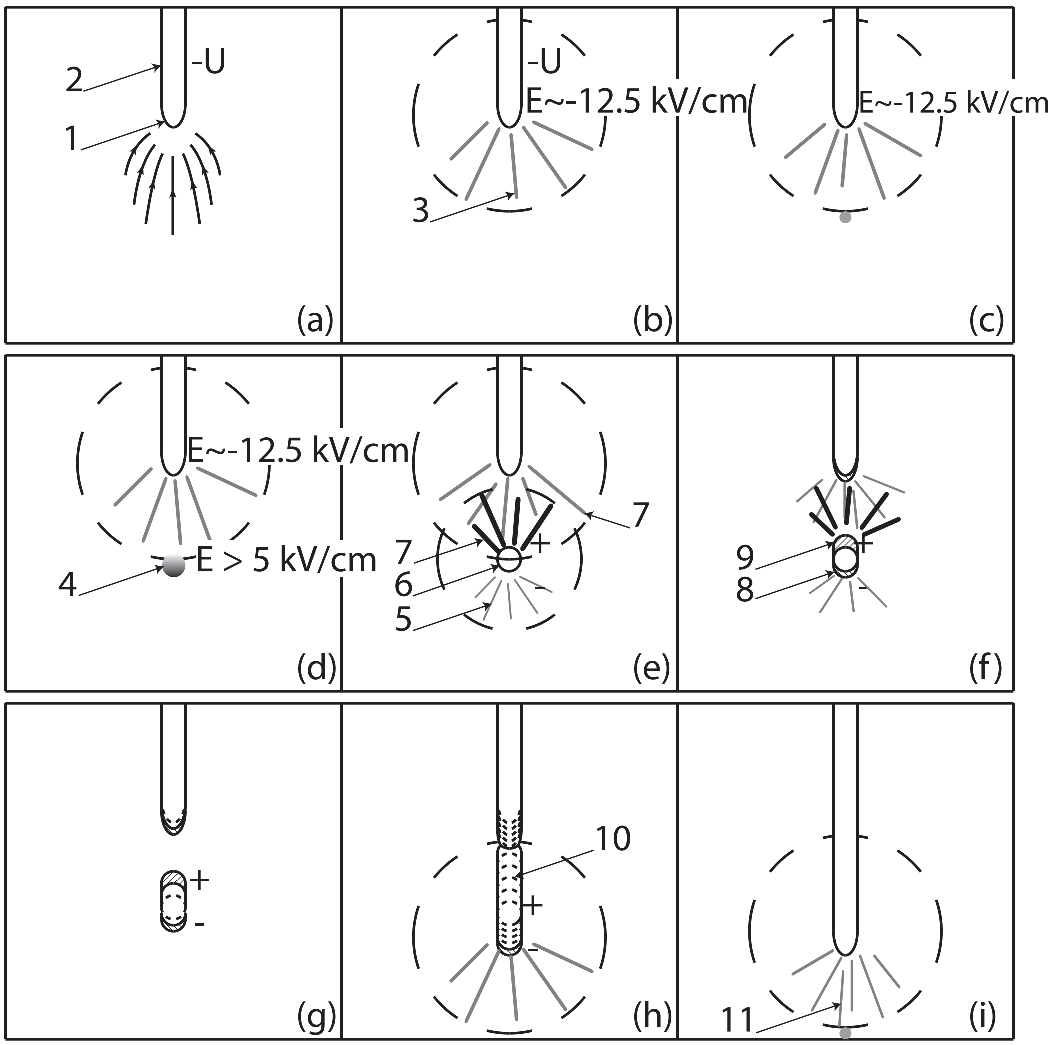

Figure 2.11. Development of a negative leader. Panels (a), (b), (c), (d), (e), (f), (g), (h) and (i) represent different stages of the development. 1, leader tip; 2, primary leader channel; 3, negative streamers in the streamer zone; 4, space stem or plasma spot; 5, negative streamers of the streamer zone associated with the negative space leader; 6, space leader developing from the plasma spot; 7, positive streamers of the streamer zone associated with the positive space leader; 8, negative end of the space leader; 9, positive end of the space leader; 10, leader step; 11, burst of negative streamers. See text for details. Note that the streamer zones are not reproduced in panels (f) and (g) for the sake of clarity.

The latter acquires a potential close to that of the former main negative channel. This process resembles a miniature return stroke of lightning, accompanied by a rapidly rising and just as rapidly falling current impulse in the channel. During this stage, the optical emission of the channel strongly increases giving the impression to the observer that the channel moves by steps (Figure 2.11h). What causes this strong emission is still unclear, even if some processes such a the temperature rise, or the ionization in the channel cover may be suggested. Finally, the negative end of the former space leader turns into the new leader head, a burst of negative streamers develops, and the process is repeated (Figure 2.11i) [*Bazelyan and Raizer*, 2000, pp. 83–89 and p. 255; *Gallimberti et al.*, 2002; *Rakov and Uman*, 2003, p. 136].

The description presented above has been reconstructed from streak photographs of laboratory negative leader discharges. A related sketch is reproduced in Figure 2.12. The main leader advancement, as well as the development of the space leaders and of their respective positive and negative coronas are quite clear in this figure. Numbers 1 to 8 indicate the different regions of the channel visible on the streak picture. The first negative discharge of a lightning or of any laboratory experiment is usually referred to as the *"stepped"* leader and is often said to be discontinuous by opposition of the continuous nature of the positive leader discharge. The motion of a negative leader is continuous, but secondary positive leaders, also continuous, produce a stepwise effect, which originates for the terminology "stepped" leaders [*Bazelyan and Raizer*, 1998, pp. 255–256; 2000, p. 87].

2.2.3 Comparison Between Leaders and Streamers

From a macroscopic point of view, the difference between the streamer and leader bodies is more quantitative than qualitative, i.e., in the degree of ionization and in the strength of the field produced. A streamer absorbs electron avalanches, a leader absorbs streamers. All in all, we can think of the leader process as chain of processes, with one added link to the chain of processes of a streamer breakdown: *avalanches–streamer–(return wave)* is replaced by *avanlanches–streamer–leader–(return wave)* [*Raizer*, 1991, p. 364]. The major difference between leader and

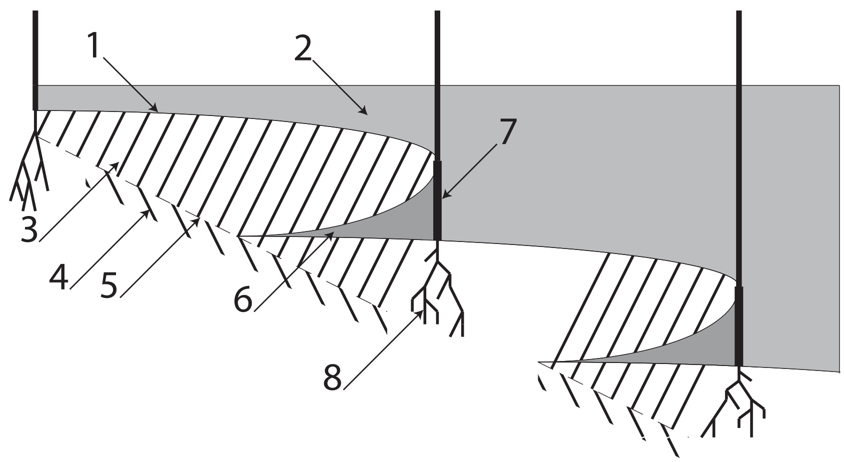

Figure 2.12. Schematic of a streak picture of a negative leader. 1, leader tip; 2, primary leader channel; 3, positive streamers of the streamer zone; 4, negative streamers of the streamer zone; 5, space stem or plasma spot; 6, space leader; 7, leader step; 8, burst of negative streamers [*Bazelyan and Raizer*, 2000, p. 85; *Rakov and Uman*, 2003, p. 136].

streamer channels is the thermodynamic and hydrodynamic conditions. Whereas streamers can hardly propagate in low electric fields, it is thought that leader could propagate in fields as low as a few hundreds V/m at ground pressure [*Gallimberti et al.*, 2002]. *Marshall et al.* [1995] estimate the maximum electric field in thunderstorm around ~1.5 kV/cm. Therefore, the leader process is the natural mechanism of lightning propagation. The extrapolation of results obtained in spark laboratory can be rather easily extended to lightning cases assuming that the lightning initiation mechanisms supply the energy for the development, and replace from this point of view the laboratory electrode. How the lightning discharges are initiated is still an unsolved question [e.g., *Marshall et al.*, 1995; *Dwyer*, 2003; *Behnke et al.*, 2005, and references therein]. For this reason, most models developed in the available literature simply postulate initiation of lightning and put emphasis on the development of the leader part of the lightning discharge, and so does the model that we present, validate and apply in the next chapters.

Chapter 3

Three-Dimensional Fractal Model of Lightning

The material covered in this chapter is mostly taken from a paper submitted for publication in the Journal of Geophysical Research–Atmospheres [*Riousset et al.*, 2006a]. A review of the available lightning models in the current literature has been presented in Chapter 1. This chapter is devoted to the description of the fractal model developed as part of the research work performed for this thesis. Following the discussion about the thunderstorm cloud electric structure presented in Chapter 2 (see Section 2.1), we employ a tripole charge configuration to simulate a lightning producing cloud in our model. The modeling of discharge channels uses the parameters for leader propagations also discussed in Chapter 2 (Section 2.2). We emphasize that the use of fractal model has several advantages as discussed in Chapter 1, one of which is to avoid the modeling of the poorly known microphysical processes governing the lightning discharge initiation and development.

3.1 Model Formulation

The thundercloud and lightning discharge are modeled in a 3-D Cartesian domain. Various possible charge sources have been implemented in the model and are detailed in Appendix A. For the purpose of investigation of lightning discharge, the model of the thundercloud charges described in this section is preferentially used. The alternative potential or charge distributions described in Appendix A are not used in the modeling of lightning discharge but have been extensively used to facilitate testing of the model (see Chapter 4).

The charge distribution in the thunderstorm is reproduced based on a tripole model of the thundercloud [e.g., *Williams*, 1989; *Rakov and Uman*, 2003, p. 69] introduced in Section 2.1 of this thesis. This model is often regarded as an adequate approximation of the charge structure involved in lightning discharges in the convective parts of normally electrified storms [e.g., *Mazur and Ruhnke*, 1998]. The model employs a three layer charge structure above a perfectly electrically conducting (PEC) ground plane. A main negative charge (Q_N) is positioned below the main positive charge (Q_P) and above the lower positive charge (Q_{LP}) (see Figures 2.2, 2.3 and 3.1).

The particular charge configuration used in our modeling closely follows the approach of *Krehbiel et al.* [2004] and *Behnke et al.* [2005]. Each charge layer is assumed to have a cylindrically symmetric disk shape with dimensions chosen based on observations of a storm over Langmuir Laboratory on July 31, 1999, as determined by *Krehbiel et al.* [2004] and summarized in Table 3.1 (see [*Marshall et al.*, 2005] for results concerning the initiation conditions of cloud-to-ground lightning discharges in this storm). In the study by *Krehbiel et al.* [2004], charging currents I_1 and I_2 were introduced between the upper and lower dipoles (i.e., Q_N–Q_P and Q_N–Q_{LP}, respectively) that reproduced the average lightning rates of both cloud-to-ground and intracloud flashes, as determined by the three-dimensional Lightning Mapping Array (LMA). The charging currents were I_1=+1.5 A between the main negative and upper positive, and I_2=−90 mA between the main negative and lower positive charge regions. The resulting variation of the electric field profiles with space and time along the axis of the modeled charge structure reproduced the basic features of balloon-borne electric field soundings through the storm [*Krehbiel et al.*, 2004].

In the present study, the above charging currents were applied until the conditions for initiation of an intracloud discharge between the main negative and upper positive charge regions were satisfied (discussed later in this section). The charge brought by the currents was uniformly distributed in cylindrical disk volumes with dimensions specified in Table 3.1 (see also Figure 3.1). The values of the thundercloud charges at the time of the lightning initiation are also included in

Table 3.1. Charge values, heights and extents for the cylindrical disk model [*Riousset et al.*, 2006a].

Charge Layer	Altitude (km AGL[a])	Depth (km)	Radius (km)	Charge (C)
P	6.75	1.5	4.0	48.7
N	3.75	1.5	3.0	-51.6
LP	2.00	1.5	1.5	2.92

[a]AGL, above ground level

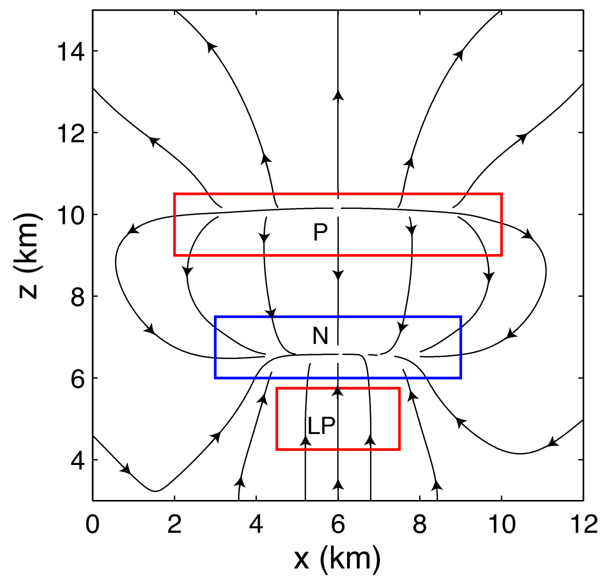

Figure 3.1. A cross-sectional view in the x-z plane at y=6 km of the model thundercloud with upper positive (P), central negative (N) and lower positive (LP) charge layers. Electric field lines produced by the model cloud are also shown for reference [*Riousset et al.*, 2006a].

Table 3.1 for reference. The charge density of the model thunderstorm at the time of discharge initiation is discretized on the grid points of the simulation domain and referred to as the ambient charge density ρ_{amb}. From the charge density, the ambient electric field and potential ($\vec{E}_{amb}$ and ϕ_{amb}) are determined at all grid points within and on the boundaries of the simulation domain.

Open boundary conditions are assumed on the side and upper boundaries. The ground is assumed to be a perfect conductor with potential ϕ_{gnd}=0. Consequently, the electric potential at the boundaries prior to the discharge can be obtained directly from the following expression [e.g., *Liu and Pasko*, 2006]:

$$\phi(\vec{r}) = \phi_{amb}(\vec{r}) = \frac{1}{4\pi\varepsilon_0}\iiint_{V'}\frac{\rho_{amb}(\vec{r'})}{|\vec{r}-\vec{r'}|}dV' + \frac{1}{4\pi\varepsilon_0}\iiint_{V'}\frac{\rho^i_{amb}(\vec{r'_i})}{|\vec{r}-\vec{r'_i}|}dV' \tag{3.1}$$

where $\vec{r}$ defines the coordinate vector of a point at a boundary and $\phi(\vec{r})$ the total potential at this point. The quantity $\rho_{amb}(\vec{r'})$ refers to the ambient charge density at point $\vec{r'}$, while $\rho^i_{amb}(\vec{r'_i})$ designates the ground image of the ambient charge distribution at point $\vec{r'_i}$. Having calculated potential values on the boundaries, we numerically solve Poisson's equation $\nabla^2\phi_{amb} = -\rho_{amb}/\varepsilon_0$ using a SOR algorithm [e.g., *Hockney and Eastwood*, 1981, p. 179] to calculate ϕ_{amb} and $\vec{E}_{amb} = -\vec{\nabla}\phi_{amb}$ inside of the simulation domain. The development of discharge trees starts when the cloud charges reach values such that the ambient field exceeds a predefined initiation threshold E_{init} for a lightning discharge by 10% somewhere in the simulation domain (the related charge values are shown in Table 3.1). From this moment on, the ambient charge distribution remains unchanged.

The exact value of the initiation threshold (i.e., of the electric field E_{init} required to initiate the lightning) is not well established, neither are the mechanisms of the lightning initiation [e.g., *Marshall et al.*, 1995; *Dwyer*, 2003; *Behnke et al.*, 2005, and references therein]. A general consensus exists in the present literature that values around ~1–2 kV/cm at sea level represent a reasonable estimate of fields needed for lightning initiation [e.g., *Gurevich and Zybin*, 2001; *MacGorman et al.*, 2001; *Behnke et al.*, 2005; *Helsdon and Poeppel*, 2005; *Mansell et al.*, 2005; *Marshall et al.*, 2005]. For the purposes of the investigations presented in this thesis, we adopt a value E_{init}=2.16 kV/cm similar to that used in recent studies of *Krehbiel et al.* [2004] and *Marshall et al.* [2005].

We note that the field value ≃2.16 kV/cm at sea level is the minimum field needed to balance the dynamic friction force in air on a relativistic electron with ~1 MeV energy [e.g., *McCarthy and Parks*, 1992; *Gurevich et al.*, 1992; *Roussel-Dupré et al.*, 1994; *Lehtinen et al.*, 1999; *Gurevich and Zybin*, 2001; *Moss et al.*, 2006]. However, we emphasize that similarly to previous work by *Pasko and George* [2002], we use 2.16 kV/cm only as a reference field, making no direct association of the relativistic runaway phenomenon and lightning initiation in our model.

The intracloud discharge develops as a bidirectional leader from the inception point. Although controlled by different processes, the propagation of the positive or negative branches is known to require nearly identical electric fields [e.g., *Raizer*, 1991, p. 375; *Bazelyan and Raizer*, 1998, p. 253; *Rakov and Uman*, 2003, p. 322]. This propagation threshold, denoted $E^{\pm}_{th}$, is about 1 kV/cm in large laboratory gaps (several tens of meters long) [*Raizer*, 1991, p. 362] and can be substantially lower in case of lightning leaders [*Gallimberti et al.*, 2002, and references therein]. Both the lightning initiation E_{init} and propagation $E^{\pm}_{th}$ thresholds represent input parameters in our model. In the framework of the present study, the increases or decreases in these thresholds would lead to corresponding increases or decreases in thundercloud charge values and densities and would not affect any principal conclusions derived from the present study. In this work we simply assume the same initiation and propagation thresholds E_{init}=$E^{\pm}_{th}$=$\pm$2.16 kV/cm, where E^{+}_{th} is positive and represents the propagation threshold of positive leaders, while E^{-}_{th} is negative and represents the propagation threshold of negative leaders. These values are given at sea level, and it is assumed that they vary proportionally to the neutral atmospheric density N at other altitudes. Practical considerations have led us to define every altitude z in our model with respect to the ground level (i.e., z=0 is always referred to as ground level). However, sea level is the usual reference for neutral atmospheric density N. Since ground level and sea level do not always coincide (e.g., when considering measurements in New Mexico thunderstorms), it is judicious to introduce explicitly the difference between ground level and sea level and to denote it as z_{gnd}. Therefore, the initiation and propagation thresholds can be derived at any altitude z above ground using the following representation:

$$E_{init}(z) = E^{\pm}_{th}(z) = \pm 2.16 \frac{N(z + z_{gnd})}{N_0} \text{ [kV/cm]} \tag{3.2}$$

where N_0 is the value of the neutral density at sea level.

As already noted above, the model thundercloud achieves a maturity state sufficient for lightning initiation when the corresponding ambient electric field exceeds the initiation threshold field by 10% somewhere in the simulation domain. As a result of this process, a region of high electric field exceeding the initiation threshold by 0 to 10% is created around the central vertical axis of the simulation domain between the upper positive and central negative charge layers. The inception point is chosen randomly in this region with no weighting based on the ambient electric field magnitude. Thus every point at which $|E_{amb}| \geq |E_{init}|$ have equal probability to initiate the discharge. The leader channel propagates iteratively from this starting point; at each step, one and only one link is added (at either the upper or the lower end of the tree) and the potential is updated to ensure the overall neutrality of the channel. To illustrate the procedure, we start from an existing channel and describe each step required to achieve the next stage of the development of the discharge tree.

We first define the total potential ϕ, which can be viewed as the ambient potential due to thundercloud charges modified by the presence of the lightning trees up to the current stage of development. Further propagation of the channel requires the knowledge of ϕ inside of the domain. How ϕ is determined will be discussed later in this section. At this point, we assume that the total potential has already been established and show how the next segment of the discharge tree is added. By the choice of the new link, we introduce stochasticity in the model. Starting from the existing channel, a new link is chosen among the candidates, which are defined as the possible links between the channel points and the neighboring points where the local electric field exceeds $E_{th}^{\pm}$. For each candidate link i, the local electric field E_i is calculated as $E_i = (\phi^{start} - \phi^{end})/l$, where ϕ^{start} and ϕ^{end} are the total potentials at the tips of the candidate link, and l is the length of the link. Consequently, a positive or negative leader will be able to propagate through a candidate link i if $E_i \geq E_{th}^{+}$ or $E_i \leq E_{th}^{-}$, respectively. Examples of candidates originating from two representative points on an existing discharge tree are shown in Figure 3.2a. The existing tree is represented using solid lines, while the candidate links are represented by dashed lines. Figure 3.2a is plotted in 2-D for the sake of clarity, and an extension to the 3-D geometry actually used by the model is straightforward. The probability of the channel growth associated with candidate link i is assigned as follows [e.g., *Femia et al.*, 1993]:

$$p_i = \frac{|E_i - E_{th}^{\pm}|^{\eta}}{\sum_i |E_i - E_{th}^{\pm}|^{\eta}} \tag{3.3}$$

where η is called the probability sensitivity. The value of η has been derived by *Popov* [2002] to be 1 for streamer discharges in air. No similar derivation exists

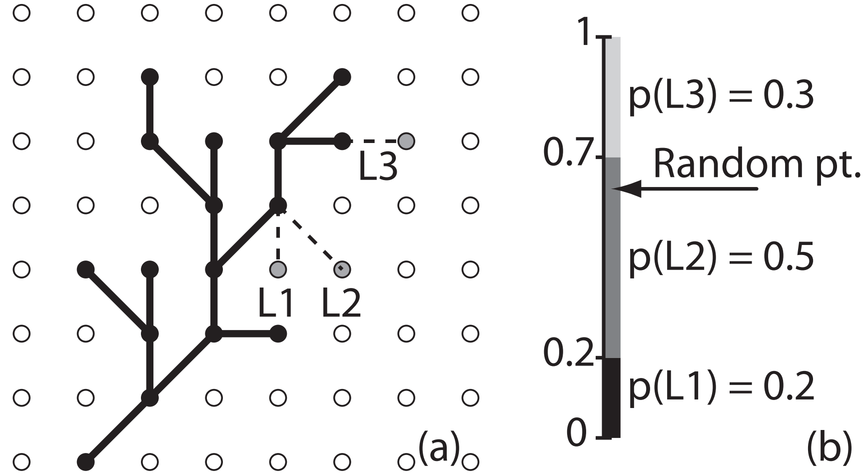

Figure 3.2. Channel extension in a 2-D geometry. (a) Channel links (solid lines) and link candidates (dashed lines); (b) Probability associated with each link. (The values of the probabilities given on this plot are arbitrary and are shown only for two representative points on the existing discharge tree for the purposes of illustration. Real values are derived based on the analysis of potential differences involving all grid points of the existing discharge tree–see text for details.)

for the case of leader discharges. For all calculations presented in this thesis, we adopt η=1, which is a common choice in existing fractal models [e.g., *Niemeyer and Wiesmann*, 1987; *Mansell et al.*, 2002]. The probability associated with each link can be represented as a portion of a segment of unity length (see Figure 3.2b). By picking randomly a point between 0 and 1 on this segment, we select the new link. Therefore, this procedure accounts for both the propensity of the channel to develop in regions of strong electric field and for the stochastic nature of the leader development.

Once the new link has been selected, the potential needs to be redefined in the channel, inside of the domain and at its boundaries. This potential adjustment must account for the overall neutrality of the discharge tree and its equipotentiality. This is achieved in the following way. From the principle of superposition, the total potential in the presence of a conducting tree at each point M inside the simulation domain can be written as $\phi(M) = \phi_{amb}(M) + \phi_{cha}(M)$, where $\phi_{cha}(M)$ is the potential due to the charges induced on the channel. In particular, for points P on the channel, $\phi_{cha}(P) = \phi_0 - \phi_{amb}(P)$ to make the channel an equipotential characterized by the constant potential ϕ_0. A simple iterative procedure is used to determine the value of channel potential ϕ_0 that minimizes the net charge on the channel as described later in this section. At each step of the iteration, the values of $\phi_{cha}(P)$ on the grid points occupied by the channel are fixed and used as an interior boundary condition for solving $\nabla^2\phi_{cha} = 0$ at any point in the simulation domain using SOR algorithm. For these solutions, the values of the potential on boundaries of the simulation domain are taken from potential solutions obtained after the previous link was added and are also assumed fixed. Having applied Poisson's equation to the new result for ϕ_{cha}, but now including the points on the channel in calculation of the Laplacian, we can estimate the charge density ρ_{cha} associated with the channel as $\rho_{cha} = -\varepsilon_0\nabla^2\phi_{cha}$. Since $\nabla^2\phi_{cha} = 0$ everywhere outside the grid points which belong to the discharge trees, ρ_{cha} is confined only to the grid points on the channel. The total charge Q_{cha} on the channel can then be obtained by performing an integration of ρ_{cha} over the volume of grid points associated with the discharge trees as follows: $Q_{cha} = \iiint_V \rho_{cha}(\vec{r})dV$. In addition, the electric dipole moment $\vec{p}$ of the discharge trees is derived for diagnostic purposes as: $\vec{p} = \iiint_V \vec{r}\rho_{cha}(\vec{r})dV$ [e.g., *Zahn*, 1987, p. 139].

The value of ϕ_0 to achieve overall neutrality of the channel, namely Q_{cha}=0, is determined by applying a bisection method [e.g., *Press et al.*, 1992, p. 353]. This root-finding algorithm requires that the solution is known to lie inside a given interval. For the present model, the total potential of the channel ϕ_0 will necessarily lie between the minimum and the maximum of the ambient potential. Because the algorithm quickly converges to the solution, we simply use the extrema values of ϕ_{amb} to bound the solution instead of attempting to estimate ϕ_0 based on its value at the previous stage of the channel development.

Having determined ϕ_0 and ϕ_{cha} as described above, the effect of the channel is known everywhere in the simulation domain following addition of each new link. In particular, the determination of ρ_{cha} enables us to update the contribution of the channel to the potential at the simulation domain boundaries. This is done using equation (3.1) with ϕ_{amb}, ρ_{amb} and ρ^i_{amb} respectively replaced by ϕ_{cha}, ρ_{cha} and ρ^i_{cha}, where ρ^i_{cha} is the ground image of the channel charge. The recalculated values are used for the boundary conditions during the next step of the discharge development. Thus, the update of the simulation domain boundary conditions is always "one link behind" with respect to advancement of the channel. This delay is due to the impossibility to determine the effect of a link on the boundary conditions prior to its establishment. Since the difference is only that due to the addition of a single link, the errors introduced by this approach are expected to be small. Typically, for the simulation results presented Chapter 5, a link modifies the total potential at the boundary by less than 1%.

Finally, recalling that ϕ_{amb} has been previously derived inside of the domain and at its boundaries, the potential at any point M of the domain can be obtained using the principle of superposition $\phi(M) = \phi_{cha}(M) + \phi_{amb}(M)$. At this stage, all requirements are fulfilled and model execution proceeds to development of the next link. This procedure is repeated until no candidate links for further extension can be found or until a point when a channel link reaches the ground. In Chapter 5, we focus on studies of intracloud discharges, which are more probable for thundercloud charge configuration specified at the beginning of this section.

3.2 Simplified Benchmarking Models (SOR-based and MoM-based)

For the purpose of validating the derivation of the electric potential, field and charge densities in the fractal model, we use simplified geometries of the channel solved with different algorithms. This section describes the modifications of the previous model to adapt it to simpler geometries, as well as the method of moments based model employed for comparison of results. The general idea is to solve the same problem using two different methods, first using the SOR algorithm employed by the fractal model described in the previous section, second using the method of moments (MoM).

For the purpose of the aforementioned comparisons, we have chosen to answer the following question: *"What are the electric potential, field and charge distributions created by a linear and a branched metallic conductor placed in a uniform ambient electric field ?"*

This question is investigated using the geometries described in Figure 3.3. For both Figures 3.3a and 3.3b, the problem is solved in a 4 km × 4 km × 4 km

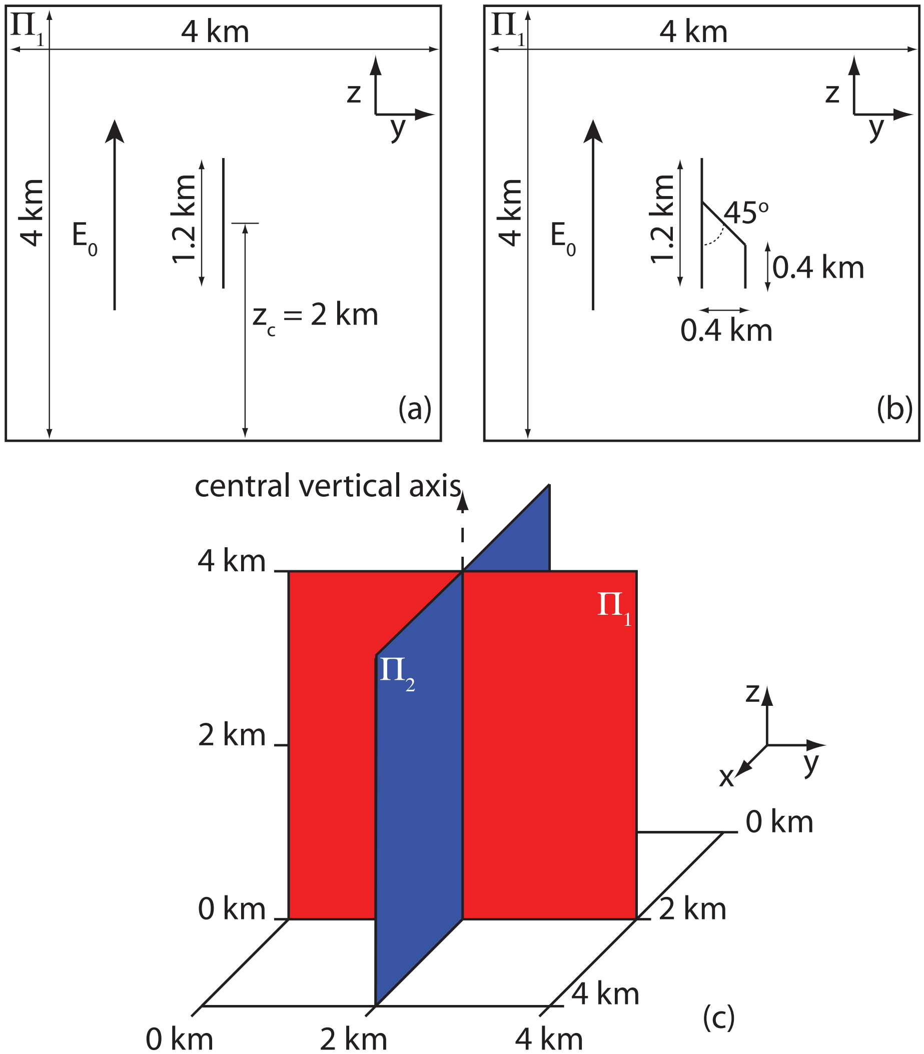

Figure 3.3. (a) Linear metallic conductor in a uniform electric field; (b) Branched metallic conductor in a uniform electric field; (c) Projection planes Π_1 at x=2 km; Π_2 at y=2 km.

simulation domain. The uniform ambient electric field E_0 is equal to 0.3 kV/cm. The wire (branched or not) is placed in the median (y, z) plane Π_1 at $x = 2$ km (see Figure 3.3c). Accounting for limitations described in Appendix B, we investigate two resolutions: a coarse resolution, for which the discretization step is equal to 100 m in x-, y- and z-directions (i.e., the simulation domain is discretized using 41×41×41 grid-points), and a finer resolution with a discretization step equal to 20 m in any direction x, y or z (i.e., the simulation domain is discretized using

$201 \times 201 \times 201$ grid-points).

To solve the two problems illustrated in Figure 3.3, we introduce modifications to the model described in Section 3.1.

First, the derivation of the channel potential ensuring both its equipotentiality and overall neutrality is performed as described in Section 3.1. In particular, the same SOR algorithm is still employed to derive the various potential distributions present in the model (ϕ_{amb} and ϕ_{cha}), the principle of superposition is again applied to derive the total potential ϕ, and the same bisection method is applied to retrieve the potential ϕ_0 of the channel. Similarly the derivations of the electric fields ($\vec{E}_{amb}$, $\vec{E}_{cha}$ and $\vec{E}$), channel charge distribution ρ_{cha}, charge transfer Q_{cha} and electric dipole moment $\vec{p}$ also use the methods discussed in Section 3.1. In addition, we introduce the derivation of the local linear charge density in the channel as $\rho^l_{cha} = \rho_{cha}\,\delta x\,\delta y$, with ρ_{cha} still being the channel volumetric charge density and δx and δy the discretization steps in the x- and y-directions.

The major changes in this version of the model are related to the uses of a uniform ambient field and of a predetermined geometry of the channel. This allows major simplifications. First of all, the knowledge of the channel geometry prior to the derivation of any quantity discards the need of using a tree development algorithm. The probabilistic approach in the fractal algorithm employing the probability p_i (see equation (3.3)) is therefore not used for these testing purposes.

Furthermore, the thundercloud electric field distribution is now replaced by a uniform external (i.e., ambient or applied) electric field. This means that the loading sequence reproducing the thundercloud electric field is no longer needed. Besides, the contribution of the channel to the potential at the boundaries is neglected so that the boundary conditions are greatly simplified. This assumption allows us to enforce the external (or ambient) electric potential E_0 by fixing the potential at the boundaries as follows:

$$\phi(x,y,z) \;=\; \begin{cases} 0 & \text{if } z=0,\ \forall(x,y) \\ -E_0\, z & \text{if } (x,y) \in \text{side boundaries} \\ -E_0\, L_z & \text{if } z = L_z = 4 \text{ km},\ \forall(x,y) \end{cases} \tag{3.4}$$

where L_z is the altitude of the upper boundary of the system. These new boundary conditions replace those used in Section 3.1.

The solutions obtained using the simplified model described above will be discussed in Chapter 4, which is devoted to the validation of the fractal model introduced in Section 3.1. In Chapter 4, we also discuss test solutions of the same problems using the method of moments (MoM). The purpose of the remainder of this section is to introduce and describe the related algorithms.

As in Section 3.1, we ensure the overall neutrality of the channel by adjusting the total potential of the channel. Thus the derivation of this potential is again the keystone of the problem. As previously, the total electric potential ϕ is defined as the superposition of the potential ϕ_{amb} due to the external electric field E_0 and the potential ϕ_{cha} induced by the polarization charges in the channel. Thus at any point M, we have again: $\phi(M) = \phi_{amb}(M) + \phi_{cha}(M)$. In particular, if the channel is made equipotential characterized by the constant ϕ_0, for any point P inside of the channel, $\phi_{cha}(P) = \phi_0 - \phi_{amb}(P)$.

If we let M be designated by the coordinate vector $\vec{r}$ with Cartesian coordinates (x, y, z), the ambient potential at point M can easily be derived as $\phi_{amb}(M) = -E_0\, z$. Assuming that we have somehow derived the linear density of polarization charges in the channel ρ^l_{cha} (how this is achieved will be discussed later in this section), $\phi_{cha}(M)$ can be written [e.g., *Balanis*, 1989, p. 670]:

$$\phi_{cha}(\vec{r}) = \frac{1}{4\pi\varepsilon_0} \int_{source} \frac{\rho^l_{cha}(\vec{r'})}{|\vec{r} - \vec{r'}|} dl' \tag{3.5}$$

where $\vec{r'}$ denotes the source coordinates and dl' is the path of integration. Using now $\phi_{cha}(\vec{r}) = \phi_0 - \phi_{amb}(\vec{r})$ and $\phi_{amb}(\vec{r}) = -E_0\, z$ in equation (3.5) yields to:

$$\phi_0 + E_0\, z = \frac{1}{4\pi\varepsilon_0} \int_{source} \frac{\rho^l_{cha}(\vec{r'})}{|\vec{r} - \vec{r'}|} dl' \tag{3.6}$$

Assuming ϕ_0 known (its derivation is presented hereafter), this equation is solved using the method of moments with “pulse” functions as basis functions to obtain ρ^l_{cha} [e.g., *Balanis*, 1989, pp. 670–677] and the charge of the channel can be calculated by performing an integration of ρ^l_{cha} over the total length of the conductor: $Q_{cha} = \int_{source} \rho^l_{cha}(\vec{r'}) dl'$.

For the simple linear geometry shown in Figure 3.3a, the potential of the conductor, which ensures its overall neutrality, can be derived analytically. If the reference for potential is taken at $z = 0$ (i.e., $\phi(0) = 0$), and if z_c is the altitude of the center of the wire, then the potential in the wire can be written as $\phi_0 = -E_0\, z_c$ for obvious reasons of symmetry [e.g., *Bazelyan and Raizer*, 2000, p. 54]. An analytical solution is not achievable for the case of the branched geometry of Figure 3.3b. We therefore employ an alternative numerical procedure involving the Nelder-Mead simplex method instead [e.g., *Lagarias et al.*, 1998] implemented in standard MATLAB function *fminsearch.m*. This root-finding algorithm converges to the minimum of the function starting from an initial guess on the variable. For the present model, we have chosen to minimize the absolute value of the charge in the channel through the following function: $f(\phi_0) = |Q_{cha}| = \left|\int_{source} \rho^l_{cha}(\vec{r'})dl'\right|$. In addition, we have used $\phi_0 = -E_0\, z_c$ as the initial condition which is the channel potential of the unbranched wire. Any other value ranging between 0 and $-E_0\, L_z$ could have been chosen.

At the end of this procedure, ϕ_{cha} is such that $\phi_{amb} + \phi_{cha} = \phi_0$ inside the channel, for which the equipotentiality is therefore ensured, and that $Q_{cha} = 0$, making the channel overall neutral. Finally, the total potential can be expressed at any point M in space as:

$$\begin{array}{rcccc} \phi(M) & = & \phi_{amb}(M) & + & \phi_{cha}(M) \\ & = & -E_0\, z & + & \frac{1}{4\pi\varepsilon_0}\int_{source} \frac{\rho^l_{cha}(\vec{r'})}{|\vec{r}-\vec{r'}|}dl' \end{array} \tag{3.7}$$

In addition, the electric field is derived using $\vec{E} = -\vec{\nabla}\phi$ and the charge transfer can be estimated using:

$$Q^+_{cha} = \int_{source} \rho^l_{cha}(\vec{r'})\, \delta(\rho^l_{cha}(\vec{r'}))dl' \tag{3.8}$$

where

$$\delta(\xi) = \begin{cases} 1 & \text{if } \xi \geq 0 \\ 0 & \text{else} \end{cases} \tag{3.9}$$

and $\vec{r'}$, dl' still denote the source coordinates and the path of integration.

This model allows comparison of the electric field, potential, linear charge density and charge transfer to the corresponding values of field solutions obtained with the simplified model based on SOR described in the first part of this section.

It should be noted that the two benchmarking models presented in this section employ different algorithms to minimize the charge in the channel (a bisection procedure and a Nelder-Mead simplex method). The agreement between the results produced by the two algorithms will be checked as a part of the validation of the model performed in Chapter 4.

To conclude the discussion in this section we make two additional points concerning the derivation of physical quantities in SOR-based and MoM-based simplified benchmarking models described in this section.

The application of a SOR algorithm to solve Poisson's equation requires that the simulation domain is discretized. In our code, it is achieved using a finite difference method (FDM). This defines a discrete set of points at which the electric potential, field and charge density can be derived. There is no such a constraint for the method of moments (see Appendix B), which allows to derive the potential at any point in space once the channel density has been obtained. However, for the sake of comparison, we choose to derive electric field and potential at the same points of the discretized space using the two methods.

In a discretized domain, the channel occupies a certain number of points depending on the resolution–the finer the resolution, the greater the number of occupied grid points. Again for the sake of comparison, the number of segments used to describe the wire or the piece of wire is chosen such that the channel occupies the same number of grid points in the SOR-based and MoM-based models. Indeed, for the method of moments, the segmentation of the channel can be chosen independently from the simulation domain discretization. For example, in the coarse resolution a 1.2 km linear wire will occupy 13 grid points. Therefore, the number of segments used to discretize the channel by the method of moments will also be chosen to be 13, although it could be any number *a priori*.

Chapter 4

Validation of the Fractal Model

In the process of validation of the fractal approach used for the modeling of lightning discharges, we go through a series of tests. In this chapter, we perform simple checks of the ability of the model to reproduce the electric field and potential in various elementary configurations (i.e., uniformly charged sphere, equipotential linear or branched channels), and to derive the corresponding charge distributions. We also validate the fractal algorithm by comparison with a published model, namely *Pasko et al.*'s [2002] fractal model of blue jets. The overall idea is to quantify any sources of error or imprecision in the fractal lightning model introduced in the previous chapter.

4.1 Electric Potential and Electric Field

The model presented in Chapter 3 is based on the knowledge of the electric potential at any stage of simulation and at any point of the simulation domain. Therefore, it is fundamental to check the accuracy of the algorithm employed for potential calculations. The choice of the use of a successive overrelaxation method (SOR) [e.g., *Hockney and Eastwood*, 1981, p. 179] has been made based on the recommendations provided in [*Hockney and Eastwood*, 1981, p. 168]. We first consider a uniformly charged sphere above a ground plane, for which an analytical solution for the potential is well known. Then we consider two more complicated situations, the first one is a linear metallic wire placed in an ambient uniform electric field, and the second one is a branched wire in the same electric field. For these

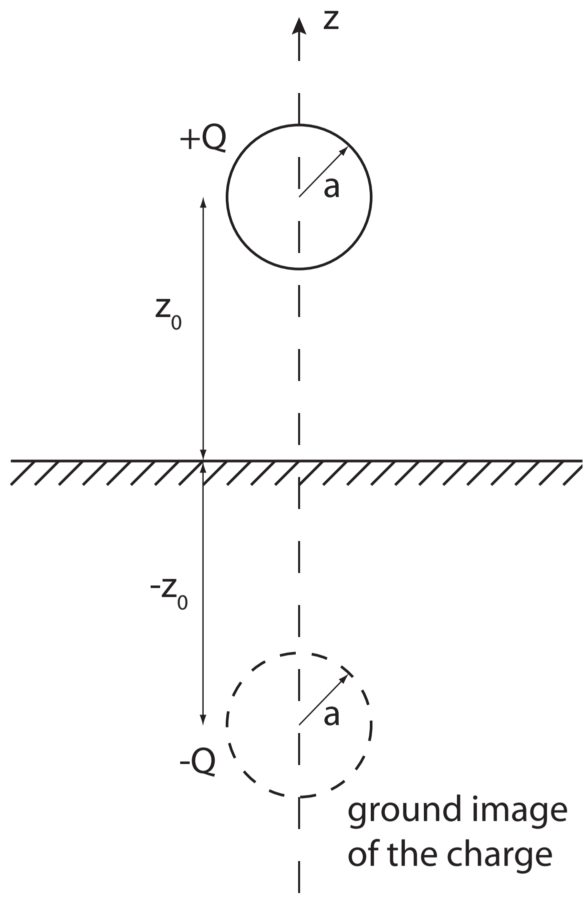

Figure 4.1. Geometry used for the test of a uniformly charged sphere above a perfectly conducting ground plane.

two situations, exact solutions can be easily derived using the method of moments (MoM) [e.g., *Balanis*, 1989, p. 670 and Chapter 3 of this thesis]. We therefore employ the method of moments (MoM) to obtain exact results and to compare them to those produced by the SOR algorithm.

We first consider the electric potential ϕ created by a uniformly charged sphere. The sphere is assumed to have a radius a=1 km and to carry the charge Q=40 C. It is placed on the vertical z-axis, 8 km above a perfectly conducting ground plane (i.e., z_0=8 km), with potential ϕ_{gnd}=0. The ground plane is placed at z=0 km (see Figure 4.1).

For the sake of simplicity, we first derive the potential of a uniformly charged sphere placed at the origin. Then we shift it 8 km along the z-axis, and finally we account for the contribution of its image. Using the integral form of Gauss law $\oiint \vec{E}(\vec{r}) \cdot d\vec{S} = \frac{Q(\vec{r})}{\varepsilon_0}$, where $\vec{r}$ is the coordinate vector in the spherical coordinate system, we can write:

$$\begin{cases} 4\pi r^2 E = & \frac{Q}{\varepsilon_0}\frac{4/3r^3}{4/3a^3} \quad \text{if } |\vec{r}| \leq a \\ 4\pi r^2 E = & \frac{Q}{\varepsilon_0} \quad\quad\quad \text{if } |\vec{r}| \geq a \end{cases} \tag{4.1}$$

Solving equation (4.1) for E, we get:

$$E(\vec{r}) \quad = \begin{cases} \frac{Q}{4\pi\varepsilon_0}\frac{r}{a^3} & \text{if } |\vec{r}| \leq a \\ \frac{Q}{4\pi\varepsilon_0}\frac{1}{r^2} & \text{if } |\vec{r}| \geq a \end{cases} \tag{4.2}$$

and using $\vec{E} = -\vec{\nabla}\phi$, we retrieve the following solutions for potential:

$$\phi(\vec{r}) \quad = \begin{cases} -\frac{Q}{4\pi\varepsilon_0}\frac{r^2}{2a^3} + C_1 & \text{if } |\vec{r}| \leq a \\ \frac{Q}{4\pi\varepsilon_0}\frac{1}{r} + C_2 & \text{if } |\vec{r}| \geq a \end{cases} \tag{4.3}$$

where C_1 and C_2 are two constants to be determined. If we assume $\lim_{r\to\infty} \phi(\vec{r})$=0, then C_2=0. Using the continuity of potential at r=a and solving for C_1, we get: C_1=$+3Q/(8a\pi\varepsilon_0)$. Finally, we can write the total potential as:

$$\phi(\vec{r}) \quad = \begin{cases} -\frac{Q}{4\pi\varepsilon_0}\left(\frac{r^2}{2a^3} - \frac{3}{2a}\right) & \text{if } |\vec{r}| \leq a \\ \frac{Q}{4\pi\varepsilon_0}\frac{1}{r} & \text{if } |\vec{r}| \geq a \end{cases} \tag{4.4}$$

In particular along the vertical axis, we have:

$$\phi(z) \quad = \begin{cases} -\frac{Q}{4\pi\varepsilon_0}\left(\frac{z^2}{2a^3} - \frac{3}{2a}\right) & \text{if } z \leq a \\ \frac{Q}{4\pi\varepsilon_0}\frac{1}{|z|} & \text{if } z \geq a \end{cases} \tag{4.5}$$

If we now shift the sphere along the vertical axis at z=z_0:

$$\phi(z) \quad = \begin{cases} -\frac{Q}{4\pi\varepsilon_0}\left(\frac{(z-z_0)^2}{2a^3} - \frac{3}{2a}\right) & \text{if } |z - z_0| \leq a \\ \frac{Q}{4\pi\varepsilon_0}\frac{1}{|z-z_0|} & \text{if } |z - z_0| \geq a \end{cases} \tag{4.6}$$

The contribution ϕ^i of the ground image of the charge is derived by analogy with equation (4.6), with $Q \rightarrow -Q$ and $z_0 \rightarrow -z_0$:

$$\phi^i(z) = -\frac{Q}{4\pi\varepsilon_0}\frac{1}{z+z_0},\ z \geq 0,\ z_0 \geq a \tag{4.7}$$

Finally, the potential along the z-axis induced by a spherical charge above a perfectly conducting ground plane can be written as follows, accounting for the ground image of the charge:

$$\phi(z) \quad = \begin{cases} -\frac{Q}{4\pi\varepsilon_0}\left(\frac{(z-z_0)^2}{2a^3} - \frac{3}{2a}\right) - \frac{Q}{4\pi\varepsilon_0}\frac{1}{z+z_0} & \text{if } |z-z_0| \leq a \\ \frac{Q}{4\pi\varepsilon_0}\frac{1}{|z-z_0|} - \frac{Q}{4\pi\varepsilon_0}\frac{1}{z+z_0} & \text{if } |z-z_0| \geq a \end{cases} \tag{4.8}$$

We can plot the function expressed in equation (4.8) for z between 0 and 12 km and compare the result with a numerical solution of the same problem using SOR algorithm. In addition, we derived the electric field created by the charge using $\vec{E} = -\vec{\nabla}\phi$, which gives along the z-axis, $E_z = -d\phi/dz$.

The simulation domain is 12 km × 12 km × 12 km, discretized using 61×61×61 grid-points. Hence the space resolution is 200 m in x-, y- and z-directions. We performed two calculations using SOR algorithm, the first assuming closed boundaries with a fixed potential equal to 0 (referred to as *"tin-can model"*), the second using the boundary conditions described in Chapter 3. The potential and electric field along a vertical axis in the center of the simulation domain are plotted in Figures 4.2a and 4.2b, respectively.

For both electric field and potential, the analytical solutions are plotted using a dashed red line, whereas numerical results are plotted in solid green and solid blue for the "tin-can" solution and the open boundary solutions, respectively. We note that the potential assuming equipotential boundaries is in rough agreement with the analytical solution outside of the sphere and far enough from the boundary, while the electric field is in good agreement with analytical solution. However, when we get closer to the boundary, the agreement is lost. When we assumed open boundary conditions on the side and upper boundaries, the match is perfect with the analytical solution for both potential and electric field. We conclude that the model accurately reproduces the potential and electric field of the given charge distribution.

It is very useful to test the ability of the model to calculate the potential induced

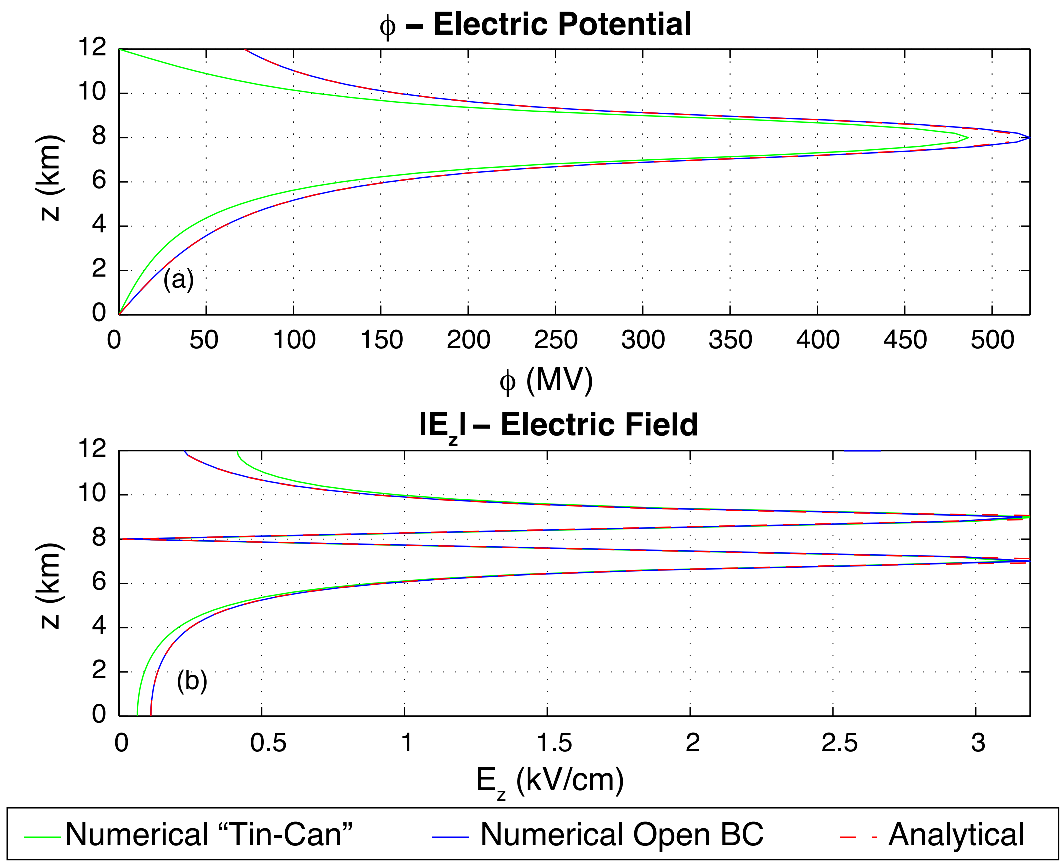

Figure 4.2. Uniformly charged sphere - (a) Electric potential along the central vertical z-axis with equipotential boundaries–so-called “tin-can” solution (solid green line), open boundary conditions (solid blue line) and analytical solution (dot-dashed red line); (b) Electric field corresponding to potential shown in part (a) for equipotential boundaries (solid green line), open boundary conditions (solid blue line) and analytical solution (dot-dashed red line).

by a metallic wire in a uniform electric field. Indeed, the high conductivity of a leader allows to regard it as a metallic wire from an electrical point of view (see discussion in Section 2.2). Consequently, the related tests correspond to a very simplified one-dimensional model of a leader in a uniform field. The first test employs an unbranched wire in a uniform field, while the second one employs a branched conductor in the same field. Both are solved using the method of moments and the SOR-based algorithm introduced in Section 3.2.

Before attempting a quantitative comparison of the results produced by a SOR algorithm and the method of moments, it is wise to check that the qualitative

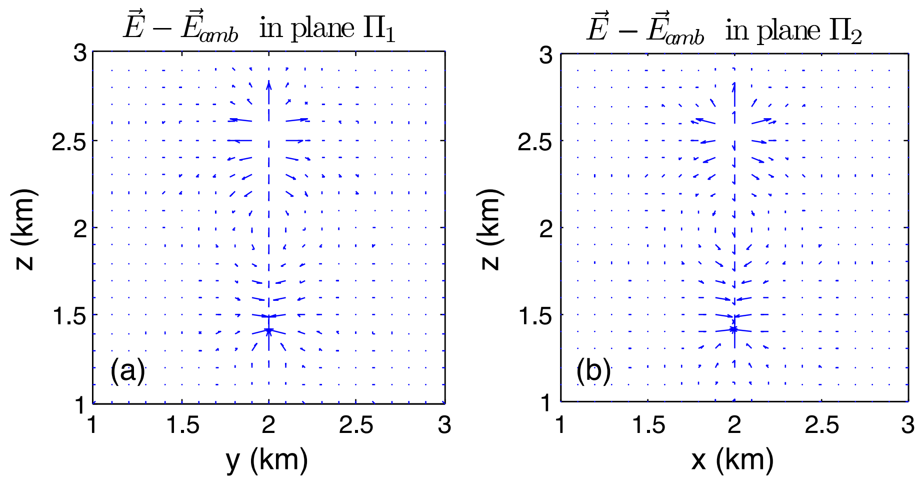

Figure 4.3. Electric field lines created by an unbranched conductor in (a) plane Π_1; (b) plane Π_2.

results are not unreasonable. This can be done by plotting the vector field created by the linear wire in an ambient field in the two principal vertical planes (x=2 km and y=2 km, marked respectively as Π_1 and Π_2 in Figure 3.3c). If we denote again $\vec{E}_0$ as the ambient electric field, $\vec{E}$ total electric field (i.e., the electric field as modified by the presence of the channel), then we can introduce the electric field $\vec{E}_{cha}$ due to the channel $\vec{E}_{cha} = \vec{E} - \vec{E}_0$. The comparison of the projection of $\vec{E}_{cha}$ in the plane Π_1 and Π_2 (Figures 4.3a and 4.3b) gives a good illustration the field lines as well as of the regions of intense field. The direction of the arrows shows the shape of the field lines while their length shows the intensity of the electric field at specified locations.

The inspection of Figures 4.3a and 4.3b shows that the two plots are identical, which is consistent with the overall cylindrical symmetry of the system. In addition, we observe that the field remains undisturbed by the presence of the channel far enough from it. Also it is magnified by the channel at its tips, consistent with expectations (see Section 2.2.2). The same phenomenon occurs with leader channels [e.g, *Bazelyan and Raizer*, 2000, p. 53].

This elementary test confirms that the SOR algorithm produces expected results for a metallic conductor of simple geometry placed in external uniform electric field. Thus, it is now judicious to investigate the quantitative validity of the calculations. If we recall that the method of moments can provide an exact solution for simple geometry, we can compare the two solutions to gain insight into accuracy of SOR-based solutions.

For the unbranched geometry of Figure 3.3a, we plot the total potential, the potential induced by the channel (defined as the difference between the total potential and the ambient potential), and the total electric field along the central vertical axis (see Figure 3.3c) as derived using SOR method and the method of moments for the coarse and the finer resolution (respectively panels (a), (b) and (c) of Figures 4.4 and 4.5). The agreement is quite good for all three functions, especially when the discretization is improved. It becomes better and better as we move away from the channel. We can notice that in both cases of Figures 4.4 and 4.5, the SOR algorithm slightly underestimates the electric field and potential due to the induced charges on the channel. However the error is relatively low as will be shown later in this chapter.

Another point that should be noticed is that total electric field is not zero at the tip of the wire (z=2.6 km), this is true for both cases shown in Figures 4.4c and 4.5c, but is especially visible for the first one. This is easily explained if we recall that the electric field is derived by finite differences in our model. If we denote δx, δy, δz, the discretization steps along the x-, y-, and z-axes, respectively, then for any point M of the domain with coordinates (x, y, z), the magnitude E of the electric field at this point can be derived from the following equation:

$$\begin{aligned} E(x,y,z)^2 = & \\ & \left(-\frac{\phi(x+\delta x,y,z)-\phi(x-\delta x,y,z)}{2\delta x}\right)^2 + \\ & \left(-\frac{\phi(x,y+\delta y,z)-\phi(x,y-\delta y,z)}{2\delta y}\right)^2 + \\ & \left(-\frac{\phi(x,y,z+\delta z)-\phi(x,y,z-\delta z)}{2\delta z}\right)^2 \end{aligned} \tag{4.9}$$

In particular, if M belongs to the channel, $\phi(x + \delta x, y, z) = \phi(x - \delta x, y, z)$ and $\phi(x, y + \delta y, z) = \phi(x, y - \delta y, z)$ and consequently $E(x, y, z) = |\phi(x, y, z + \delta z) - \phi(x, y, z + \delta z)|/(2\delta z)$. In the body of an equipotential channel, we also have $\phi(x, y, z + \delta z) = \phi(x, y, z - \delta z)$ and therefore $E(x, y, z)$=0 if M is in the chan-

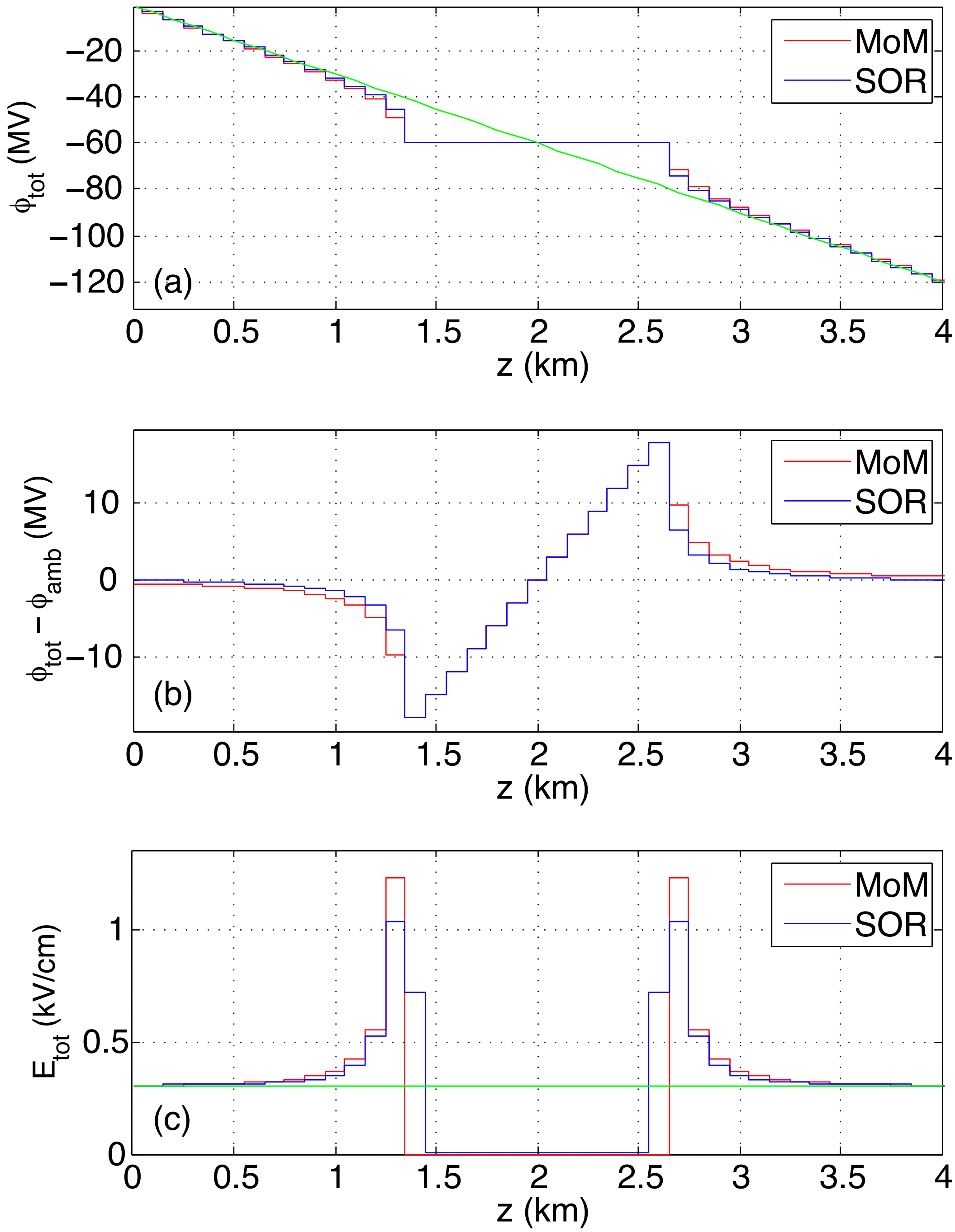

Figure 4.4. Comparison of results from MoM (red lines) and SOR (blue lines) based models for a space resolution of 100 m in x-, y- and z-directions. All values are given for an unbranched conductor placed on the central vertical axis of the simulation domain. All graphs are plotted along this axis. (a) Total potential, with ambient potential plotted in green for reference; (b) Potential of the wire (i.e., total potential minus ambient potential); (c) Total electric field, with ambient electric field plotted in green for reference.

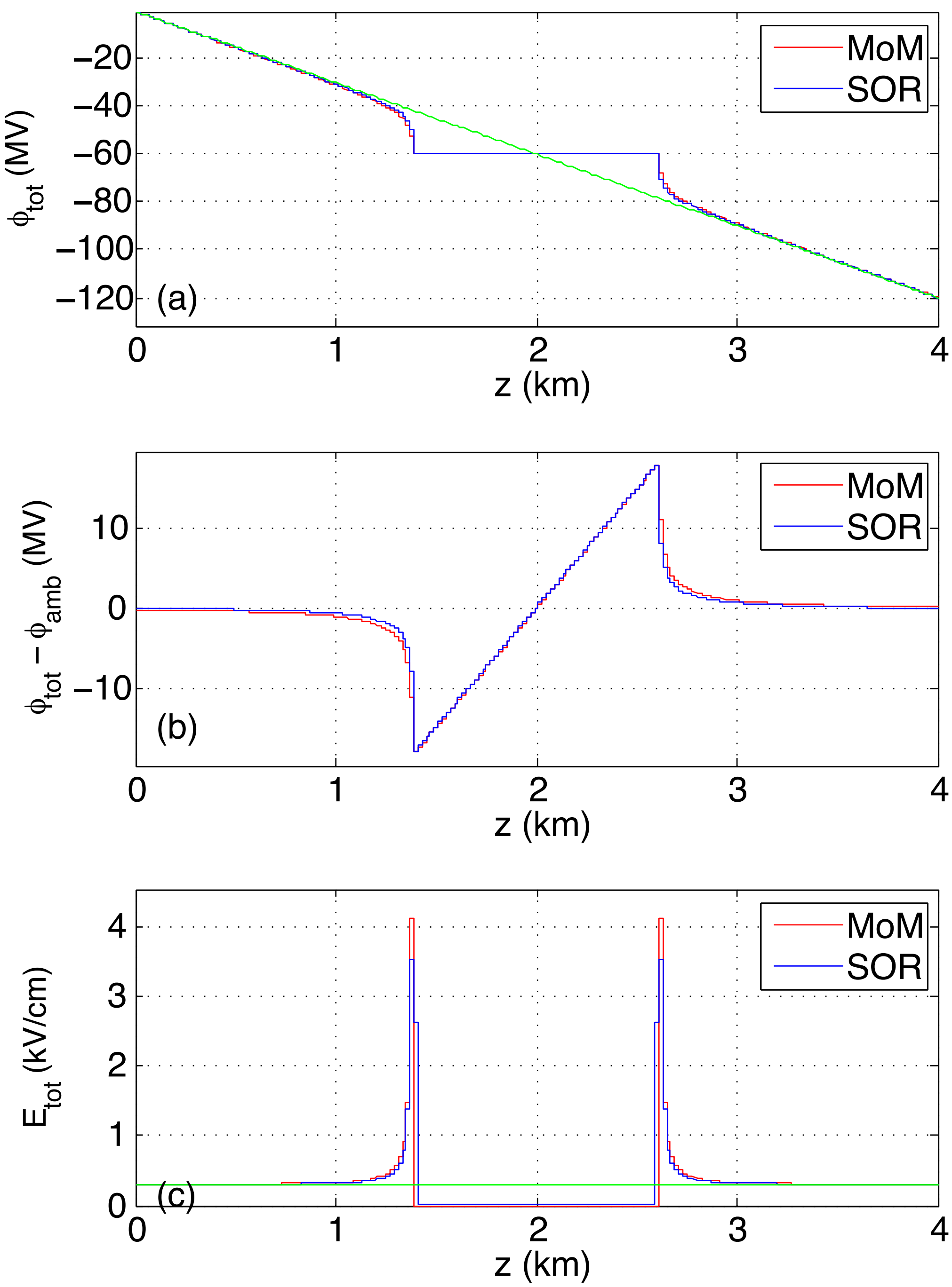

Figure 4.5. Comparison of results from MoM (red lines) and SOR (blue lines) based models for a space resolution of 20 m in x-, y- and z-directions. All values are given for an unbranched conductor placed on the central vertical axis of the simulation domain. All graphs are plotted along this axis. (a) Total potential, with ambient potential plotted in green for reference; (b) Potential of the wire (i.e., total potential minus ambient potential); (c) Total electric field, with ambient electric field plotted in green for reference.

nel. If we still consider M inside of the channel but further assume that M is located at the upper tip, the overall cylindrical symmetry of the system still imposes $\phi(x+\delta x, y, z) = \phi(x-\delta x, y, z)$ and $\phi(x, y+\delta y, z) = \phi(x, y-\delta y, z)$, but now $\phi(x, y, z+\delta z) \neq \phi(x, y, z-\delta z)$. Indeed, if M is at the upper tip of the channel, the next grid point in z-direction defined by the coordinates $(x, y, z+\delta z)$ does not belong to the channel, and therefore is not included in the equipotentiality condition on the channel. Because this point is still used in the derivation of the electric field (see equation (4.9)), then $E(x, y, z) \neq 0$ although M is in the channel. In reality, $\delta z \rightarrow 0$, and therefore $\phi(x, y, z+\delta z) \rightarrow \phi(x, y, z-\delta z)$ and $E(x, y, z) \rightarrow 0$. This explains the discrepancy at the upper tip of the wire. The same reasoning can be made to explain the discrepancy at the lower tip. Nevertheless, the agreement is good, and we still observe the field enhancement at the tips of the wire noticed in the discussion of Figure 4.3.

To further quantify numerical differences between SOR and MoM solutions, we derived and plotted the relative errors for the total potential and electric field in the plane Π_1. The results are shown in Figure 4.6 for the coarse resolution and in Figure 4.7 for the finer one. The relative error $\epsilon_\phi(M)$ at point M for the total potential ϕ is derived as:

$$\epsilon_\phi(M) = \left| \frac{\phi_{\mathrm{SOR}}(M) - \phi_{\mathrm{MoM}}(M)}{\phi_{\mathrm{MoM}}(M)} \right| \times 100\,[\%] \tag{4.10}$$

where $\phi_{\mathrm{SOR}}(M)$ is the total potential derived at point M using a SOR algorithm and $\phi_{\mathrm{MoM}}(M)$, the same value but derived using the method of moments. Similarly and with obvious notations, the relative error $\epsilon_E(M)$ for the norm of the total electric field can be written as:

$$\epsilon_E(M) = \left| \frac{E_{\mathrm{SOR}}(M) - E_{\mathrm{MoM}}(M)}{E_{\mathrm{MoM}}(M)} \right| \times 100\,[\%] \tag{4.11}$$

Figures 4.6a and 4.7a reveal that the error is maximum at the lower boundary (i.e., z=0 km). It is high for low values of z but diminishes as z increases. Elsewhere the error on the total potential is relatively low, does not exceed 7% whatever the resolution considered, and is maximum at the tip of the channel.

The high error at z=0 can easily be explained. It is mainly due to the boundary

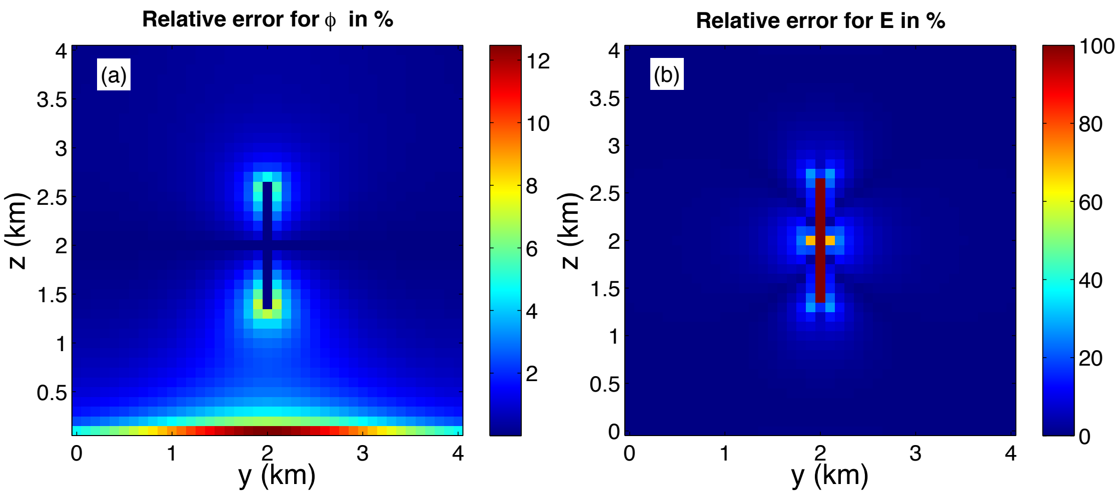

Figure 4.6. Comparison of results from MoM and SOR based models for a space resolution of 100 m in x-, y- and z-directions. All values are given for an unbranched conductor placed on the central vertical axis of the simulation domain. (a) Relative error for the electric potential in the plane Π_1; (b) Relative error for the electric field in the same plane.

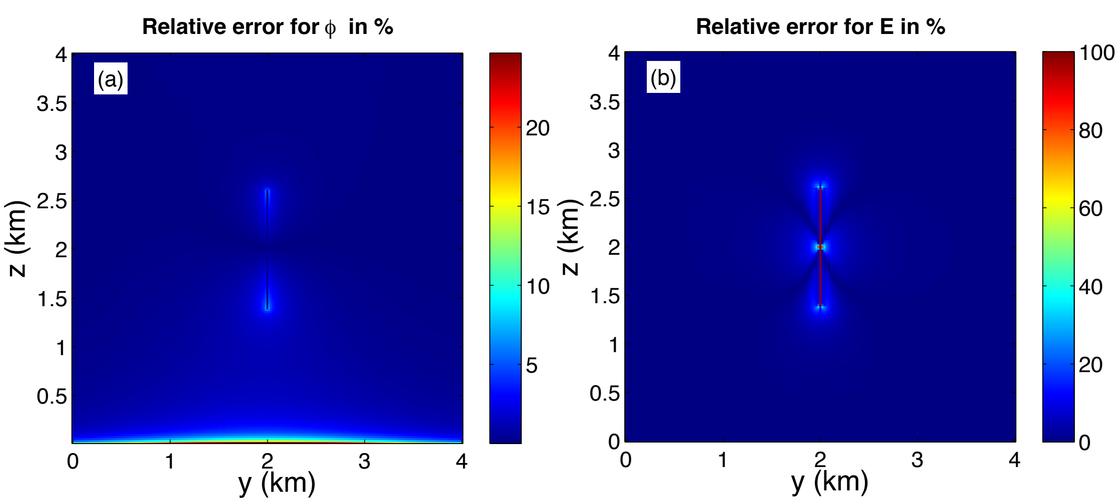

Figure 4.7. Comparison of results from MoM and SOR based models for a space resolution of 20 m in x-, y- and z-directions. All values are given for an unbranched conductor placed on the central vertical axis of the simulation domain. (a) Relative error for the electric potential in the plane Π_1; (b) Relative error for the electric field in the same plane.

conditions. While equipotential planes are used to create the ambient field E_0 in the SOR-based model, no such planes are required in the MoM-based model (see Section 3.2). This difference is responsible for the error observed at $z = 0$ km. If we recall equation (3.4) and assume $\phi_{\mathrm{MoM}}(z{=}0 \text{ km}) \neq 0$, then we see that fixing $\phi_{\mathrm{SOR}}(z{=}0 \text{ km}) \rightarrow 0$ implies $\epsilon_\phi(M) \rightarrow 100\%$ in equation (4.10) if M belongs to the plane $z{=}0$ km. In addition, we note that an SOR algorithm uses the value derived at the surrounding points to derive the potential at a point M of the simulation domain, thus the error observed at $z{=}0$ "propagates" on a range of low values of z. The error around the tip is due to an intrinsic limitation of SOR algorithm, and is also present for more complicated geometries as will be discussed later in this chapter.

In Figures 4.6b and 4.7b showing electric field solutions, we no longer see a large error at the lower boundary, but now the error seems to be larger in the channel body, around the center of the channel and at its tips. If we recall that at the lower boundary, the electric field will not be zero, then there is no reason for equation (4.11) to be large for low values of z. However, because the channel is equipotential, the electric field along its body is equal to zero, and therefore, $\epsilon_E(M) \rightarrow \infty$ if M is on the channel. Otherwise, the error is maximum close to the tip and is consistent with an intrinsic limitation of the SOR algorithm, since the electric field is found by differentiation of the potential.

An error also appears around the center of the channel. The observation of Figure 4.3 shows that the lines of electric field converge at the tips of the channel (which we call "nodes" of field lines) and loop around a point located at the center of the channel (which we call a "center" of field lines). When we get closer and closer to the center, the concentration of field lines may increase beyond the discretization mesh and therefore, the electric field may not be accurately reproduced by the SOR code. This is not a problem when using the method of moments, because of its ability to return exact solutions at any point in space. This hypothesis tends to be confirmed by the fact that the region of error around the center of the channel diminishes when the resolution increases (see Figures 4.6b and 4.7b). All in all, the error does not exceed $\sim$30%.

It is interesting to compare the exact result of the method of moments using a fine resolution and the solution to the same problem using a SOR method with a coarser resolution. The first solution can be regarded as the exact solution in an ideal case where we could find the detailed distribution of potential and electric field, while the latter actually corresponds to achievable precision in the fractal model detailed in Chapter 3. The comparison of the total electric potential, channel induced potential and total electric field along the main central axis are shown in panels (a), (b) and (c) of Figure 4.8, respectively.

Figures 4.8a and 4.8b show that the agreement between the derived potentials in each case is very good, except that the SOR derivations tend to overestimate the potential. Obviously, the precision is better for the method of moments, due to its better spatial resolution.

The interpretation of Figure 4.8c is more complex. The SOR algorithm in a coarse resolution is unable to reproduce the large enhancement of the electric field close to the tip. This is due to the fact that the closest point to the channel for the used resolution is one hundred meter away from the tip, i.e., in a region where the field enhancement is substantially reduced. With a 20 m resolution in all directions, the method of moments is perfectly able to reproduce this field enhancement.

Nonetheless, we can see that even with a coarse resolution, the SOR algorithm returns a good approximation of the real values of the electric potential and electric field at large distances from the channel.

In the calculations discussed above, we have checked the validity of the SOR algorithm used in our fractal model for the simple case of an unbranched channel. We now apply the same procedure to a more complicated geometry, namely the branched channel shown in Figure 3.3b.

Again, we first check that field due to the charges induced on the channel $\vec{E}_{cha}$ (as defined previously) are in qualitative agreement with expectations. The projections of $\vec{E}_{cha}$ in the planes Π_1 and Π_2 (see Figure 3.3c) give a good illustration of the geometry of the field lines as well as of the regions of intense field. In Figure 4.9a, we see that the tips of an equipotential wire are associated with strong electric field enhancements. The enhancement of the field is lower around the lower tips than around the upper one. The projection in plane Π_2 of the branched channel (Figure 4.9b) is generally similar to that of the unbranched channel (Figure 4.3b). Due to the presence of two lower branches instead of one, the field enhancement in

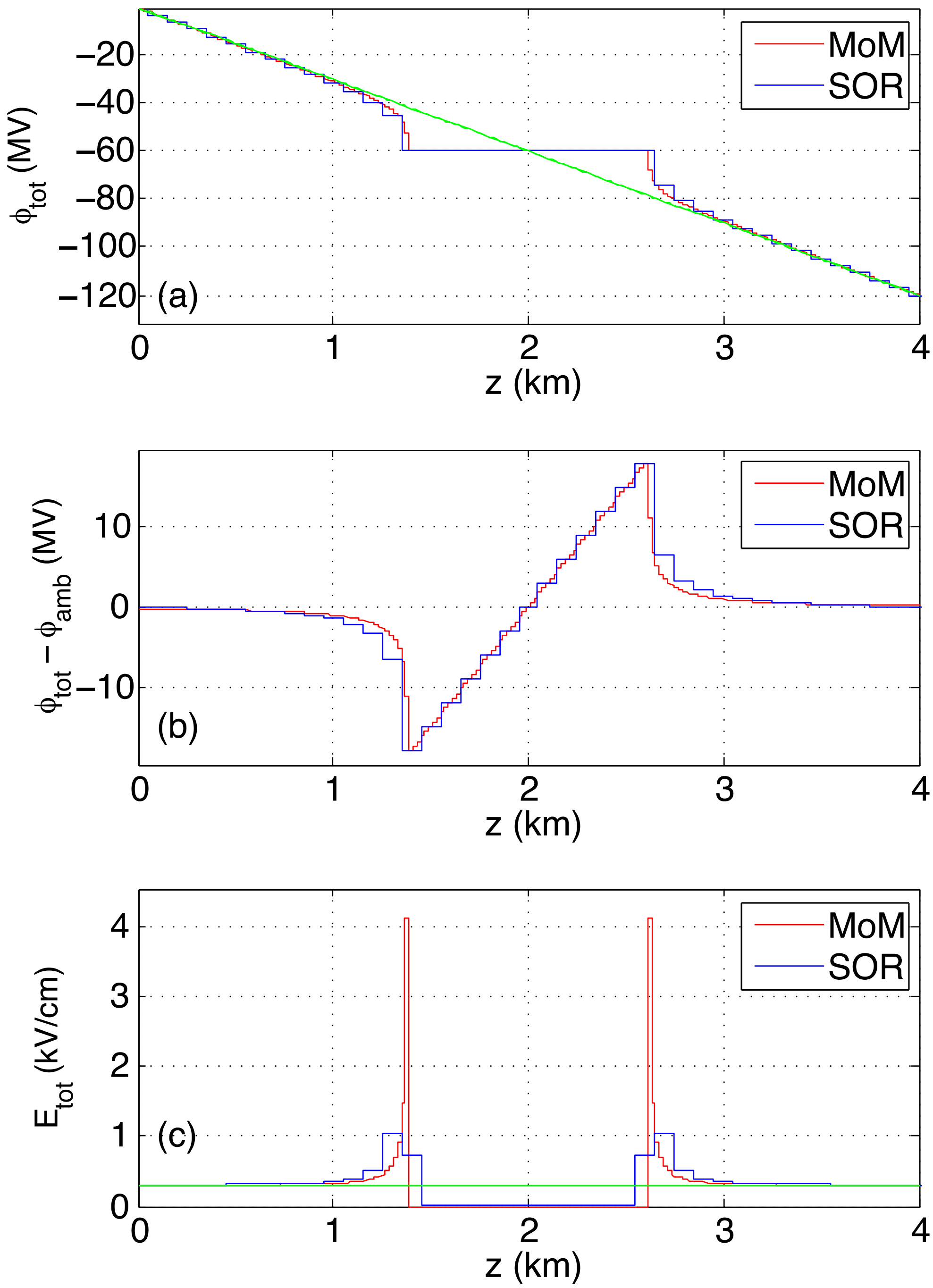

Figure 4.8. Comparison of results from MoM code in fine resolution, 20 m in x-, y- and z-directions (red lines) and from SOR algorithm in coarse resolution, 100 m in x-, y- and z-directions (blue lines). All values are given for an unbranched conductor placed on the central vertical axis of the simulation domain. All graphs are plotted along this axis. (a) Total potential, with ambient potential plotted in green for reference; (b) Potential of the wire (i.e., total potential minus ambient potential); (c) Total electric field, with ambient electric field plotted in green for reference.

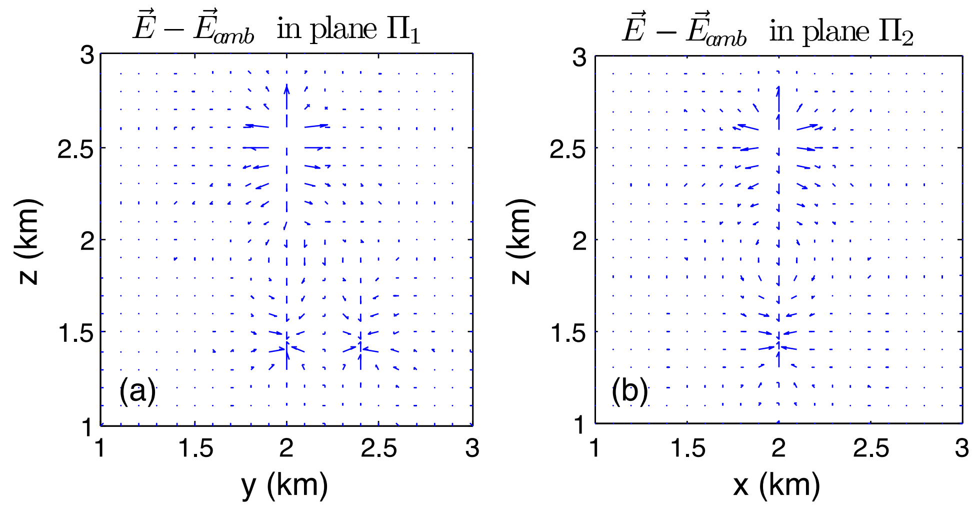

Figure 4.9. Electric field lines created by a branched conductor in (a) plane Π_1; (b) plane Π_2.

the lower part of the plot is expected to be distributed between these two branches, and therefore the field magnification should be greater at the upper tip. This is indeed confirmed by Figure 4.9a.

If we compare total potential along the central vertical axis for the branched channel as derived using SOR method and the method of moments, we see that both methods agree on the value of the potential in the channel ($\sim$$-57$ MV) for both resolutions as shown in Figures 4.10a and 4.11a. From Figures 4.10b and 4.11b, we see that similarly to the results obtained for an unbranched channel, the SOR solution slightly underestimates the real values of the potential close to the channel. However, the overall agreement remains very good. The agreement between the total electric field as derived using each algorithm (SOR and MoM) is not as good especially at low resolutions (Figure 4.10c). The agreement is improved at some distance from the channel, but close to and inside of the channel, the difference between the two methods of derivation is significant. For a finer resolution (Figure 4.11c), the agreement is good even inside of the channel except at the branching point.

An important point to note is that whatever the validity of the charge derivation (to be discussed in the next section), the resulting potential derived to ensure overall neutrality of the channel is the same either using the Nelder-Mead simplex

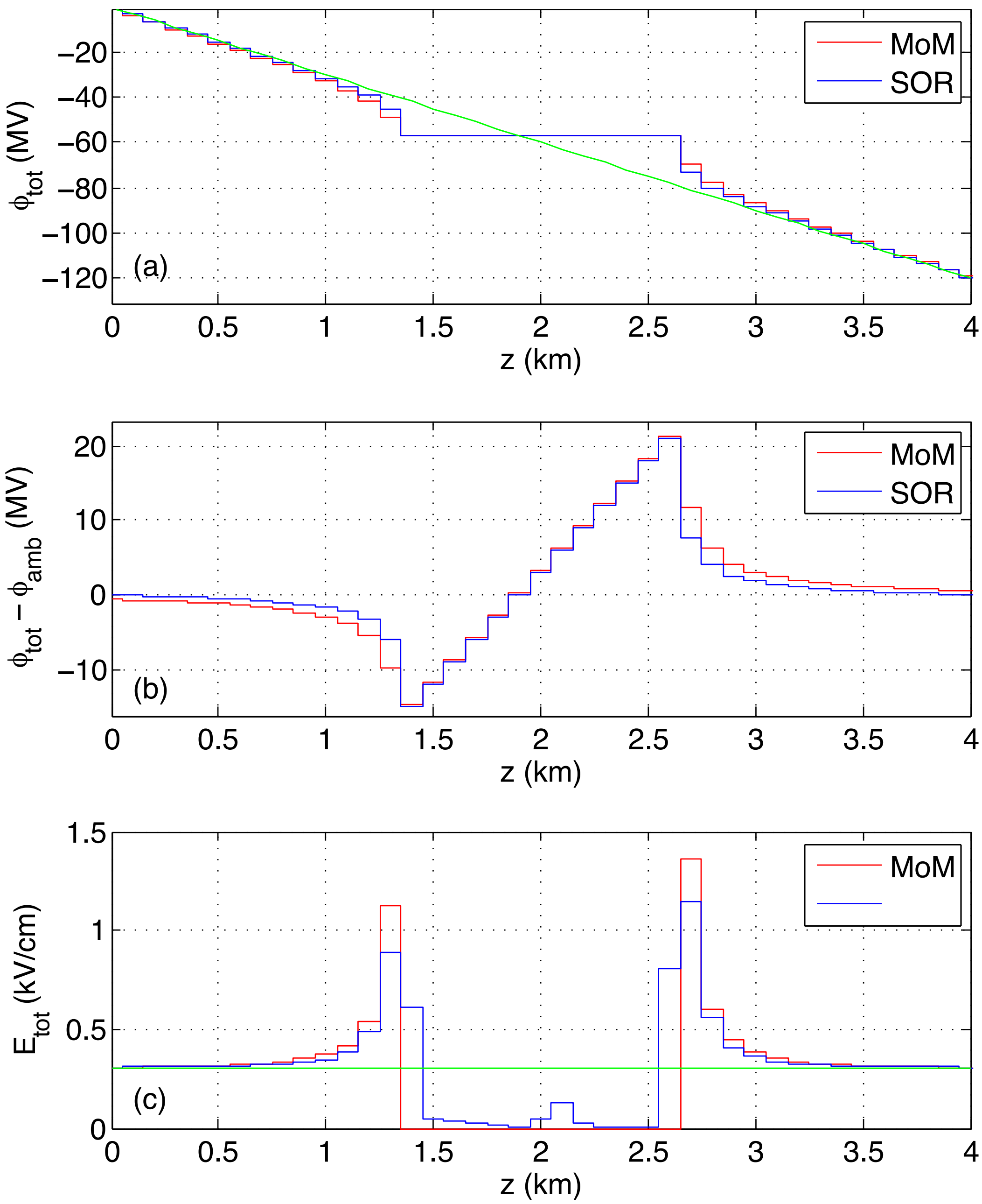

Figure 4.10. Comparison of results from MoM (red lines) and SOR (blue lines) based models for a space resolution of 100 m in x-, y- and z-directions. All values are given for a branched conductor of geometry shown in Figure 3.3b. All graphs are plotted along the central vertical axis of the simulation domain. (a) Total potential, with ambient potential plotted in green for reference; (b) Potential of the wire (i.e., total potential minus ambient potential); (c) Total electric field, with ambient electric field plotted in green for reference.

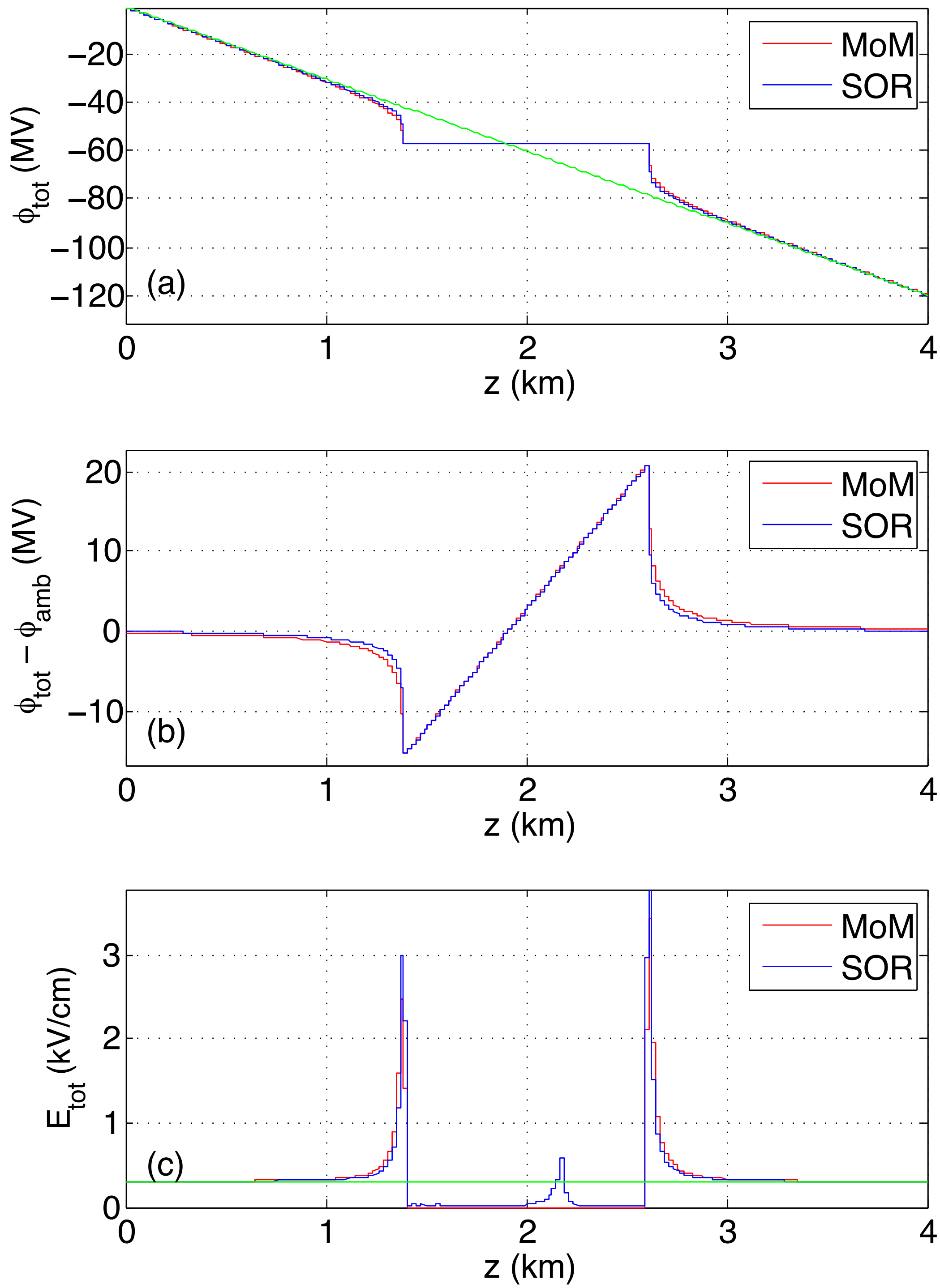

Figure 4.11. Comparison of results from MoM (red lines) and SOR (blue lines) based models for a space resolution of 20 m in x-, y- and z-directions. All values are given for a branched conductor of geometry shown in Figure 3.3b. All graphs are plotted along the central vertical axis of the simulation domain. (a) Total potential, with ambient potential plotted in green for reference; (b) Potential of the wire (i.e., total potential minus ambient potential); (c) Total electric field, with ambient electric field plotted in green for reference.

method or the bisection method. We note that the SOR method tends to underestimate the actual value of the electric potential especially close to the tip. This had been already noticed in the studies of an unbranched channel reported earlier in this section.

Similar to the unbranched channel, the use of a finite difference method to derive the electric field (equation (4.9)) introduces an error at the tips of the channel, which further propagates to the closest surrounding grid points. A second important feature to note is the discrepancy between the electric field derived using the two methods (Figures 4.10c and 4.11c) close to the center of the simulation domain. In a perfect conductor, as it has been assumed in this case of study, the electric field is expected to be zero at any point of the channel. This is not true when we look at the results returned by the SOR algorithm. There are two possible explanations for this. Because the system is no longer symmetric, $\phi(x, y + \delta y, z) \neq \phi(x, y - \delta y, z)$ and $E(x, y, z)$ can be non-zero for a point M with coordinates (x, y, z) inside of the channel. If we further recall that the electric field at the point M in the channel is derived using surrounding points, which are not necessarily in the channel, then using equation (4.9), we can conclude that it is possible to obtain non-zero field solutions on the channel. This idea is confirmed by the fact that this effect diminishes with an improved resolution (Figure 4.11c) and becomes confined to region of junction of branches. Another possible explanation would be the inability of SOR algorithm to accurately reproduce the region around a field line center, that we noticed in the study of the linear channel. Figure 4.9 shows that such a point probably exists close to the center of the simulation domain (x=y=z=2 km).

We now quantify the relative error between results obtained with the SOR-based and MoM-based models. Using the same definition for $\epsilon_\phi(M)$ and $\epsilon_E(M)$ as previously, we plot the relative error for the total electric field and potential in the plane Π_1 for the two considered resolutions (100 m and 20 m in every direction) (see Figures 4.12 and 4.13). Similarly to the linear channel, we note that the error on the potential is essentially concentrated at the tips of the channel and at the lower boundary. Around the region occupied by the channel, the error is limited to $\sim$10%. We also observe the same large relative error in the channel internal electric field as well as a discrepancy around the channel tips. The main information given

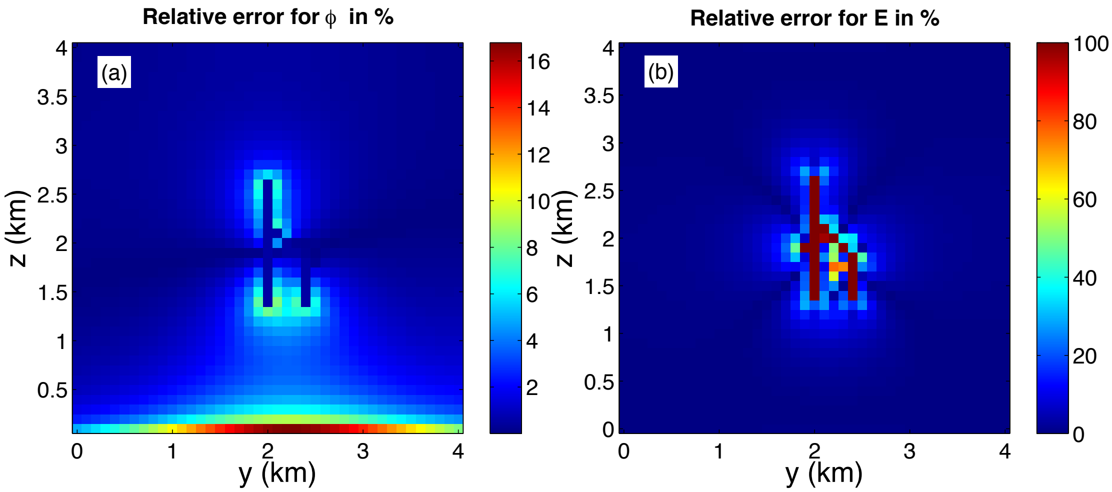

Figure 4.12. Comparison of results from MoM and SOR based models for a space resolution of 100 m in x-, y- and z-directions. All values are given for a branched conductor of geometry shown in Figure 3.3b. (a) Relative error for the electric potential in the plane Π_1; (b) Relative error for the electric field in the same plane.

by these plots is the existence of a significant error (a factor 2 or 3) between the branches when the electric field is derived using a coarse resolution.

The relative errors in the electric field and potential close to the lower boundary and the channel tips can be explained using the reasoning applied for the case of an unbranched conductor. Also, we note that the same intrinsic limitations of the SOR method which have been noticed for the previously considered unbranched case can be recalled to explain error at the tips either for the potential or for the electric field.

The main difference between an unbranched and a branched channel in terms of observed errors lies in the region close to the branching point. The presence of a neighboring branch is more important for the derivation of the local electric field and potential in this region than anywhere else (Figures 4.12 and 4.13). A finer resolution naturally leads to a better description of the electric field and potential in the simulation domain. In particular, the details of the influence of the branching are quite well resolved in Figure 4.13b and the problem is limited to a small region around the branching point. For a coarser resolution, there is a spreading of this error due to the inability of the model to describe the branching point accurately (Figure 4.13a). Thus, improving the resolution leads to a "displacement" of the

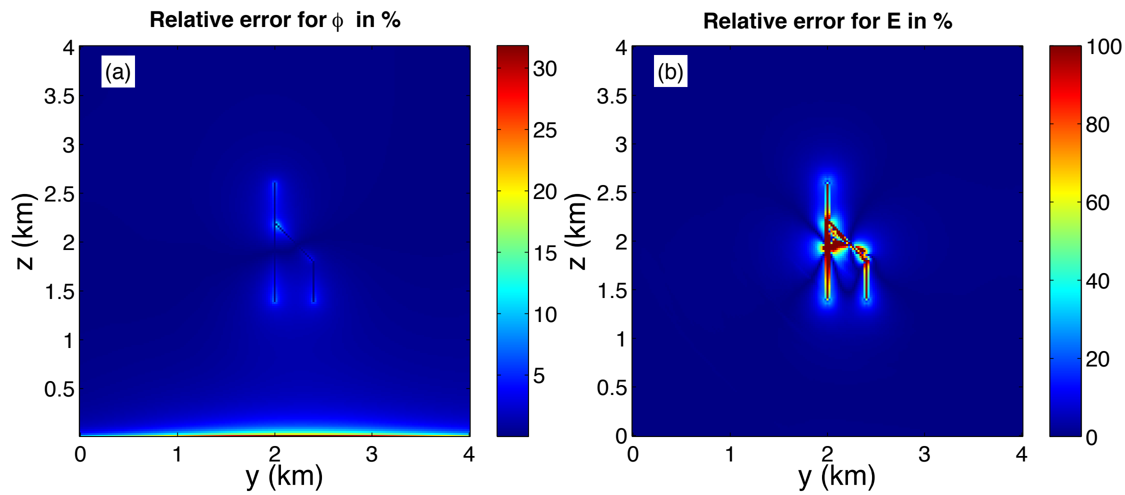

Figure 4.13. Comparison of results from MoM and SOR based models for a space resolution of 20 m in x-, y- and z-directions. All values are given for a branched conductor of geometry shown in Figure 3.3b. (a) Relative error for the electric potential in the plane Π_1; (b) Relative error for the electric field in the same plane.

error towards the branching points and it is expected that the problem would ultimately disappear for an excessively fine resolution. Yet, a detailed inspection of Figures 4.12b and 4.13b shows that the error is not only concentrated at the branching point but in a wider area expanding farther between the two branches. We previously noticed that whatever the resolution, an SOR algorithm would probably not be able to accurately reproduce the field magnitude around a field line center. Besides, a careful inspection of Figure 4.9a suggests the existence of a field line center in a region below the branching point and probably around the severe error region observed in Figure 4.13b. Therefore the presence of such a field line center may be responsible for the error existing in the derivation of the electric field in this region.

Nonetheless, it should be noted that only potential inside of the channel and at some distance from it are most important for fractal modeling of leader development (see Section 3.1, in particular equation (3.3), and Section 4.4 in this chapter). Therefore, errors close to the branching points of the leader trees are not critical from the prospect of fractal modeling.

If we compare the total potential derived using a coarse resolution with a SOR algorithm and the same potential derived using a finer resolution with the method

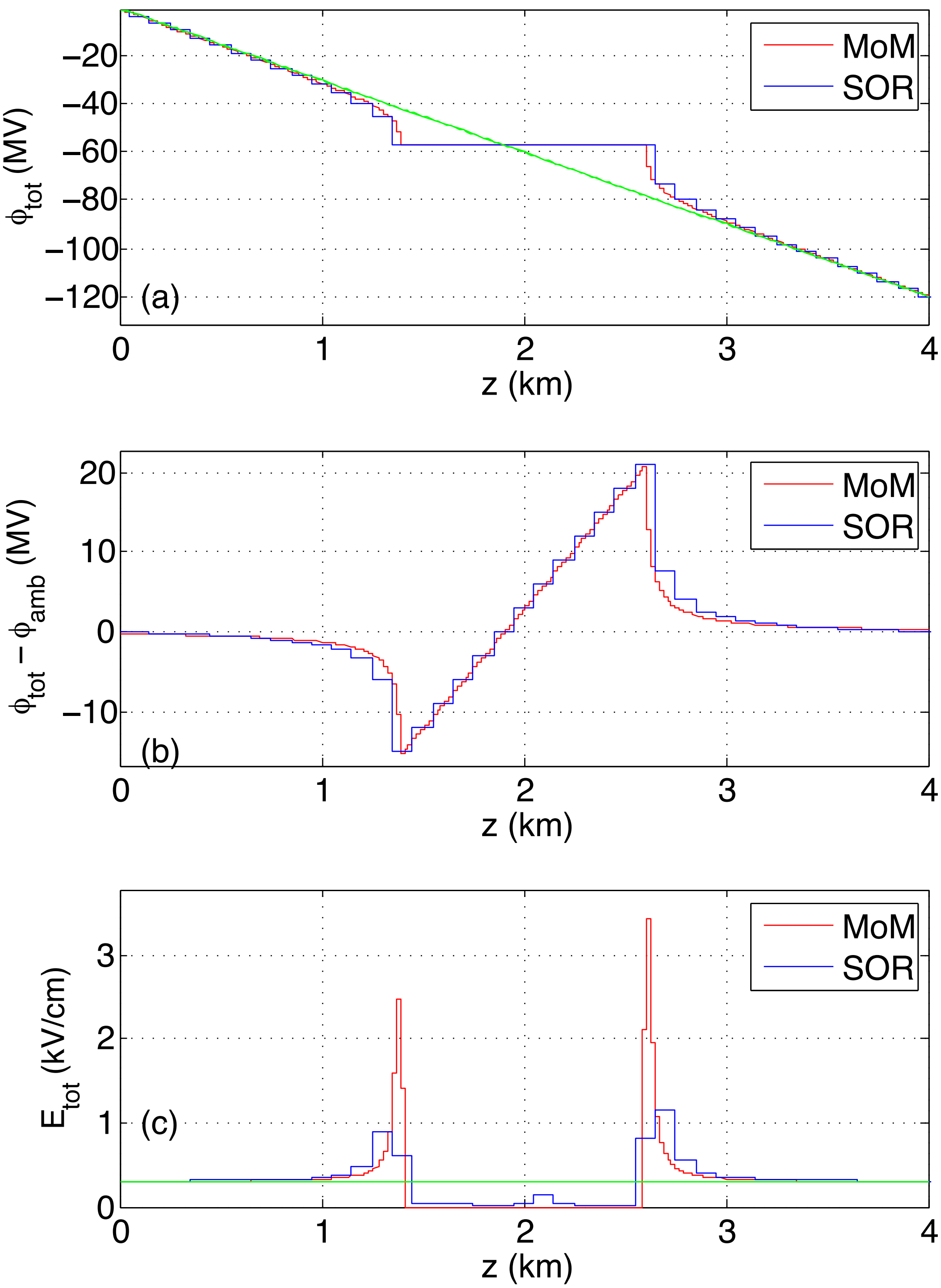

Figure 4.14. Comparison of results from MoM code in fine resolution, 20 m in x-, y- and z-directions (red lines) and from SOR algorithm in coarse resolution, 100 m in x-, y- and z-directions (blue lines). All values are given for a branched conductor of geometry shown in Figure 3.3b. All graphs are plotted along the central vertical axis of the simulation domain. (a) Total potential, with ambient potential plotted in green for reference; (b) Potential of the wire (i.e., total potential minus ambient potential); (c) Total electric field, with ambient electric field plotted in green for reference.

of moments along the central vertical axis (Figure 4.14a), we note that whatever the resolution, the Nelder-Mead simplex method used to derive the potential in the method of moments model and the bisection method employed with the SOR algorithm still return the same value for the channel potential. We can also notice that under the aforementioned conditions, the SOR method slightly overestimates the actual values of the potential, especially close to the channel tip. The agreement between the electric field magnitudes as derived in the two situations is poor (Figure 4.14c). Even if it remains fairly good at some distance from the channel, it is quite poor inside of it and at the channel tips. In particular, it can be non-zero inside of an equipotential conductor. Moreover, while the SOR solution qualitatively reproduces the field enhancement around the tip, it is not able to quantitatively reach real values of this enhancement due to the low resolution employed.

4.2 Charge and Charge Density

In the previous section, we already introduced a charge derivation when we validated the optimization of the potential in the channel such that its net charge is equal to zero. In this section we further investigate charge considerations by comparing the numerical estimations obtained using a SOR-based and a MoM-based model. In particular, we have chosen to consider the charge distributions associated with conductors placed in the external electric field.

Placed in a non-zero electric field, a conducting channel becomes polarized. We now investigate the charge carried by the channel using the two geometries and the two resolutions described in Section 4.1 and represented in Figure 3.3. We still use the results of the method of moments as a reference to check the accuracy of the results obtained by the SOR algorithm.

We first consider a linear equipotential channel placed in a uniform electric field. This allows us to check the linear charge density as well as the magnitude of the charge carried by the positively (or negatively) polarized part of the channel. Figure 4.15 shows the linear charge density along the wire derived using a finite difference method as discussed in Chapter 3 (applied to the potential obtained by the SOR algorithm) and the linear charge density retrieved from the method of moments. Figure 4.15a is obtained using a coarse resolution (the resolution is 100 m in x-, y- and z-directions), while Figure 4.15b is obtained using a finer resolution (20 m in x-, y- and z-direction). The agreement is fairly good in both situations except around the tips of the channel.

For the reasons explained in Section 3.1, we know that the charge derived from SOR-based model is concentrated on the grid points occupied by the channel. It is also the case with the method of moments. However, to explain the discrepancy at the tips of the channel, we must consider how the linear charge density is derived in the SOR code. Using the same definition for ϕ, δx, δy, δz as previously, the volumetric charge density at a point M with coordinates (x, y, z), is derived as follows [e.g., *Potter*, 1973, p. 86]:

$$\begin{aligned}
&\rho(x,y,z) = -\varepsilon_0 \nabla^2 \phi(x,y,z) \\
\Rightarrow\ &\rho(x,y,z) = -\varepsilon_0 \times \\
&\left(\frac{\phi(x+\delta x,y,z) - 2\phi(x,y,z) + \phi(x-\delta x,y,z)}{\delta x^2} + \right. \\
&\frac{\phi(x,y+\delta y,z) - 2\phi(x,y,z) + \phi(x,y-\delta y,z)}{\delta y^2} + \\
&\left. \frac{\phi(x,y,z+\delta z) - 2\phi(x,y,z) + \phi(x,y,z-\delta z)}{\delta z^2} \right)
\end{aligned} \tag{4.12}$$

The wire is placed along z-axis, and we know that each point of the channel occupies the elementary volume $\delta^3 V = \delta x\, \delta y\, \delta z$. Moreover, we know from Chapter 3 that the charge density inside of the wire is present only on the grid points occupied by the wire. Therefore the channel cross-section can be expressed as $S = \delta x\, \delta y$. At this point, it must be noticed that the SOR and the MoM codes solve similar but not exactly identical problems. Indeed, the cross section of the channel in the SOR code is rectangular, while it is circular in the method of moments (see Appendix B). For the purpose of comparison, the channel radius in the method of moments has been chosen to be equal to $r_0 = \delta x/2 = \delta y/2$. For the SOR code, the linear charge density ρ^l_{cha} is calculated as:

$$\rho^l_{cha} = \rho_{cha}\, S \tag{4.13}$$

where ρ_{cha} is derived using equation (4.12). The aforementioned difference in geometry is partially responsible for the differences observed in Figure 4.15. It is important to note also that the linear charge density is a by-product of the SOR algorithm, and therefore includes some approximations (e.g., due to the use of a finite difference method as discussed for the derivation of electric field in a previous section), whereas it is the main output in the method of moments.

The total charge in the channel can be calculated by integrating the linear charge density over the length of the wire. From Figure 4.15, we check that the total charge is zero, consistent with the condition of neutrality of the channel. Of interest is the comparison of the positive Q^+ charge carried by the channel– referred to as transferred charge in Chapter 3. Due to the neutrality condition, the channel carries equal amount of negative charge Q^-. The positive charge carried by the channel has been derived using the two methods described in Section 3.2; the results are shown in Table 4.1.

For both a coarse and a fine resolution, the agreement between the two methods is within ∼33%. As expected, this agreement is improved with an improved resolution.

Finally, we compare the linear charge density derived on a coarse grid using the SOR algorithm and the same quantity derived in a finer resolution using the method of moments. This allows us to check the importance of the resolution for the derivation of the charge density of a linear channel placed in a uniform field.

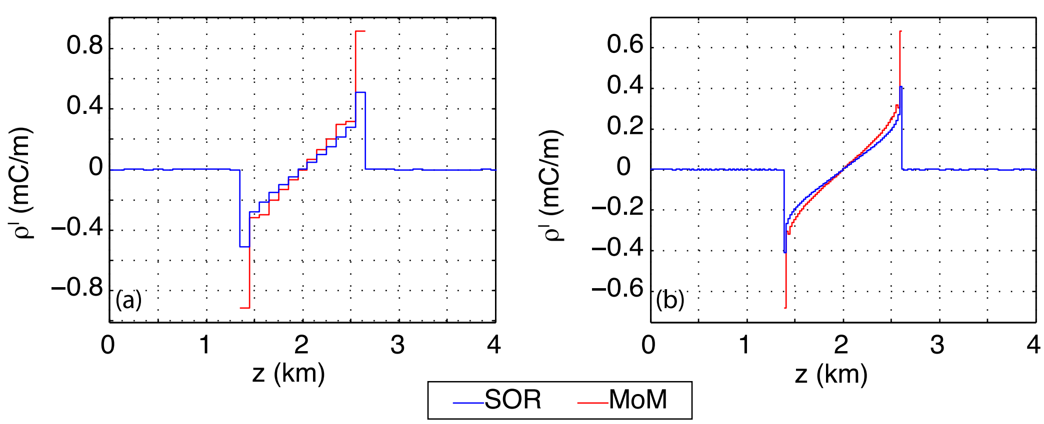

Figure 4.15. Comparison of linear charge densities obtained from MoM (red lines) and SOR (blue lines) based models for a space resolution of: (a) 100 m in x-, y- and z-directions; (b) 20 m in x-, y- and z-directions. All values are given for an unbranched conductor of geometry shown in Figure 3.3a. All graphs are plotted along the central vertical axis of the simulation domain.

Table 4.1. Positive charge (C) carried by an equipotential channel placed in a uniform ambient field.

Resolution (m)	Method MoM	SOR	Error[a]
	Unbranched Channel		
100	∼+0.195	∼+0.131	∼0.33
20	∼+0.096	∼+0.075	∼0.22
	Branched Channel		
100	∼+0.296	∼+0.180	∼0.39
20	∼+0.148	∼+0.106	∼0.28

[a] defined as $|Q^+_{\mathrm{SOR}} - Q^+_{\mathrm{MoM}}|/|Q^+_{\mathrm{MoM}}|$

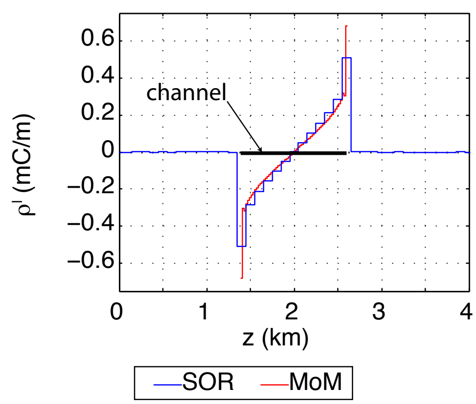

Figure 4.16. Comparison of linear charge density derived the MoM code in a fine resolution, 20 m in x-, y- and z-directions (red lines) and from a SOR algorithm in coarse resolution, 100 m in x-, y- and z-directions (blue lines). All values are given for an unbranched conductor placed on the central vertical axis of the simulation domain (see Figure 3.3a). All graphs are plotted along this axis.

The results are plotted in Figure 4.16. Except at the tips the agreement is very good.

The comparison of the linear charge density in the different sections of the branched channel described in Figure 3.3b would be quite tedious to represent in the manner of Figure 4.15 and would not provide significant information compared to the case of an unbranched channel. However, it may be useful to check how well the SOR algorithm is able to reproduce the positive charge carried by a branched channel as defined previously by equation (3.8). The results obtained using the two methods for two resolutions are reported in Table 4.1.

For a coarse resolution, the relative error between the two techniques is about $\sim$40% and it is expected that a more complicated geometry (by comparison with the unbranched channel) increases the error in the charge derivation. This result is similar to the results for the electric field magnitude and potential discussed previously. Nonetheless, when the resolution is improved, the error is reduced to less than $\sim$30%.

It can be surprising to see that the total obtained charge in the channel using the same method but in two different resolutions varies. An explanation lies in the fact that the geometries of conductors at two resolutions are not exactly the same. First, there is the error induced by the numerical length of the wire which makes a channel of fixed length and radius to occupy a smaller volume when the resolution is improved. Then we should recall that the radius r_0 of the channel in each case of MoM solutions has been fixed to $r_0 = \delta x/2 = \delta y/2$. Therefore, the channel has a smaller numerical length and a smaller radius for a finer resolution. These differences explain why we do not observe exactly the same charge values for the two resolutions considered.

4.3 Comparison with Previously Published Fractal Model

In this section, we check the ability of our model to reproduce a known fractal pattern established by an existing model. We chose to reproduce one of the blue jets modeled previously by *Pasko and George* [2002].

Blue jets and blue starters are believed to be positive streamer coronas expanding form the streamer zones of conventional lightning leaders under conditions when large-scale electric fields near the thundercloud tops exceed the minimum field required for the propagation of positive streamers in air [*Pasko and George*, 2002]. Due to the far greater resistivity of streamer channels compared to leader channels, the voltage drop along a streamer channel cannot be neglected as for leader structures, and consequently equipotentiality cannot be assumed (see discussion in Section 2.2). Therefore, the model developed in this thesis is modified to account for a finite potential drop along links following algorithms described in [*Pasko* *and George*, 2002]. We use exactly the same geometry and input parameters as described in [*Pasko and George*, 2002] to obtain results shown in their Figure 4b. The initiation point is set at the center of simulation domain at an altitude at which the propagation threshold for positive streamers is exceeded. Thus, an assumption is made that the initiation is somehow started at this location and that the blue jet further propagates from this point. The electric field thresholds required for propagation of positive and negative streamers are significantly higher than those for propagation of positive or negative leaders and therefore the propagation thresholds in the model have been adequately modified to use E_{cr}^{+}=4.4 kV/cm and E_{cr}^{-}=−12.5 kV/cm (see Table 2.3).

Whereas it was derived to ensure overall neutrality and equipotentiality of a leader channel in Chapter 3, the channel potential is now calculated to account for its resistivity. This is modeled using a voltage drop. *Pasko and George* [2002] assumed it to be equal to the propagation thresholds of the streamers of the corresponding polarity–i.e., the voltage drop is 4.4 kV/cm in positive streamers and −12.5 kV/cm in negative ones at ground pressure, and is scaled proportionally to atmospheric neutral density at higher altitudes. Starting from the initiation point, one and only one link is added to the channel at each step. The major difference is that the potential at the end of the newly created link is defined once and for the remainder of the simulation as $\phi^{end} = \phi^{start} - E_{cr}^{\pm}\, l$. While for equipotential leaders the potential of every point in the channel was updated after each link addition to ensure overall neutrality of the discharge tree, in the present case it does not vary for the remainder of the simulation. Therefore the assumption of the neutrality is not made for results presented in this section.

We run the simulation in a 80 km × 80 km × 40 km Cartesian domain discretized using 161×161×81 grid points. Therefore the discretization step (i.e., the resolution) is 500 m in x-, y- and z-directions. For the case of our study [*Pasko and George*, 2002, Figure 4b], the ambient electric field is created by a Q=120 C charge placed at x_Q=y_Q=40 km, i.e., in the center of the simulation domain at altitude z_Q=15 km. The source charge is assumed to have a Gaussian spatial distribution with a characteristic spatial scale equal to a_x=a_y=a_z=3 km in all three directions. Thus the ambient charge density ρ_{amb} (as defined in Chapter 3,

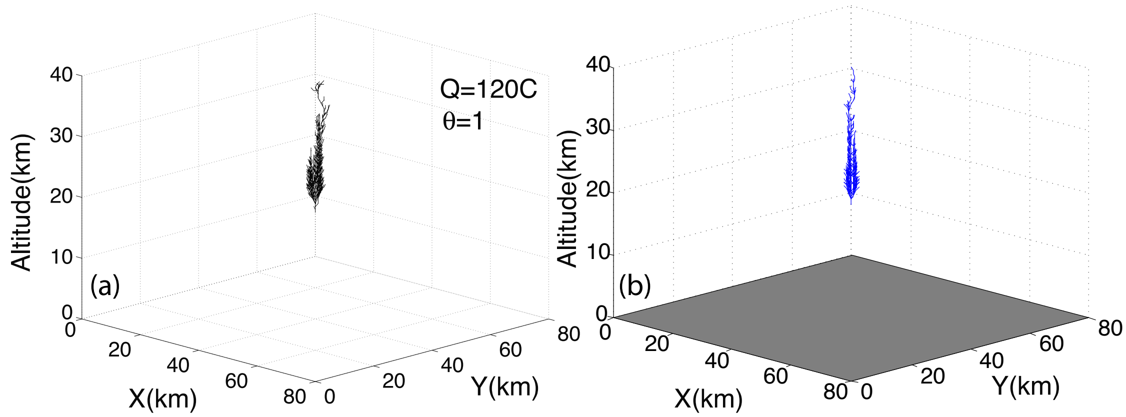

Figure 4.17. A blue jet discharge for a thundercloud with charge value Q=120 C having Gaussian spatial distribution with characteristic spatial scale 3 km and positioned at 15 km altitude: (a) taken from [*Pasko and George*, 2002]; (b) produced by the current model.

see also Appendix A) can be expressed as:

$$\rho_{cha}(x,y,z) = \frac{Q}{\pi^{3/2}a_x a_y a_z} e^{-\left(\left(\frac{x-x_Q}{a_x}\right)^2+\left(\frac{y-y_Q}{a_y}\right)^2+\left(\frac{z-z_Q}{a_z}\right)^2\right)} \tag{4.14}$$

The ambient electric field induced by such a charge distribution exceeds the positive streamer propagation threshold around altitude $z = 18$ km [*Pasko and George*, 2002, Figure 1a]. Therefore the initiation point has been fixed at the center of the simulation domain (x=y=40 km) at z=18 km.

The comparison of results presented in Figures 4.17a and 4.17b shows very similar inverted conical pattern of the discharge trees with similar radial and vertical spatial dimensions. The agreement between the two results is excellent. Therefore we conclude that the fractal algorithm implemented in our model is fully consistent with the one previously developed by *Pasko and George* [2002].

4.4 Feasibility of Use of the SOR Algorithm in Fractal Models

The results presented in Section 4.1 indicate that in order to improve the solution when applying a SOR algorithm in combination with a fractal model, we could think of using a finer resolution as we did for Figure 4.11. However, such a resolution would quickly become unbearable in terms of computational time when the method is practically used in a fractal model. Therefore, at this point, we can reasonably wonder if the SOR algorithm is a judicious choice for the derivation of the electric field and potential in a fractal model, due to the flaws observed in the estimation of the electric field. To answer this question, we must recall how the electric field and potential appear in the fractal model. They are introduced through the probability p_i for the propagation of a candidate link i (given by equation (3.3) and repeated here),

$$p_i = \frac{|E_i - E_{th}^{\pm}|^{\eta}}{\sum_i |E_i - E_{th}^{\pm}|^{\eta}}$$

where η and $E_{th}^{\pm}$ have been defined in Chapter 3. The field E_i in this equation is not the electric field derived using a finite difference method that is used in Figures 4.3, 4.4c, 4.5c, 4.6b, 4.7b, 4.9, 4.10c, 4.11c, 4.12b and 4.13b. The field E_i is calculated on the basis of a potential difference between the beginning of the link and its end, i.e., $E_i = (\phi^{start} - \phi^{end})/l$, where ϕ^{start} and ϕ^{end} are the total potentials at the tips of the candidate link, and l is the length of the link as was already defined in Chapter 3. This is important since we have shown in this chapter that the accuracy of the derivation of the electric potential of both an unbranched and a branched wire was indeed fairly good, with a relative error compared to actual values $\lesssim 10\%$.

We further notice that the origin of the links belongs to the channel where the potential has been shown to be known exactly (see, for example, Figures 4.8a and 4.14a), and that the end of the link is situated at a neighboring grid point, at some distance from the tip, where an error in potential never exceeds 10%. We can therefore conclude that the value E_i used in equation (3.3) is accurate to less than 10% and that the SOR method still stands as an efficient way to derive electric potential in a fractal model.

Additionally, we note that the discharge is started in the fractal model when the magnitude of the electric field exceeds the initiation threshold somewhere in the simulation domain. In this case, the magnitude of the electric field due to the cloud charges prior the discharge is actually derived using a finite difference method through equation (4.9). Results presented in Figure 4.2 have demonstrated that the method is accurate.

Thus the SOR algorithm, as used in our fractal model, has been checked to accurately reproduce the potential at any point of the simulation domain and at any stage of the simulation. It has also been shown that it efficiently reproduces the electric field magnitude due to cloud charges prior the discharge.

To summarize the presentation of material in this chapter, we note that we first validated the ability of our model to accurately reproduce the electric potential and field created by a uniformly charged sphere in free space placed above a perfectly conducting plane by comparing it with the exact analytical solution of the problem. We further demonstrated the ability of the model to reproduce the electric field and potential created by both an unbranched and a branched channel in a uniform ambient field using grids of different resolutions. We further checked the charge estimations for the above situations, and finally validated the fractal algorithm in our new model by modeling a blue jet event reported previously in [*Pasko and George*, 2002].

The validation of the model for simple cases of study allows us to apply it for modeling of lightning discharges, and related results are presented in Chapter 5, which follows.

Chapter 5

Modeling of Intracloud Lightning Discharge in a New Mexico Thunderstorm and Comparison with Lightning Mapping Observations

5.1 Simulation Results

In this section, we report results from a simulation run corresponding to an intracloud discharge. The results have been obtained in a 12 km $\times$ 12 km $\times$ 12 km simulation domain, which has been discretized using 41$\times$41$\times$61 equidistant grid-points. Hence, the space resolution is 300 m in the x- and y-directions and 200 m in the vertical z-direction. The algorithm used in this chapter is the one described in Section 3.1. We note that the ground level for lightning simulations is different from the reference altitude for the Lightning Mapping Array measurements (which is usually within 10 m of the mean sea level [*Rison et al.*, 1999]). As discussed in Chapter 3, our model uses ground level as zero altitude (z=0 km) reference point. To ease direct comparison with LMA results, all plot results produced by our model have been shifted by adding z_{gnd} to z such that all altitudes in Figures 5.1, 5.2, 5.4, 5.5, and 5.6 are given with reference at the sea level. After $\sim$32.5 seconds of application of charging currents I_1 and I_2 with magnitudes defined in Section 3.1, the conditions for lightning initiation are fulfilled (i.e., the electric field at one of the points inside of the simulation domain exceeds E_{init} threshold by 10%). This leads to cloud charge density ρ_{amb} in the two upper charge layers on the order of ± 1 nC/m^3. These values are smaller than those inferred from measurements by *Williams et al.* [1985] or *Coleman et al.* [2003], but still of the same order of magnitude. The positions, dimensions and integral charge values corresponding to each charge layer at this moment of time are summarized in Table 3.1, which is repeated below as Table 5.1.

Table 5.1. Charge values, heights and extents for the cylindrical disk model [*Riousset et al.*, 2006a].

Charge Layer	Altitude (km AGL[a])	Depth (km)	Radius (km)	Charge (C)
P	6.75	1.5	4.0	48.7
N	3.75	1.5	3.0	-51.6
LP	2.00	1.5	1.5	2.92

[a]AGL, above ground level

Figure 5.1 (which is also identical to Figure 3.1 from Section 3.1) shows a cross-sectional view of the model thundercloud (in the x-z plane positioned in the center of the simulation domain at y=6 km). The upper and lower positive charge layers are represented using red lines, while the central negative charge layer is represented using blue lines. In addition, Figure 5.1 also illustrates the electric field lines produced by this charge configuration just before the initiation of the discharge. The electric field lines converge toward the negative charge center and diverge from the upper positive one, consistent with expectations. Besides, the field is normal to the equipotential ground surface, also consistent with field theory.

Figure 5.2 shows an example of a fully developed discharge. The discharges trees are projected on the x-y, y-z and x-z planes (shown, respectively in panels (b), (d) and (e) of Figure 5.2). The panel (c) in Figure 5.2 shows a histogram representing the numbers of grid-points occupied by the discharge links as a function of the altitude. Finally, the altitude of each new link at each step is plotted in the upper panel (i.e., panel (a) of Figure 5.2). The sequence of steps in our model can be considered as resembling the time development of lightning flashes in the actual

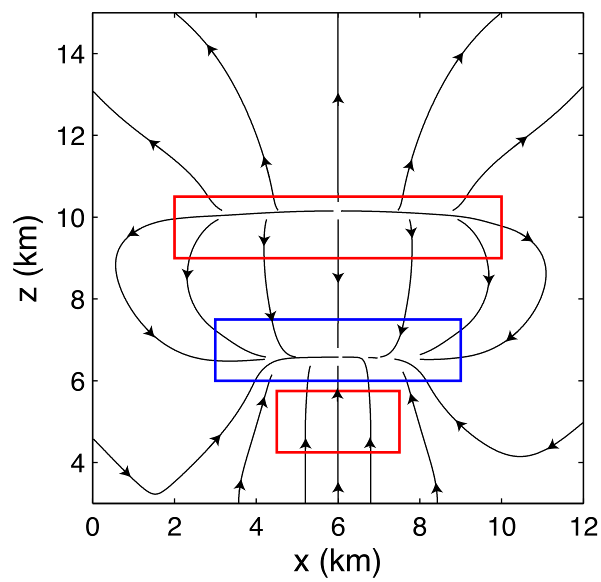

Figure 5.1. A cross-sectional view in the x-z plane at y=6 km of the model thundercloud with upper positive (P), central negative (N) and lower positive (LP) charge layers. Electric field lines produced by the model cloud are also shown for reference [*Riousset et al.*, 2006a].

LMA measurements. The step number gives the sequence of creation of new links in the model, and a color-scale similar to actual LMA data is used: early links are plotted in dark blue, latest ones in dark red, the color range in-between gives the sequence of events. For this run, ground level has been set at 3 km above sea level (the approximate altitude of the ground for measurements of the lightning activity near Langmuir Laboratory in central New Mexico). The simulated discharge is initiated at an altitude of 7.6 km above sea level (4.6 km above ground level), $\sim$1.5 km away from the central vertical axis of the simulation domain. It initially extends vertically without showing much of branching structure between $\sim$7.0 and $\sim$9.2 km before spreading horizontally in the volume of the main negative and upper positive charge layers (at altitudes around 6.5 and 10 km, respectively).

Figure 5.3 represents an actual intracloud lightning measured by the LMA over Langmuir Laboratory on July 31, 1999 at 22:23 (local time). This event is similar to the bilevel discharge first reported by *Rison et al.* [1999]. We observe the inception point of the discharge at an altitude of $\sim$8.0 km at northwestern edge of the storm. The discharge then propagates vertically between altitudes around 7.0

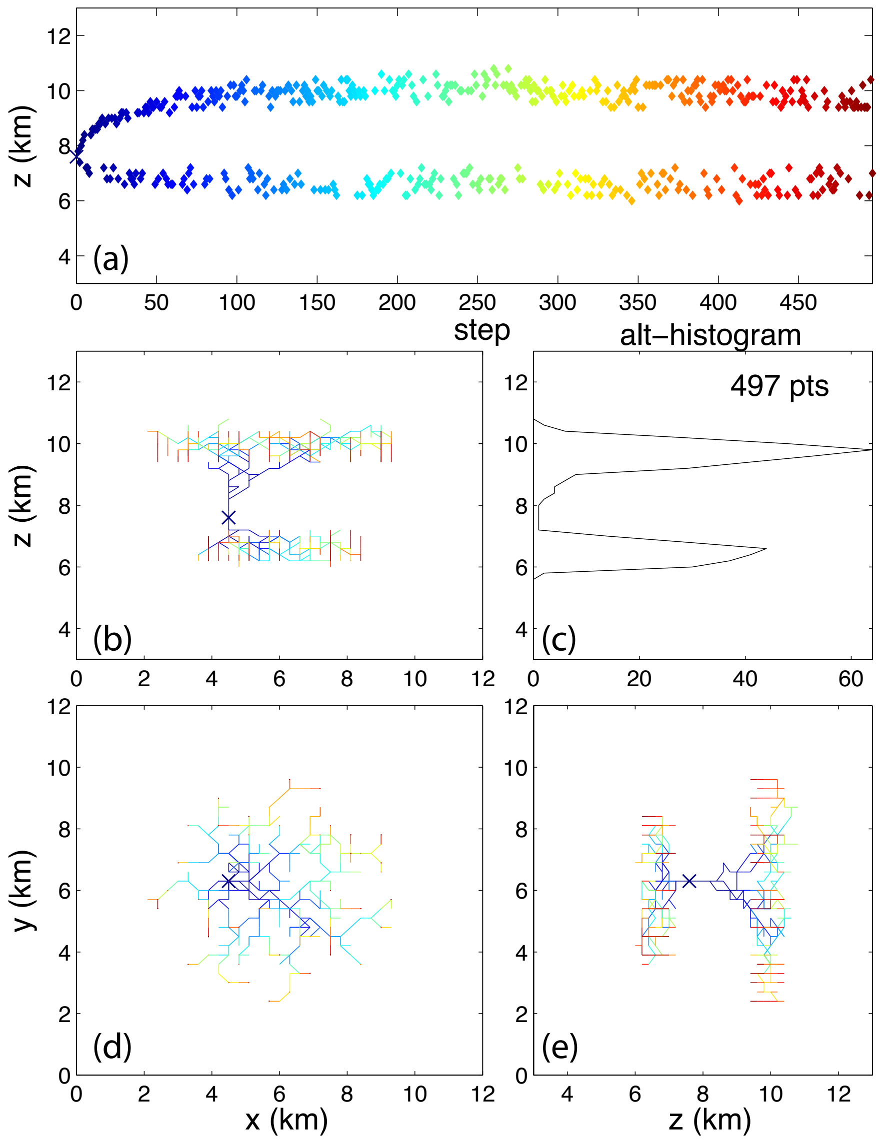

Figure 5.2. Representation in Lightning Mapping Array (LMA) data form of a simulated intracloud discharge. We use the same formatting as for the LMA data shown in Figure 5.3 [*Riousset et al.*, 2006a].

and 9.0 km, where horizontal propagation then becomes dominant.

Figure 5.4 is the same as Figure 5.2, except that only the branches developing above the initiation point are shown. In addition, we show the contours of the charge centers in panels (b), (d) and (e) by gray lines. The upper positive, central negative and lower positive charge centers are shown in panels (b) and (e), while

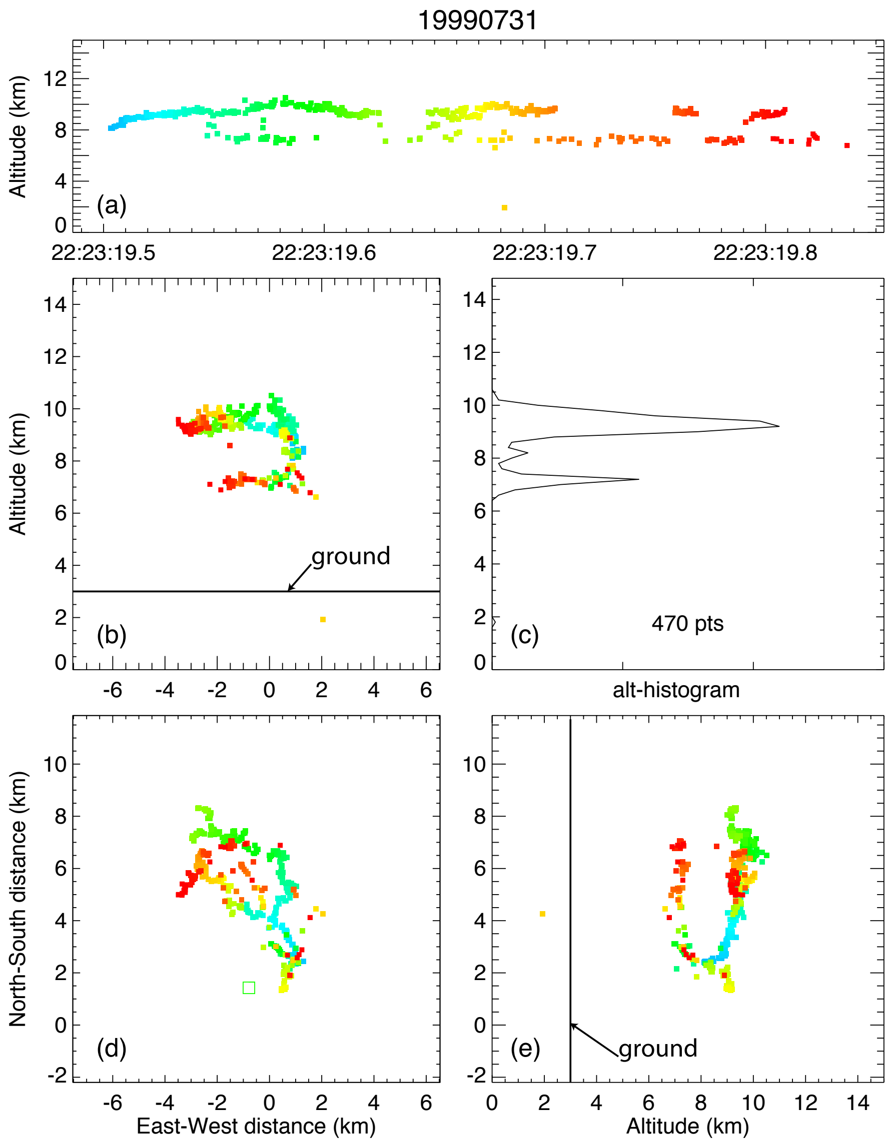

Figure 5.3. An actual bilevel intracloud flash measured by the LMA during the thunderstorm on July 31, 1999 at 22:23 (local time) [*Riousset et al.*, 2006a].

only the upper positive charge layer is illustrated in panel (d). Inspection of this figure indicates that the negative leaders are essentially contained in the upper positive charge layer. Figure 5.5 is the same as Figure 5.2, except that now only the branches developing below the initiation point are shown. Similarly to Figure 5.4, we plotted the contours of the upper positive, central negative and lower positive charge centers in panels (b) and (e), and those of the central negative layer in

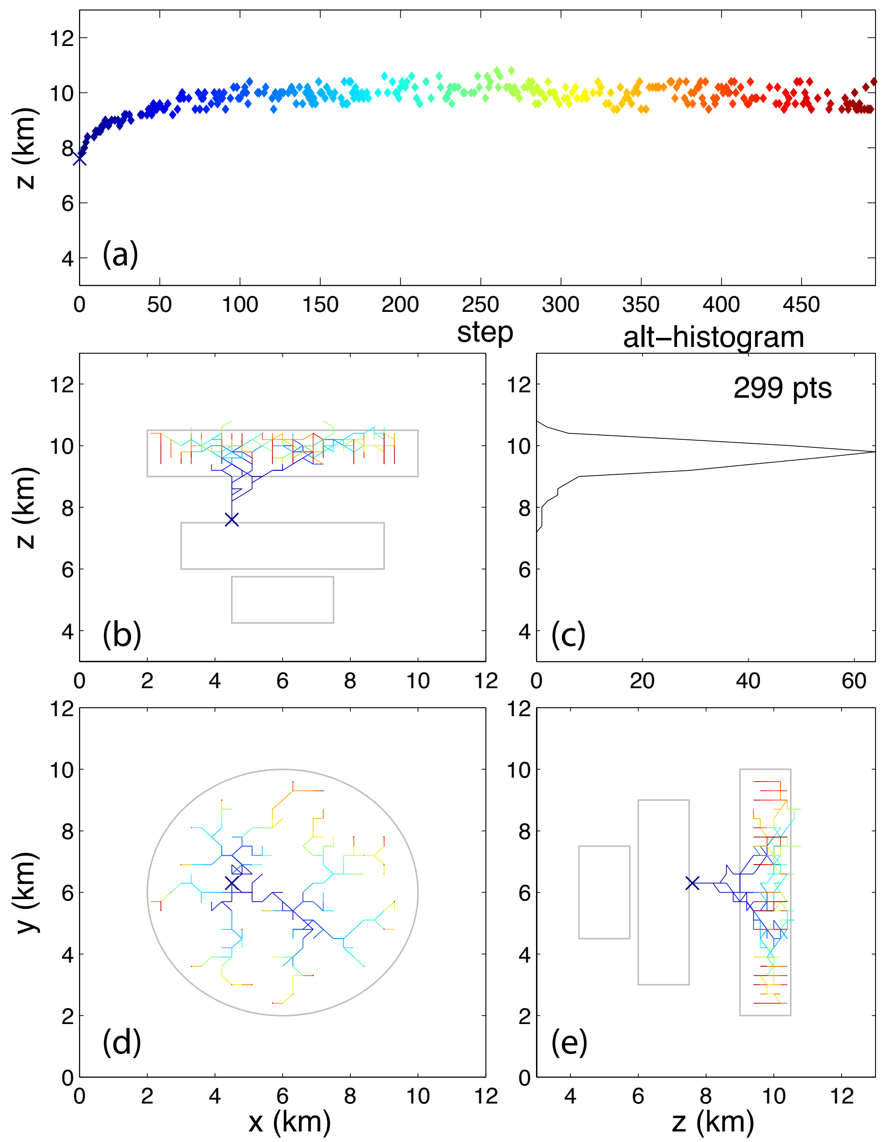

Figure 5.4. Representation in Lightning Mapping Array (LMA) data form of the upper branches of the simulated intracloud discharge reproduced in Figure 5.2. The gray lines represent the contours of the charge centers (see text for details) [*Riousset et al.*, 2006a].

panel (d). It can be noticed from this figure that positive leaders are mainly "trapped" in the central negative charge layer.

Figure 5.6a shows the same model discharge as shown in Figure 5.2 using a 3-D representation, while Figures 5.6b and 5.6c compare the total electric field (red lines in Figure 5.6b) and potential (blue lines in Figure 5.6c) before (solid lines)

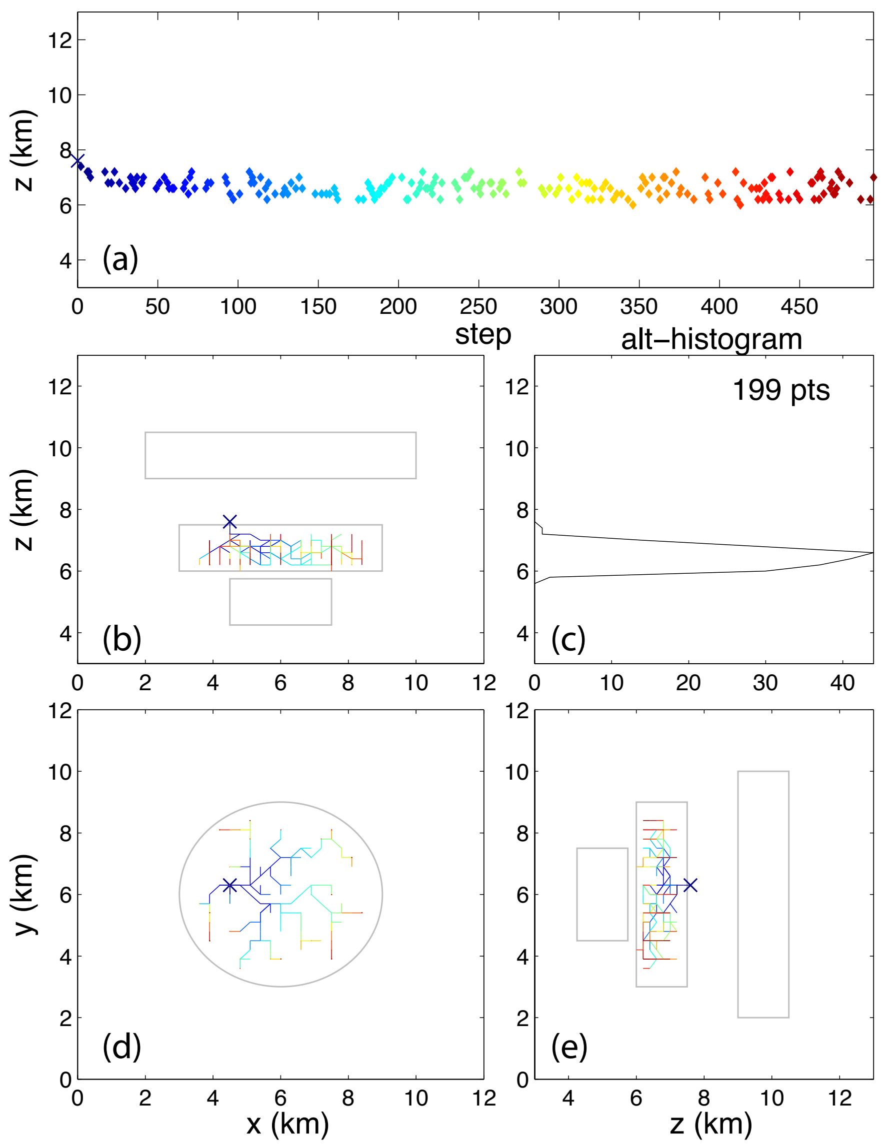

Figure 5.5. Representation in Lightning Mapping Array (LMA) data form of the lower branches of the simulated intracloud discharge reproduced in Figure 5.2. The gray lines represent the contours of the charge centers (see text for details) [*Riousset et al.*, 2006a].

and after (dashed lines) the flash at the center of the simulation domain, along the vertical axis. The propagation threshold given by equation (3.2) is also shown for reference by dash-dotted green lines in Figure 5.6b. A positive value of the electric field indicates an upward directed field.

Figure 5.7a shows the evolution of the discharge tree total potential ϕ_0. The

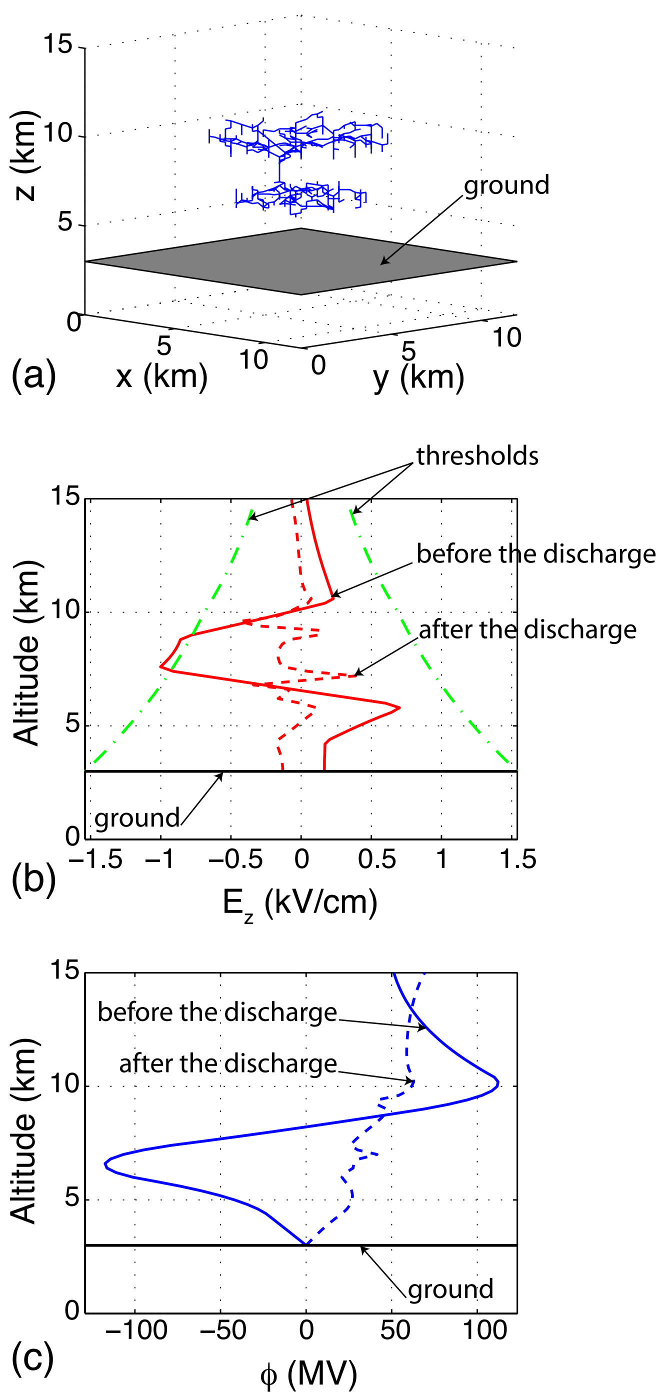

Figure 5.6. (a) 3-D view of the intracloud discharge shown in Figure 5.2 after 496 steps; (b) Electric field before the flash (solid red line), and after (dashed red line). The electric field initiation threshold is shown for reference by green dash-dotted lines; (c) Electric potential before (solid blue line), and after (dashed blue line) the discharge development [*Riousset et al.*, 2006a].

charge carried by the positive leaders is illustrated in Figure 5.7b. We note that negative leaders carry equal amount of negative charge, and the charge shown in Figure 5.7b can be interpreted as the total charge transferred by the discharge. Figures 5.7c and 5.7d illustrate the evolution of the discharge dipole moment as the simulation progresses. Figure 5.7a shows a rapid increase of the channel potential at the early stages of the discharge development, following by a smoother increase after which ϕ_0 reaches the final value of ∼41.5 MV. Figure 5.7b shows a progressive growth of the charge transferred by the discharge which reaches value ∼37.5 C by the end of the simulation. The magnitude of the dipole moment $\vec{p}$ shown in Figure 5.7c also smoothly increases reaching ∼122 C·km. Figure 5.7c shows that $\vec{p}$ is predominantly vertical and directed toward the ground. This trend is consistent with the development of the trees, since the horizontal components of $\vec{p}$ (i.e., p_x and p_y) become more and more negligible compared to the vertical component p_z.

A comparison of the total charge in the system before and after the development of the discharge trees allows us to check the charge conservation. The system remains approximately neutral, with differences between absolute values of positive and negative charges not exceeding ∼30 mC during different stages of the model execution. This difference is mainly due to numerical noise and is negligible compared to the charge in the cloud or in the upper and lower channel structures. As already noted above, the amount of charge carried by the positive and negative leaders is ∼37.5 C, which constitutes ∼75% of thundercloud charges of each polarity (i.e., 51.6 C) as shown in Table 5.1.

5.2 Discussion

The simulation run described in the previous section is typical for intracloud discharges produced by our model. As will be discussed in this section, it shows many similarities with the bi-level discharge observed during the thunderstorm over Langmuir Laboratory on July 31, 1999, which is reproduced in Figure 5.3. These measurements show the initial 2–3 km vertical propagation followed by two distinct regions of roughly horizontal propagation at altitudes of ∼6.5 and ∼9.5 km. The upper region corresponds to the propagation of the negative leaders in the thundercloud positive charge, and the lower one to that of the positive leaders in

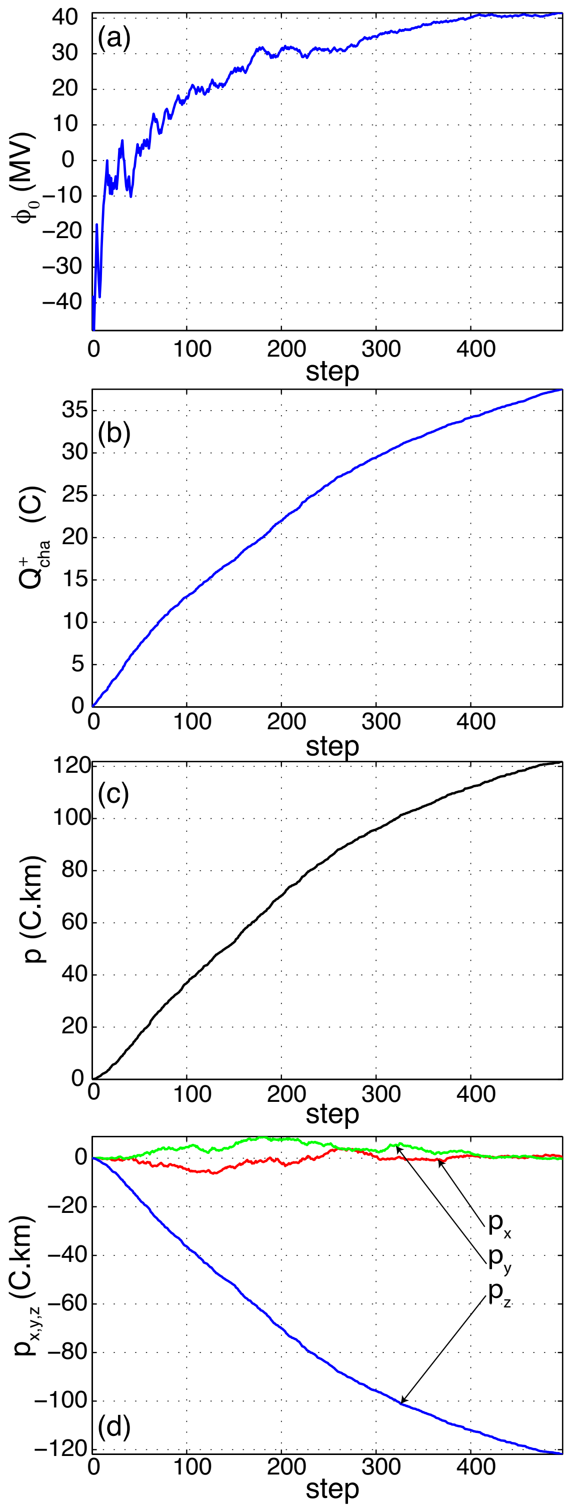

Figure 5.7. Parameters of the simulated discharge shown in Figure 5.2 at each step of the development: (a) Channel potential ϕ_0; (b) Charge carried by the positive leaders Q^+_{cha}; (c) Magnitude of the discharge electric dipole moment $p = |\vec{p}|$; (d) x-, y- and z-components (red, green and blue lines, respectively) of the dipole moment $\vec{p}$ [*Riousset et al.*, 2006a].

the main negative charge. These altitudes of propagation are in reasonable agreement with the results of our model shown in Figure 5.2. The model propagation altitudes are mostly defined by chosen positions of model thundercloud charges, and these positions, in fact, can be inferred directly from comparisons of model results with observations shown in Figure 5.3 [*Coleman et al.*, 2003].

Comparison of Figures 5.2 and 5.3 shows that both the simulated and measured discharges are not initiated on the axis of the inferred storm charges, although they both propagate in a rather symmetric manner toward and in the upper positive and central negative charge layers. It is recalled that x-, and y-directions in our simulation are arbitrary and do not necessarily correspond to East-West and North-South directions in Figure 5.3. Thus, no conclusions should be drawn from the horizontal position of the initiation point, it should merely be noticed instead, that our initiation algorithm produced realistic horizontal displacement of the initiation point with respect to the axis of the storm charge layers. The random initiation algorithm employed in the simulation uses the fact that the lightning is probably not initiated immediately upon the threshold being exceeded at some point in the cloud, but after the threshold is over-exceeded over some larger horizontal area. Initiating the discharge once the threshold is exceeded by 10% somewhere in the simulation domain allows the growing charges Q_{LP}, Q_N and Q_P to create such a region around the central vertical axis. The lightning is then initiated randomly within this area of high electric field (exceeding the initiation threshold E_{init}).

The initiation point should be regarded first and foremost as an indicator for locations of strongest vertical fields. In realistic situations the initiation point is also expected to depend on the non-uniformity of the actual storm charges. It is very improbable that the real thundercloud has the perfect cylindrical symmetry assumed by the model. Therefore, a non-uniform charge distribution is considered as a primary factor which would lead to the initiation of lightning closer to the edge of the cloud as in the case of Figure 5.3.

Tests have also been conducted with non-random initiation (the related results are not shown in this thesis for the sake of brevity). In this case, the discharge was always initiated at the point of maximum electric field magnitude. Due to the cylindrical geometry of the modeled thundercloud, this point was always on the main axis of the inferred charge layers at an altitude of 7.6 km. The same initial

2–3 km vertical extension of the tree followed by the horizontal propagations at altitudes around 6.5 and 10.0 km was observed. The main difference was that the discharge had taken a more symmetric form since the horizontal shift of the initiation point was suppressed. Quantitatively, the values for the channel potential, transferred charge, linear charge density and dipole moments remained very close to those discussed for the simulation presented in Figures 5.2 and 5.6 with parameters shown in Figure 5.7.

When the contours outlining the positions of the charge layers are superimposed with the discharge channels, as in Figures 5.4 and 5.5, it becomes obvious that simulated trees tend to propagate more or less through the full extent of the parent storm charges. A similar effect has been observed for dielectric breakdown in polymethylmethacrylate [*Williams et al.*, 1985]. This property has also been suggested for real intracloud discharges [e.g., *Shao and Krehbiel*, 1996; *Coleman et al.*, 2003]. When approaching or entering a region of intense charge density (either positive or negative) the potential gradient (i.e., the electric field) at the tips of the developing discharge trees becomes strongest in the horizontal direction. Since the discharge path is mainly driven by the direction of the local electrostatic field, both in real [*Williams et al.*, 1985] and simulated clouds, it is expected that the upper and lower ends of the discharge tree would propagate horizontally inside of the charge layers, where electric field is almost horizontal as illustrated in Figure 5.1.

A comparison of panels (a), (b) and (c) of Figures 5.2 and 5.3 reveals a far greater number of points for the propagation of the simulated positive leaders when compared to the actual measurements. *Rison et al.* [1999] noted that negative breakdown in positive charge regions is inherently noisier at radio frequencies than positive breakdown in a negative layer. The LMA primarily detects the negative breakdown in the positive charge region. In the negative charge regions LMA detects recoil streamers in which negative leaders re-ionize the channels formed by positive leader breakdown. Recoil processes are not accounted for in our model. The model thus simulates what the LMA detects due to negative leaders, but not positive leaders. Yet, comparison of Figures 5.4 and 5.5 reveals that positive trees developing in the lower portion of the discharge occupy less grid points that negative ones. This effect is purely numerical (i.e., is not related to physical differences between different types of leaders observed in LMA data) and results from the fact that the upper positive and central negative charge centers have different radii (4 and 3 km, respectively) but are discretized using grids with identical grid size. Thus to extend through the entire volume of each charge layer, the discharge should require $(\pi R_P^2 d_P)/(\pi R_N^2 d_N)$ times as many steps in the positive as in the negative charge region. Here, R_P, d_P designate, respectively, the radius and depth of the upper positive charge layer, while R_N, d_N refer to the same quantities for the central negative charge region. Using values tabulated in Table 5.1, we calculate this ratio to be ∼1.78, which is in good agreement with the ratio ∼1.51 derived from Figures 5.4c and 5.5c.

Comparison of Figures 5.2d and 5.3d emphasizes a major difference in the horizontal development in the simulated discharges as compared the measured ones, namely the horizontal structure of the simulated trees looks far more complex. As noticed previously, LMA measurements only detect recoil events associated with positive leaders. Since these occur later in the flash and do not occur in all the positive leaders, the LMA map of positive leaders has a different and simpler pattern than that of the simulation. Additionally, inspection of Figures 5.4d and 5.5d shows little difference between horizontal development of positive and negative trees. The present version of the model does not include any differences between positive and negative leaders, and their streamer zones in particular, and an extension of the model to account for related effects represents a subject of future studies. It is also likely that the details and complexities of the storm charge structure, which are not reproduced in our model, are largely responsible for the observed discharge structure shown in Figure 5.3.

The calculated value of the charge carried by the leader trees has been estimated at every step of the simulation and is plotted for positive branches in Figure 5.7b. The value at the end of the discharge development, ∼37.5 C is of particular interest and can be compared to the values cited in the available literature. *Helsdon et al.* [1992] quote typical values for the charge transferred ranging between 0.3 and 100 C. *Shao and Krehbiel* [1996] estimated charge transfer to be between 8.5 and 49 C for two intracloud discharges in Florida based on interferometer data and single-station electric field change measurements. *Rakov and Uman* [2003, p. 325] list the charge transfer values between 21 and 32 C for an intracloud discharge in a

New Mexico thunderstorm. Our model results are generally consistent with values documented in the existing literature.

The average linear charge density of discharge trees in our model can also be estimated and compared to previously published values. This is done by summing the absolute value of the charge carried by channels of each polarity and dividing it by the total length of the channels (~147 km), leading to an estimate ~0.5 mC/m. This value is below but still is in a reasonable agreement with a value of 1 mC/m referred to by *Helsdon et al.* [1992] and *Mazur and Ruhnke* [1998]. It is also in a good agreement with the linear charge densities between 0.7 and 8.7 mC/m measured by *Proctor* [1997] for intracloud flashes with origin similar to that of the simulated discharge presented in this chapter. We note that the accuracy of the derivation of the linear charge density can be questioned since it occupies such large volume (in the present example a grid-point covers volume $300 \times 300 \times 200$ m^3). However, based on the analogy with an inflating wire, we can argue that the method used in the model is not unreasonable. If we consider an equipotential wire of radius r_0 carrying a fixed linear charge density ρ^l, it is expected that the potential created by such a wire at some distance of the wire will be the same whatever the value of r_0 is, since we derive the potential as:

$$\phi(\vec{r}) = \phi_{amb}(\vec{r}) + \frac{1}{4\pi\varepsilon_0}\int_L \frac{\rho^l(\vec{r'})}{|\vec{r'} - \vec{r}|}d\vec{l'} \tag{5.1}$$

where $\vec{r}$ defines the coordinate vector of any point in space, $\phi_{amb}(\vec{r})$ is the ambient potential at this point, L is the total length of the wire, $\vec{r'}$ a coordinate vector pointing to a point in the wire, and $\rho^l(\vec{r'})$ and dl' are respectively the linear charge density and differential length element along the wire at the point designated by $\vec{r'}$. Therefore, r_0 can be increased without changing the value of the electric potential and field far enough from the channel. At some point r_0 can be such that the volume occupied by the channel is comparable to the volume of the grid point sequence used in our simulation to model it. From this point of view, we spread the charge carried by the channel in a larger volume, thus decreasing the volumetric charge density while keeping constant the linear charge density. Therefore, the derivation of the potential still remains correct at some distance from the channel. If ρ^l remains constant, the volumetric charge density would decrease in a coarse resolution, and our model would not be able to reproduce its variations correctly close to the channel. Nevertheless, the model can still provide a fairly good approximation for the linear charge density. No current computer could possibly be powerful enough to reach a resolution needed to accurately describe the realistic volumetric charge density in lightning leaders in models capturing large scale (∼km) electrical structure of thunderclouds, since the exact description of the charge distribution in and around the channel would require a resolution of ∼1 mm in all directions (the leader channel radius is estimated to be in the order of a few millimeters [e.g., *Gallimberti et al.*, 2002]).

Figure 5.7a shows the evolution of the channel potential during the development of the discharge trees. Being initiated just above the central negative layer, the initial channel potential ϕ_0 is strongly negative (−47.5 MV). In the early stages of the development (∼30 steps), ϕ_0 rapidly increases to positive values. Figure 5.2a shows that at this moment, the discharge enters the upper positive and central negative charge centers. These regions of intense charge correspond to "wells" of ambient potential at altitudes around 6.6 and 10 km (see Figure 5.6c). When the discharge reaches a well of potential (positive or negative), the well extends horizontally faster than it goes "uphill" (i.e., in the vertical direction). This results in a smoother increase in channel potential after ∼30 steps, and causes the discharge to start developing horizontally due to the large potential gradients in the horizontal direction (see Figure 5.1). A similar behavior was observed by *Behnke et al.* [2005] (see in particular Figures 5 and 6 of this paper), but their model was not able to simulate the discharge to completion. In particular, a reason for ϕ_0 to reach higher positive values on the order of 41.5 MV in our work lies in the ability of our model to model fully developed discharge trees.

The overall symmetry of the thunderstorm charge configuration in our model suggests that the related electric dipole moment is essentially vertical. The Q_P and Q_N charge layers form a dipole structure at the top of the cloud in which leaders of opposite polarities propagate. It is therefore expected that the fully developed channels would form an inverted dipole (i.e., vertical and preferentially downward directed). Results presented in Figure 5.7d are consistent with these expectations. Figure 5.7d also indicates that the dipole moment of the discharge is dominated by its vertical component during the full period of propagation of the leader channels.

The magnitude of the dipole moment of the fully developed discharge has been calculated to be ∼122 C·km, consistent with values previously reported in [*Shao and Krehbiel*, 1996].

Results of the present work demonstrate the ability of the model to produce realistic intracloud discharges. The model also allows direct investigation of the reduction of the electric field inside of the thundercloud due to the growth of the discharge trees. The results shown in Figure 5.6b demonstrate that the simulated intracloud leader structure significantly reduces the electric field in the cloud. In particular, the fractional decrease of the electric field by $\sim 80\%$ at an altitude around 8 km is in reasonable agreement with the value ∼60% measured by *Winn and Byerley* [1975]. This reduction is especially pronounced at altitudes ∼6.5 km and ∼10.0 km, where most of discharge trees develop (see Figure 5.6b). The field is lowered far below the propagation threshold. Our results therefore demonstrate that under model conditions discussed in Section 3.1 the bulk charge carried by the integral action of positive and negative lightning leaders is sufficient to significantly reduce the value of the electric field in the thundercloud.

5.3 Summary of Results

In this chapter, the model introduced in Section 3.1 has been successfully applied to reproduce a realistic pattern of an intracloud discharge (in particular, the altitude of initiation and extensive horizontal propagation of leader channels) comparable to an actual discharge observed over Langmuir Laboratory on July 31, 1999. It has been shown that parameters of the discharge such as the charge carried, dipole moment and average linear charge density associated with the leader trees, are in good agreement with related measurements reported in the existing referred literature. The model has been applied to study the reduction of the electric field in the thunderstorm due to the growth of the bipolar structure of leader trees resembling development of an intracloud lightning discharge. This study suggests that the polarization charges carried by the leader trees could lower the net charge in the different charge layers of the thundercloud and could decrease the total electric field significantly below the lightning initiation threshold.

Chapter 6

Summary and Suggestions for Future Research

6.1 Summary of Results

Here we summarize the principal results and contributions, which follow from studies presented in this thesis.

6.1.1 Development of a New Stochastic Model of Lightning

A new three-dimensional probabilistic model describing development of bi-directional structure of positive and negative lightning leaders closely resembling processes observed by LMA in association with intracloud discharges has been developed. The model represents a synthesis of the original dielectric breakdown model based on fractal approach proposed by *Niemeyer et al.* [1984] and the equipotential lightning channel hypothesis advanced by *Kasemir* [1960], and places special emphasis on obtaining self-consistent solutions preserving complete charge neutrality of the discharge trees at any stage of the simulation. This work also employed refined description of boundary conditions, by implementing open boundary conditions on the side and upper boundaries of the simulation domain. Results presented in Chapter 5 have evidenced the applicability of the model to the study of intracloud discharges. The model results are compared to a representative intracloud discharge measured by LMA in a New Mexico thunderstorm on

July 31, 1999. These comparisons indicate, in particular, that the model is capable of realistically reproducing principal features of the observed event including the initial vertical extension of the discharge between the main negative and upper positive charge regions of the thundercloud, followed by horizontal progression of negative and positive leaders in the upper positive and main negative charge regions, respectively.

6.1.2 Validation of the Newly Developed Fractal Model

We have performed a thorough validation of the model by checking independently each of the major model components. In particular, the derivation of the channel potential have been examined by comparison with solutions obtained with the method of moments for two simple cases: a linear and a branched equipotential wire placed in a uniform electric field. The fractal algorithm of the new model has been tested by comparisons with results of a similar model previously published in referred literature. The final validation of the model has been done by simulating an intracloud discharge and comparing the simulation output with an actual discharge pattern measured by the lightning mapping array on July 31, 1999 over Langmuir Laboratory, Socorro, NM as discussed in previous section. The altitude of the initiation of the lightning as well as the levels of horizontal propagation are in good agreement with observations. In addition, as summarized in Chapter 5, the values of the simulated charge transfer, leader linear charge density and electric dipole moment are also in a reasonable agreement with experimental measurements by various authors. In particular, for the model case presented in this thesis, the total charge transfer, the vertical dipole moment and the average linear charge density associated with the development of bi-directional structure of leader channels are estimated to be 37.5 C, 122 C·km, and 0.5 mC/m, respectively, in good agreement with related data reported in the referred literature.

6.1.3 Identification of a Mechanism of the Electric Field Reduction due to Intracloud Lightning

The propagation in the charge regions of the thundercloud of leader trees of opposite polarity results in a dramatic reduction of the net charges of both polarities in the thundercloud layers. Due to the polarization nature of the lightning charge, this effect neither violates the overall neutrality of the discharge channels, nor changes the total charge in the simulation domain. However, this reduction of charge involves a strong reduction of the electric field within the thunderstorm, consistent with observations and balloon measurements over New Mexico. The model results demonstrate that the bulk charge carried by the integral action of positive and negative leaders leads to a significant (up to 80%) reduction of the electric field values inside the thundercloud, significantly below the lightning initiation threshold. This effect has been quantified in this thesis and related results are in a reasonable agreement with experimental measurements by *Winn and Byerley* [1975].

6.2 Suggestions for Future Research

There is, as always, much more work to be completed. The greatest strength of the model developed in this thesis lies probably in its theoretical simplicity, and in the fact that it involves only a limited number of purely mathematical parameters. Every of the present parameters have been validated by reference to the work of other authors (providing distribution of the thunderstorm charge densities, lightning initiation and propagation electric field thresholds, etc.). Indeed, the only purely mathematical parameter in the model which has not been physically justified yet is the probability sensitivity η (in equation (3.3)). For this reason, the influence of this parameter on the simulation results should be established, and an attempt should be made to define this parameter in a physical framework similarly to what has been done for streamer discharges [*Popov*, 2002].

In this thesis only intracloud discharges have been investigated. The present model is directly applicable to studies of thundercloud conditions leading to cloud-to-ground discharges and related work represents an important task for future research.

Investigations on the relationships between lightning discharges and transient luminous events (TLEs, for details see [*Pasko*, 2006, and references therein]) are particularly relevant for the study of coupling of the lower and upper regions of the Earth's atmosphere, and the presented model can be of great use for this purpose.

In particular, the present model is believed to be especially useful for identifying specific conditions in thunderclouds leading to upward propagation of positive and negative leaders above the cloud tops, which are believed to serve as precursors and starting points of blue jets and gigantic jet TLE phenomena (about this issue, see [*Riousset et al.*, 2006b]).

In addition to the application of the current model to the aforementioned phenomena, improvements of the modeling can be considered. In particular, the modeling of the upper atmospheric boundary as a "moving capacitor plate" should be introduced to better account for ionospheric images of the thunderstorm charges [*Greifinger and Greifinger*, 1976; *Pasko et al.*, 1997; *Pasko and George*, 2002]. This model modification would be especially important for studies of blue jets and gigantic jets.

It was emphasized in Chapter 1 that most of fractal models based on work by *Niemeyer et al.* [1984] do not employ any time-scale of discharge development, neither does the model discussed in this work (Chapter 3). A possibility to describe realistic time development of the discharge should be investigated in further version of the model.

Finally, it has also been emphasized in Chapter 5 that the model simulates the propagation of positive and negative leaders in exactly same way. In reality, major differences exist between their propagation mechanisms. Those differences mainly lie in differences between streamer zones around positive and negative leader tips and have been discussed in Chapter 2. However, for the reasons discussed in Chapter 1, they have not yet been introduced in the model discussed in Chapter 3. The modeling of a streamer-to-leader transition and streamer zone effects are major issues in the current fractal models, that will need to be addressed in future studies.

Appendix A

Model Charge and Potential Sources

This appendix lists the various possible sources currently available in the model. They can be divided in two categories: charge distributions and potential distributions.

A.1 Charge Distributions

A uniformly charged sphere is an elementary geometry illustrated in Figure A.1a. It requires the definition of the coordinates (x_Q, y_Q, z_Q) of the center of the sphere, as well as its radius a and its charge Q. The charge density ρ_0 within the sphere is not derived as $\rho_0 = Q/\left(\frac{4}{3}\pi a^3\right)$, as could be expected. Instead, the model first counts the number of grid points n within the volume enclosed by the sphere, then multiplies it by $\delta^3 V$–the elementary volume occupied by one grid point–to obtain the volume occupied by the n grid points within the sphere. The charge density is finally derived as $\rho_0 = Q/(n\delta^3 V)$. This approach is necessary to ensure that the charge implemented is actually the one used by the model, and that the loss in errors due to discretization are negligible. For example, if a sphere is such that it is contained within a single grid point (i.e., $\frac{4}{3}\pi a^3 < \delta^3 V$), the "normal" derivation of charge density is expressed as $Q/\left(\frac{4}{3}\pi a^3\right)$. If this value is assigned to this grid point, the total charge in the system is $Q\,\delta^3 V/\left(\frac{4}{3}\pi a^3\right) > Q$. This would introduce an error that we have chosen to correct in the way described above.

The uniformly charged sphere placed above a perfectly conducting ground plane is used in Chapter 4 to verify the ability of the SOR algorithm to produce correct

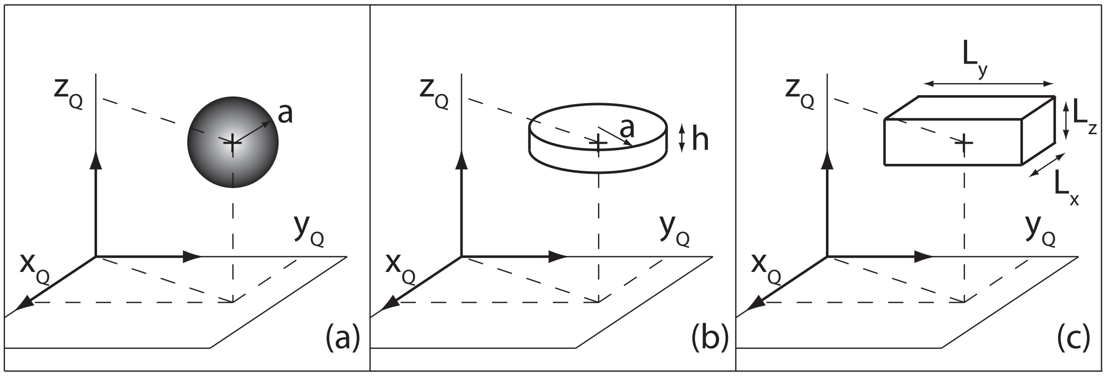

Figure A.1. Available geometries for the charge sources in the model: (a) sphere; (b) cylinder/disk; (c) block.

values for the potential and electric field.

The charge Q can also be distributed in a cylindrical geometry (Figure A.1b). In this case (x_Q, y_Q, z_Q) define the coordinates of the center of the cylinder, h its height (sometimes also referred to as its depth) and a its radius. Again the number of points n enclosed in the disk is first counted, then the charge density ρ_0 is derived as $\rho_0 = Q/(n\delta^3 V)$.

The uniformly charged disk is especially useful for the modeling of the tripolar structure of the thundercloud. Q can be either assigned or loaded using charging currents discussed in Section 3.1.

Although it has not been used for any of the tests presented in this thesis, it is possible to use a block of uniform charge density as a source of the model (Figure A.1c). In addition to the charge Q and the coordinates of the center of the block, the length l_x, width l_y and height l_z of the block need to be specified. The numerical discretization errors are eliminated in a way similar to what has been described for the spherical and cylindrical geometries.

To avoid the sharp boundaries of the sphere or the cylinder, a Gaussian charge distribution is introduced. The knowledge of the total charge Q, of the coordinates of the center of the charge distribution (x_Q, y_Q, z_Q) and of the characteristic spatial scales in x-,y- and z-directions (a_x, a_y and a_z, respectively) allows us to express the

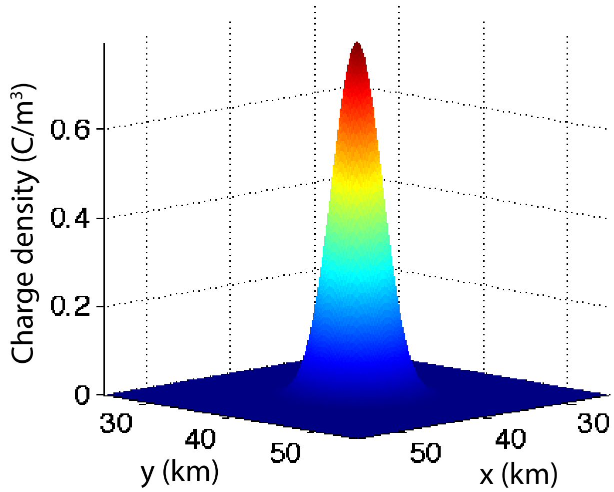

Figure A.2. Gaussian charge distribution in the plane z=15 km for the parameters used in Chapter 4 for blue jet simulation.

charge density ρ at any point $M(x,y,z)$ as:

$$\rho(x,y,z) = \frac{Q}{\pi^{3/2}a_x a_y a_z} e^{-\left(\left(\frac{x-x_Q}{a_x}\right)^2+\left(\frac{y-y_Q}{a_y}\right)^2+\left(\frac{z-z_Q}{a_z}\right)^2\right)}$$

This expression is the same as equation (4.14) in the thesis. As an example of a Gaussian distribution, we plot in Figure A.2 the charge density in the plane z=15 km for the charge used to simulate the blue jet in Chapter 4. The parameters used in this example are: $Q=40$ C, $x_Q=40$ km, $y_Q=40$ km, $z_Q=15$ km, and a_x=a_y=a_z=3 km.

Finally, it must be noted that any of the aforementioned distributions can be combined to describe very diverse charge configurations. Each charge distribution is derived independently from the others, and finally, the resulting charge configuration is obtained by summing the charge densities created by each distribution.

A.2 Potential Distributions

Instead of assuming a uniform charge density in the geometries described in panels (a), (b) and (c) of Figure A.1, we can fix the potential within the volume of the sphere, disk or block respectively. This provides different sources for the model. The main difference is that we no longer set up Q or ρ, but fix the potential ϕ within the volume and then run the SOR algorithm. In particular, we can use the disk or the block geometries to model a linear equipotential channel (in Chapter 4, we used for example h=1.2 km and a=$\delta x/2$=$\delta y/2$).

To model the branched geometry of Figure 3.3b, we first fixed the potential along a simple line as in Figure 3.3a and then fixed the potential at adequate points to obtain the desired geometry.

Generalizing this procedure, we can fix the value of the potential at any point of the simulation domain, and maintain its value throughout a simulation run. Then we can derive the resulting potential distribution anywhere else in the simulation domain. This is especially useful for derivation of the potential induced by complex geometries such as equipotential fractal discharge trees. In particular, this approach is used in the calculation of the potential ϕ_{cha} induced by the leader trees in the fractal model as explained in Chapter 3 and implemented in Chapter 5.

Appendix B

Limitations of SOR and MoM Solutions for Small Radius Wires

The use of SOR and MoM algorithms with small radii cylinders raises some issues that are briefly discussed in this appendix.

B.1 Limitations of the SOR Method

The use of a SOR algorithm requires a finite difference method (FDM) to discretize the simulation domain. To accurately reproduce streamer or leader channels of phenomena such as lightning, an extremely fine resolution would be required. A leader radius at ground level is, for example, estimated to be only a few millimeters [e.g., *Gallimberti et al.*, 2002]. To describe accurately this type of channel, a resolution of $\sim$1 mm in all directions would be required. At the same time, the best achievable spatial resolution with currently available computing resources for a simulation domain exceeding several thousands of cubic kilometers is several hundreds of meters. Therefore a compromise has to be made.

The links resembling the discharge channels in our model are plotted with an infinitely small diameter. A simulated discharge tree can actually be seen as a sequence of points, each of which occupies an elementary volume $\delta^3 V = \delta x\, \delta y\, \delta z$, where $\delta^3 V$ is a cubic elementary volume and δx, δy and δz, are spatial resolutions in x-, y- and z-directions, respectively (see Figure B.1a). Obviously, channel segments of real lightning leaders do not occupy such large volumes. That is why it is

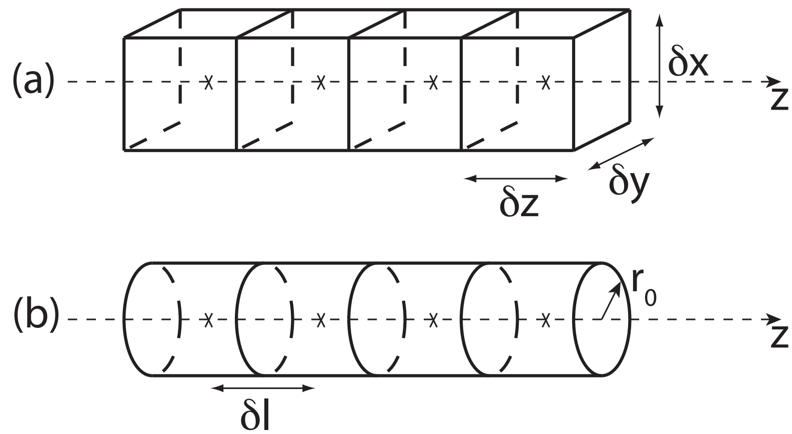

Figure B.1. Discretization of small radius cylinder by (a) a finite difference method; (b) the method of moments.

very important to check the influence of such an approximation on large scale distributions of the electric potential, field and charge density. This is done in Chapter 4.

B.2 Limitations of the Method of Moments

In the method of moments, the channel is considered as a cylinder of radius r_0 for the case of Figure 3.3a or as a sum of cylindrical elements for the case of Figure 3.3b. Each cylinder can be discretized using any number of elementary cylinders with radius r_0 and elementary length δl, defined as the ratio of the total length of the channel over the number of elements used to discretized it. However, a limitation appears for $r_0 \gg \delta l$. This limitation is well-known in MoM-based studies of moderately thick cylindrical antennas, and is usually referred to as the segment length-to-radius ratio condition [e.g., *Werner*, 1998].

To evidence it in the framework of the model validation discussed in Chapter 4, we consider the linear charge distribution along the body of a 1 meter long wire with fixed potential equal to 1 V. The wire is discretized using 100 elementary cylinders, i.e. δl=1 cm (see Figure B.1b). First the wire is assumed to have a 1 mm radius (case (a)), then it is assumed to have a 1 cm radius (case (b)).

Results for case (a) and (b) are given in Figures B.2a and B.2b, respectively. For a 1 mm radius wire, $r_0/\delta l$=0.1 $\ll$ 1, the charge density increases at the tip of

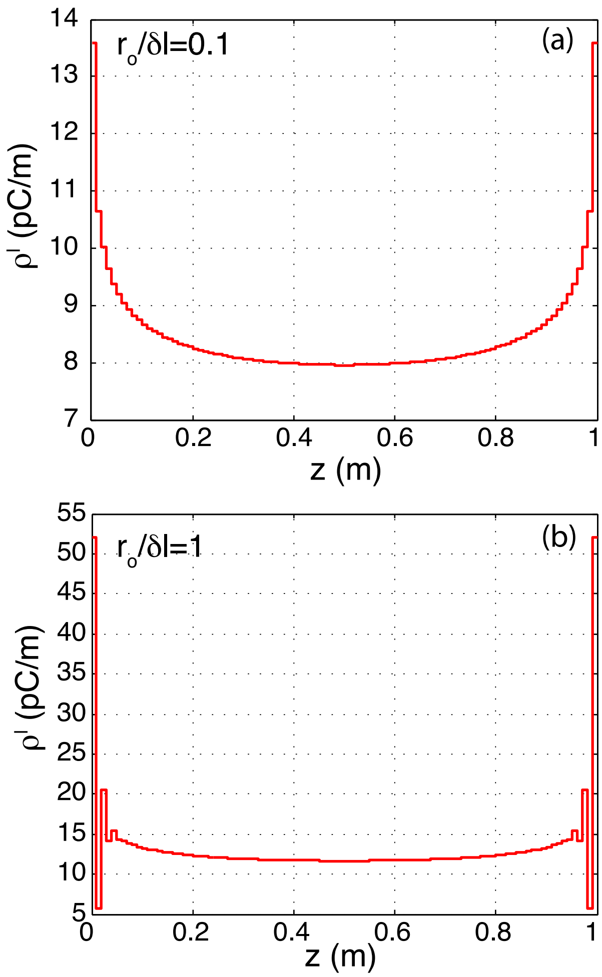

Figure B.2. Linear charge density created by a 1 m equipotential wire with potential equal to 1 V and radius r_0 equal to 1 mm (a); 1 cm (b) using the method of moments.

the channel. For a 1 cm radius wire, $r_0/\delta l$=1 $\geq$ 1, the charge density oscillates at the tips of the wire. This is obviously not a realistic behavior and therefore brings forward the existence of a limit value of the ratio $r_0/\delta l$.

Finally, it must be remembered that unlike the finite difference method which is limited to grid points of the discretized domain, the method of moments allows to derive the potential at any point in space as follows:

$$\phi(\vec{r}) = \phi_{amb}(\vec{r}) + \frac{1}{4\pi\varepsilon_0}\int_L \frac{\rho^l(\vec{r'})}{|\vec{r'} - \vec{r}|} d\vec{l'} \tag{B.1}$$

where $\vec{r}$ defines the coordinate vector of any point in space, $\phi_{amb}(\vec{r})$ is the ambient potential at this point, L is the total length of the wire, $\vec{r'}$ a coordinate vector pointing to a point in the wire, and $\rho^l(\vec{r'})$ and dl' are respectively the linear charge density and differential length element along the wire at the point designated by $\vec{r'}$.

Bibliography

Agoris, D. P., V. P. Charalambakos, E. Pyrgloti, and S. Grzybowski (2004), A computational approach on the study of Franklin rod height impact on striking distance using a stochastic model, *J. El. Stat.*, *60*(2–4), 175–181, doi: 10.1016/j.elstat.2004.01.020.

Altaratz, O., T. Reisin, and Z. Levin (2005), Simulation of the electrification of winter thunderclouds using the three-dimensional Regional Atmospheric Modeling System (RAMS) model: Single cloud simulations, *J. Geophys. Res.*, *110*(D20205), doi:10.1029/2004JD005616.

Balanis, C. A. (1989), *Advanced Engineering Electromagnetics*, Wiley, New York, NY.

Barthe, C., G. Molinié, and J.-P. Pinty (2005), Description and first results of an explicit electrical scheme in a 3D cloud resolving model, *Atmospheric Research*, *76*(1-4), 95–113, doi:10.1016/j.atmosres.2004.11.021.

Bazelyan, E. M., and Y. P. Raizer (1998), *Spark Discharge*, CRC Press, New York, NY.

Bazelyan, E. M., and Y. P. Raizer (2000), *Lightning Physics and Lightning Protection*, IoP, Philadelphia, PA.

Behnke, S. A., R. J. Thomas, P. R. Krehbiel, and W. Rison (2005), Initial leader velocities during intracloud lightning: Possible evidence for a runaway breakdown effect, *J. Geophys. Res.*, *110*(D12), D10207, doi:10.1029/2004JD005312.

Borodich, F. M. (1997), Some fractal models of fracture, *J. Mech. Phys. Solids*, *45*(2), 239–259, doi:10.1016/S0022-5096(96)00080-4.

Cherepanov, G. P., A. S. Balankin, and V. S. Ivanova (1995), Fractal fracture-mechanics - A review, *Eng. Frac. Mech.*, *51*(6), 997–1,033, doi:10.1016/0013-7944(94)00323-A.

Coleman, L. M., T. C. Marshall, M. Stolzenburg, T. Hamlin, P. R. Krehbiel, W. Rison, and R. J. Thomas (2003), Effects of charge and electrostatic potential on lightning propagation, *J. Geophys. Res.*, *108*(D9), 4298, doi: 10.1029/2002JD002718.

Comtois, D., H. Pépin, F. Vidal, F. A. Rizk, C. Y. Chien, T. W. Johnston, J. C. Kieffer, B. La Fontaine, C. Potvin, P. Couture, H. P. Mercure, A. Bondiou-Clergerie, P. Lalande, and I. Gallimberti (2003), Triggering and guiding of an upward positive leader from a ground rod with an ultrashort laser pulse - II: Modeling, *IEEE Trans. Plasma Sci.*, *31*(3), 387–395, doi:10.1109/TPS.2003.811649.

Dwyer, J. R. (2003), A fundamental limit on electric fields in air, *Geophys. Res. Lett.*, *30*(20), 2055, doi:10.1029/2003GL017781.

Femia, N., L. Niemeyer, and V. Tucci (1993), Fractal characteristics of electrical discharges: experiments and simulation, *J. Phys D: Appl. Phys.*, *26*(4), 619–627, doi:10.1088/0022-3727/26/4/014.

Franklin, B. (1751), *Experiments and Observations on Electricity, made at Philadelphia in America*, E. Cave, London, UK.

Gallimberti, I., G. Bacchiega, A. Bondiou-Clergerie, and P. Lalande (2002), Fundamental processes in long air gap discharges, *C. R. Physique*, *3*(10), 1,335–1,359, doi:10.1016/S1631-0705(02)01414-7.

Greifinger, C., and P. Greifinger (1976), Transient ULF electric and magnetic fields following a lightning discharge, *J. Geophys. Res.*, *81*(13), 2,237–2,247.

Gurevich, A. V., and K. P. Zybin (2001), Runaway breakdown and electric discharges in thunderstorms, *Phys. Uspekhi*, *44*(11), 1,119–1,140.

Gurevich, A. V., G. M. Milikh, and R. A. Roussel-Dupré (1992), Runaway electron mechanism of air breakdown and preconditioning during a thunderstorm, *Phys. Lett. A.*, *165*(5–6), 463–468, doi:10.1016/0375-9601(92)90348-P.

Helsdon, J. H., Jr., G. Wu, and R. D. Farley (1992), An intracloud lightning parameterization scheme for a storm electrification model, *J. Geophys. Res.*, *97*(D5), 5,865–5,884.

Helsdon, J. H., Jr., S. Gattaleeradapan, R. D. Farley, and C. C. Waits (2002), An examination of the convective charging hypothesis: Charge structure, electric fields, and Maxwell currents, *J. Geophys. Res.*, *107*(D22), 4630, doi: 10.1029/2001JD001495.

Helsdon, J. H., Jr., and K. Poeppel (2005), A 3D non grid-point-dependent lightning scheme, *Eos Trans. AGU*, *86*(52), Fall Meet. Suppl., Abstract AE41A-0147.

Hockney, R., and J. Eastwood (1981), *Computer Simulation Using Particles*, McGraw-Hill, New York, NY.

Kasemir, H. W. (1960), A contribution to the electrostatic theory of a lightning discharge, *J. Geophys. Res.*, *65*(7), 1,873–1,878.

Krehbiel, P., W. Rison, R. Thomas, T. Marshall, M. Stolzenburg, W. Winn, and S. Hunyady (2004), Thunderstorm charge studies using a simple cylindrical charge model, electric field measurements, and lightning mapping observations, *Eos Trans. AGU*, *85*(47), Fall Meet. Suppl., Abstract AE23A-0843.

Krider, E. P. (2006), Benjamin Franklin and lightning rods, *Phys. Today*, *59*(1), 42–48.

Kupershtokh, A. L., V. Charalambakos, D. Agoris, and D. I. Karpov (2001), Simulation of breakdown in air using cellular automata with streamer to leader transition, *J. Phys. D: Appl. Phys.*, *34*(6), 936–946, doi:10.1088/0022-3727/34/6/315.

Lagarias, J. C., J. A. Reeds, M. H. Wright, and P. E. Wright (1998), Convergence properties of the Nelder-Mead simplex algorithm in low dimensions, *SIAM Journal on Optimization*, *9*(1), 112–147.

Lalande, P., A. Bondiou-Clergerie, G. Bacchiega, and I. Gallimberti (2002), Observations and modeling of lightning leaders, *C. R. Physique*, *3*(10), 1,375–1,392, doi:10.1016/S1631-0705(02)01413-5.

Lehtinen, N. G., T. F. Bell, and U. S. Inan (1999), Monte Carlo simulation of runaway MeV electron breakdown with application to red sprites and terrestrial gamma ray flashes, *J. Geophys. Res.*, *104*(A11), 24,699–24,712, doi:10.1029/1999JA90033.

Liu, N., and V. P. Pasko (2004), Effects of photoionization on propagation and branching of positive and negative streamers in sprites, *J. Geophys. Res.*, *109*, A04301, doi:10.1029/2003JA010064.

Liu, N., and V. P. Pasko (2006), Effects of photoionization on similarity properties of streamers at various pressures in air, *J. Phys. D: Appl. Phys.*, *39*(2), 327–334, doi:10.1088/0022-3727/39/2/013.

Liu, X. S., and P. R. Krehbiel (1985), The initial streamer of intracloud lightning flashes, *J. Geophys. Res.*, *90*(ND4), 6,211–6,218.

MacGorman, D. R., J. M. Straka, and C. L. Ziegler (2001), A lightning parameterization for numerical cloud models, *J. Appl. Meteor.*, *40*(3), 459–478.

Mandelbrot, B. B. (1983), *The Fractal Geometry of Nature*, updated and augmented ed., W. H. Freeman, New York, NY.

Mansell, E. R., D. R. MacGorman, C. L. Ziegler, and J. M. Straka (2002), Simulated three-dimensional branched lightning in a numerical thunderstorm model, *J. Geophys. Res.*, *107*(D9), 4075, doi:10.1029/2000JD000244.

Mansell, E. R., D. R. MacGorman, C. L. Ziegler, and J. M. Straka (2005), Charge structure and lightning sensitivity in a simulated multicell thunderstorm, *J. Geophys. Res.*, *110*, D12101, doi:10.1029/2004JD005287.

Marshall, T. C., and W. D. Rust (1993), Two types of vertical electrical structures in stratiform precipitation regions of mesoscale convective systems, *Bull. Am. Meteorol. Soc.*, *74*(11), 2,159–2,170.

Marshall, T. C., M. P. McCarthy, and W. D. Rust (1995), Electric field magnitudes and lightning initiation in thunderstorms, *J. Geophys. Res.*, *100*(D4), 7,097–7,104, doi:10.1029/95JD00020.

Marshall, T. C., M. Stolzenburg, and W. D. Rust (1996), Electric field measurements above mesoscale convective systems, *J. Geophys. Res.*, *101*(D3), 6,979–6,996, doi:10.1029/95JD03764.

Marshall, T. C., M. Stolzenburg, W. R. Rust, E. R. Williams, and R. Boldi (2001), Positive charge in the stratiform cloud of a mesoscale convective system, *J. Geophys. Res.*, *106*(D1), 1,157–1,164, doi:10.1029/2000JD900625.

Marshall, T. C., M. Stolzenburg, C. R. Maggio, L. M. Coleman, P. R. Krehbiel, T. Hamlin, R. J. Thomas, and W. Rison (2005), Observed electric fields associated with lightning initiation, *Geophys. Res. Lett.*, *32*, L03813, doi: 10.1029/2004GL021802.

Mazur, V., and L. H. Ruhnke (1998), Model of electric charges in thunderstorms and associated lightning, *J. Geophys. Res.*, *103*(D18), 23,299–23,308.

McCarthy, M. P., and G. K. Parks (1992), On the modulation of X-ray fluxes in thunderstorms, *J. Geophys. Res.*, *97*(D5), 5,857–5,864.

Moss, G. D., V. P. Pasko, N. Liu, and G. Veronis (2006), Monte Carlo model for analysis of thermal runaway electrons in streamer tips in transient luminous events and streamer zones of lightning leaders, *J. Geophys. Res.*, *111*, A02307, doi:10.1029/2005JA011350.

Niemeyer, L., and H. J. Wiesmann (1987), Modeling of leader branching in electronegative gases, pp. 134–139, Gaseous Dielectrics V: Proceedings of the Fifth International Symposium on Gaseous Dielectrics: Knoxville, TN, 3-7 May.

Niemeyer, L., L. Pietrono, and H. J. Wiesmann (1984), Fractal dimension of dielectric breakdown, *Phys. Rev. Lett.*, *52*(12), 1,033–1,036, doi: 10.1103/PhysRevLett.52.1033.

Niemeyer, L., L. Pietrono, and H. J. Wiesmann (1986), Fractal dimension of dielectric breakdown–Response, *Phys. Rev. Lett.*, *57*(5), 650, doi:10.1103/PhysRevLett.57.650.

Niemeyer, L., L. Ullrich, and N. Wiegart (1989), The mechanism of leader breakdown in electronegative gases, *IEEE Trans. on Electr. Insul.*, *24*(2), 309–324, doi:10.1109/14.90289.

Ogawa, T., and M. Brook (1964), Mechanism of intracloud lightning discharge, *J. Geophys. Res.*, *69*(24), 5,141.

Pasko, V. P. (2006), Theoretical modeling of sprites and jets, in *Sprites, Elves and Intense Lightning Discharges*, *NATO Science Series II: Mathematics, Physics and Chemistry*, vol. 225, edited by M. Füllekrug, E. A. Mareev and M. J. Rycroft, pp. 253–311, Springer, Heidleberg, Germany.

Pasko, V. P., and J. J. George (2002), Three-dimensional modeling of blue jets and blue starters, *J. Geophys. Res.*, *107*(A12), 1458, doi:10.1029/2002JA009473.

Pasko, V. P., U. S. Inan, T. F. Bell, and Y. N. Taranenko (1997), Sprites produced by quasi-electrostatic heating and ionization in the lower ionosphere, *J. Geophys. Res.*, *102*(A3), 4,529–4,561, doi:10.1029/96JA03528.

Pasko, V. P., U. S. Inan, and T. F. Bell (2000), Fractal structure of sprites, *Geophys. Res. Lett.*, *27*(4), 497–500, doi:10.1029/1999GL010749.

Pasko, V. P., U. S. Inan, and T. F. Bell (2001), Mesosphere-troposphere coupling due to sprites, *Geophys. Res. Lett.*, *28*(19), 3,821–3,824, doi:10.1029/2001GL013222.

Petrov, N. I., and G. N. Petrova (1992), Simulation of the branching and bending of breakdown channels in dielectrics, *Tech. Phys. Lett.*, *18*(2), 65–67.

Petrov, N. I., and G. N. Petrova (1993), Physical mechanisms for intracloud lightning discharges, *Techn. Phys.*, *38*(4), 287–290.

Petrov, N. I., G. N. Petrova, and F. D'Alessandro (2003), Quantification of the probability of lightning strikes to structures using a fractal approach, *IEEE Trans. on Dielectr. and Electr. Insul.*, *10*(4), 641–654, doi:10.1109/TDEI.2003.1219649.

Poeppel, K. (2005), A 3D Lightning parameterization with branching and charge induction, Master's thesis, South Dakota School of Mines and Technology, Rapid City, SD.

Popov, N. A. (2002), Spatial structure of the branching streamer channel in a corona discharge, *Plasma Phys. Rep.*, *28*(17), 615–622, doi:10.1134/1.1494061.

Potter, D. (1973), *Computational Physics*, Wiley, New York, NY.

Press, W. H., B. P. Flannery, S. A. Teukolsky, and W. T. Vetterling (1992), *Numerical Recipes in C: The Art of Scientific Computing*, second ed., Cambridge Univ. Press, New York, NY.

Proctor, D. E. (1981), VHF radio pictures of cloud flashes, *J. Geophys. Res.*, *86*(NC5), 4,041–4,071.

Proctor, D. E. (1983), Lightning and precipitation in a small multicellular thunderstorm, *J. Geophys. Res.*, *88*(NC9), 5,421–5,440.

Proctor, D. E. (1997), Lightning flashes with high origins, *J. Geophys. Res.*, *102*(D2), 1,693–1,706, doi:10.1029/96JD02635.

Raizer, Y. P. (1991), *Gas Discharge Physics*, Springer-Verlag, New York, NY.

Rakov, V. A., and M. A. Uman (2003), *Lightning Physics and Effects*, Cambridge Univ. Press, New York, NY.

Riousset, J. A., V. P. Pasko, P. R. Krehbiel, R. J. Thomas, and W. Rison (2006a), Three-dimensional fractal modeling of intracloud lightning discharge in a New Mexico thunderstorm and comparison with lightning mapping observations, *J. Geophys. Res.*, doi:10.1088/xxx-xxxx, In review.

Riousset, J. A., V. P. Pasko, P. R. Krehbiel, R. J. Thomas, and W. Rison (2006b), Electrical structure of thunderclouds leading to formation of blue jets and gigantic jets, *2006 CEDAR Workshop, Poster Session Booklet #2*, p. 6, Abstract COUP-05, Santa Fe, New Mexico, June 22, 2006.

Rison, W., R. J. Thomas, P. R. Krehbiel, T. Hamlin, and J. Harlin (1999), A GPS-based three-dimensional lightning mapping system: Initial observations in central New Mexico, *Geophys. Res. Lett.*, *26*(23), 3,573–3,576, doi:10.1029/1999GL010856.

Roussel-Dupré, R. A., A. V. Gurevich, T. Tunnel, and G. M. Milikh (1994), Kinetic theory of runaway breakdown, *Phys. Rev. E*, *49*(3), 2,257–2,271, doi:10.1103/PhysRevE.49.2257.

Satpathy, S. (1986), Fractal dimension of dielectric breakdown–Comment, *Phys. Rev. Lett.*, *57*(5), 649, doi:10.1103/PhysRevLett.57.649.

Shao, X. M., and P. R. Krehbiel (1996), The spatial and temporal development of intracloud lightning, *J. Geophys. Res.*, *101*(D21), 26,641–26,668.

Shepherd, T. R., W. D. Rust, and T. C. Marshall (1996), Electric fields and charges near 0 degrees C in stratiform clouds, *Mon. Wea. Rev.*, *124*(5), 919–938.

Stolzenburg, M., W. D. Rust, and T. C. Marshall (1998a), Electrical structure in thunderstorm convective regions - 1. Mesoscale convective systems, *J. Geophys. Res.*, *103*(D12), 14,059–14,078, doi:10.1029/97JD03546.

Stolzenburg, M., W. D. Rust, and T. C. Marshall (1998b), Electrical structure in thunderstorm convective regions - 2. Isolated storms, *J. Geophys. Res.*, *103*(D12), 14,079–14,096, doi:10.1029/97JD03547.

Stolzenburg, M., W. D. Rust, and T. C. Marshall (1998c), Electrical structure in thunderstorm convective regions - 3. Synthesis, *J. Geophys. Res.*, *103*(D12), 14,097–14,108, doi:10.1029/97JD03545.

Uman, M. A. (1984), *Lightning*, reprint ed., Dover, Mineola, NY.

Uman, M. A. (2001), *The Lightning Discharge*, unabridged ed., Dover, Mineola, NY.

Werner, D. H. (1998), A method of moments approach for the efficient and accurate modeling of moderately thick cylindrical wire antennas, *IEEE Trans. Antennas Propag.*, *46*(3), 373–382, doi:10.1109/8.662656.

Williams, E. R. (1989), The tripolar structure of thunderstorms, *J. Geophys. Res.*, *94*(D11), 13,151–13,167.

Williams, E. R., C. M. Cooke, and K. A. Wright (1985), Electrical discharge propagation in and around space charge clouds, *J. Geophys. Res.*, *90*(D4), 6,059–6,070.

Winn, W. P., and I. Byerley, L. G. (1975), Electric field growth in thunderclouds, *Quart. J. R. Met. Soc.*, *101*, 979–994.

Winn, W. P., G. W. Schwede, and C. B. Moore (1974), Measurements of electric fields in thunderclouds, *J. Geophys. Res.*, *79*(12), 1,761–1,767.

Zahn, M. (1987), *Electromagnetic Field Theory: A Problem Solving Approach*, reprint ed., R.F. Krieger, Malabar, FL.

Ziegler, C. L., and D. R. MacGorman (1994), Observed lightning morphology relative to modeled space charge and electric field distributions in a tornadic storm, *J. Appl. Meteor.*, *51*(6), 833–851.